EPRI | ELECTRIC POWER RESEARCH INSTITUTE

Materials Reliability Program: Advanced FEA Evaluation of Growth of Postulated Circumferential PWSCC Flaws in Pressurizer Nozzle Dissimilar Metal Welds (MRP-216, Rev. 1)

Evaluations Specific to Nine Subject Plants

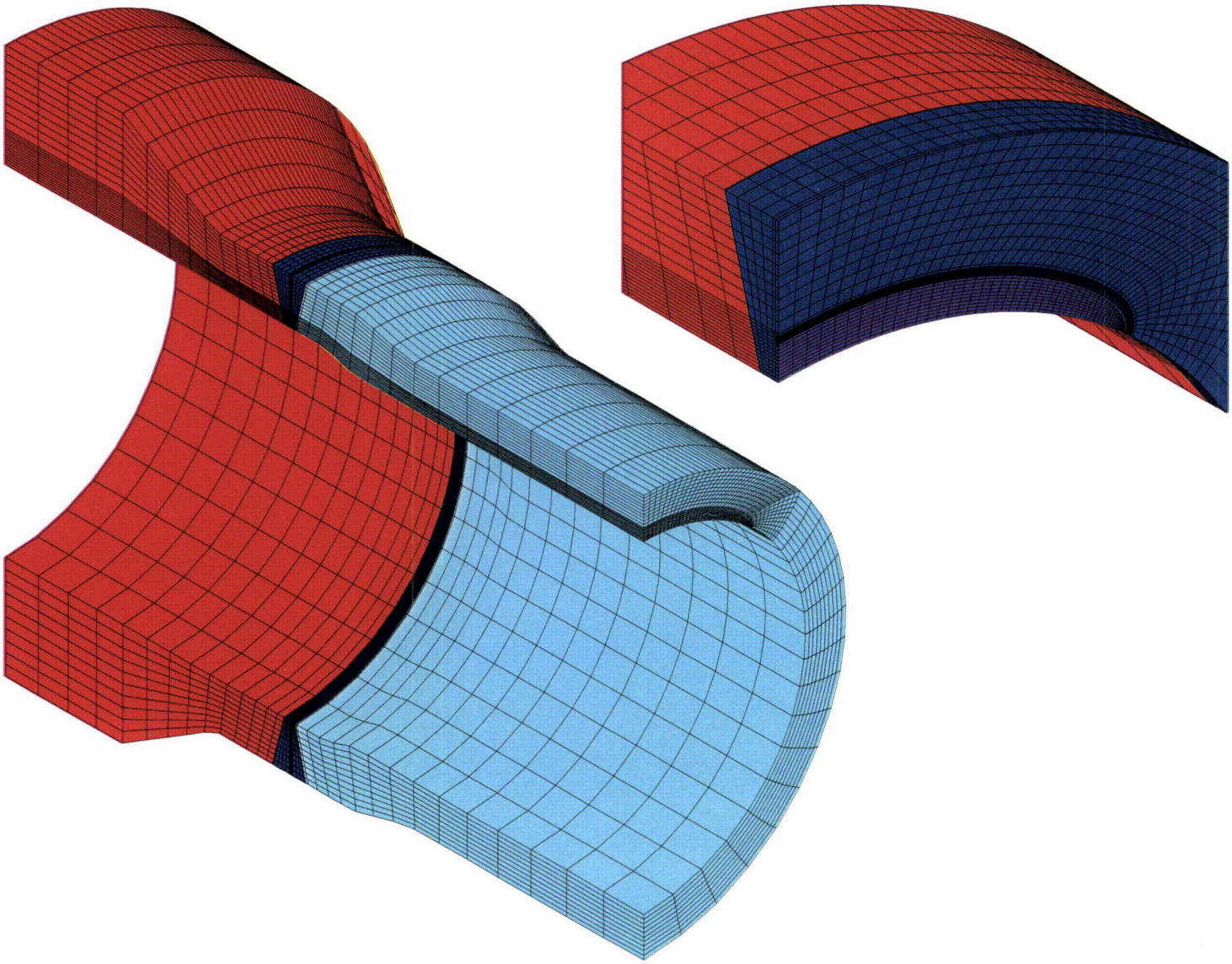

Materials Reliability Program: Advanced FEA Evaluation of Growth of Postulated Circumferential PWSCC Flaws in Pressurizer Nozzle Dissimilar Metal Welds (MRP-216, Rev. 1)

Evaluations Specific to Nine Subject Plants

1015400

Final Report, August 2007

EPRI Project Manager
C. Harrington

ELECTRIC POWER RESEARCH INSTITUTE
3420 Hillview Avenue, Palo Alto, California 94304-1338 • PO Box 10412, Palo Alto, California 94303-0813 • USA
800.313.3774 • 650.855.2121 • askepri@epri.com • www.epri.com

DISCLAIMER OF WARRANTIES AND LIMITATION OF LIABILITIES

THIS DOCUMENT WAS PREPARED BY THE ORGANIZATION(S) NAMED BELOW AS AN ACCOUNT OF WORK SPONSORED OR COSPONSORED BY THE ELECTRIC POWER RESEARCH INSTITUTE, INC. (EPRI). NEITHER EPRI, ANY MEMBER OF EPRI, ANY COSPONSOR, THE ORGANIZATION(S) BELOW, NOR ANY PERSON ACTING ON BEHALF OF ANY OF THEM:

(A) MAKES ANY WARRANTY OR REPRESENTATION WHATSOEVER, EXPRESS OR IMPLIED, (I) WITH RESPECT TO THE USE OF ANY INFORMATION, APPARATUS, METHOD, PROCESS, OR SIMILAR ITEM DISCLOSED IN THIS DOCUMENT, INCLUDING MERCHANTABILITY AND FITNESS FOR A PARTICULAR PURPOSE, OR (II) THAT SUCH USE DOES NOT INFRINGE ON OR INTERFERE WITH PRIVATELY OWNED RIGHTS, INCLUDING ANY PARTY'S INTELLECTUAL PROPERTY, OR (III) THAT THIS DOCUMENT IS SUITABLE TO ANY PARTICULAR USER'S CIRCUMSTANCE; OR

(B) ASSUMES RESPONSIBILITY FOR ANY DAMAGES OR OTHER LIABILITY WHATSOEVER (INCLUDING ANY CONSEQUENTIAL DAMAGES, EVEN IF EPRI OR ANY EPRI REPRESENTATIVE HAS BEEN ADVISED OF THE POSSIBILITY OF SUCH DAMAGES) RESULTING FROM YOUR SELECTION OR USE OF THIS DOCUMENT OR ANY INFORMATION, APPARATUS, METHOD, PROCESS, OR SIMILAR ITEM DISCLOSED IN THIS DOCUMENT.

ORGANIZATION(S) THAT PREPARED THIS DOCUMENT

Dominion Engineering, Inc. (Except Appendices)

Structural Integrity Associates, Inc. (Appendices B, D, and E)

Quest Reliability, LLC (Appendix C)

Westinghouse Electric Co. (Appendix A)

NOTE

For further information about EPRI, call the EPRI Customer Assistance Center at 800.313.3774 or e-mail askepri@epri.com.

CITATIONS

This report (except appendices) was prepared by

Dominion Engineering, Inc.
11730 Plaza America Drive
Suite 310
Reston, VA 20190

Principal Investigators
G. A. White
J. E. Broussard

Contributors
J. E. Collin
M. T. Klug
D. J. Gross
V. D. Moroney

The authors of each of the appendices are identified on the first page of each respective appendix.

MRP-216 was previously issued as a Technical Update (Product ID 1015383) in order to support short-term documentation needs of licensees. There are no technical or editorial changes within the body of the report between the original Technical Update version and this Final Report (Revision 1), although formatting changes may have resulted from the publishing process. Minor editorial changes were incorporated into the Report Summary (pages v and vi).

This report describes research sponsored by the Electric Power Research Institute (EPRI). The report is a corporate document that should be cited in the literature in the following manner:

Materials Reliability Program: Advanced FEA Evaluation of Growth of Postulated Circumferential PWSCC Flaws in Pressurizer Nozzle Dissimilar Metal Welds (MRP-216, Rev. 1): Evaluations Specific to Nine Subject Plants. EPRI, Palo Alto, CA: 2007. 1015400.

REPORT SUMMARY

Indications of circumferential flaws in the pressurizer nozzles at Wolf Creek raised questions about the need to accelerate refueling outages or take mid-cycle outages at other plants. This study demonstrates the viability of leak detection as a means to preclude the potential for rupture for the pressurizer nozzle dissimilar metal (DM) welds in a group of nine PWRs originally scheduled to perform performance demonstration initiative (PDI) inspection or mitigation during the spring 2008 outage season. Modeling showed that the classical assumption of a semi-elliptical crack shape results in a large overestimation of the crack area and thus an underestimation of crack stability at the time when the crack penetrates to the outside surface.

Background

In October 2006, several indications of circumferential flaws were reported in the pressurizer nozzles at Wolf Creek. The indications were located in the nickel-based Alloy 82/182 DM weld material, which is known to be susceptible to primary water stress corrosion cracking (PWSCC). During its fall 2006 outage, Wolf Creek addressed the concern for growth of these circumferential indications by applying previously scheduled weld overlays. In late 2006, the Materials Reliability Program (MRP) performed a series of short-term evaluations regarding the implications of the Wolf Creek indications for other PWR plants. This study extends the crack growth calculations of these short-term evaluations to consider flaw shape development based on the crack-tip stress intensity factor calculated at each point along the crack front.

Objective

- To evaluate the viability of detection of leakage from a through-wall flaw in an operating plant to preclude the potential for rupture of pressurizer nozzle DM welds in the group of nine PWRs originally scheduled for PDI inspection or mitigation during the spring 2008 outage season, given the potential concern about growing circumferential stress corrosion cracks

Approach

In order to facilitate modeling of the crack shape development, Quest Reliability, LLC extended its FEACrack software to model the growth of circumferential flaws having a custom profile. In Phase I of this study, the team applied this new software tool to the same basic weld geometry, piping load inputs, and welding residual stress distribution assumed in the late 2006 MRP calculation. In Phase II, the team investigated an extensive crack growth sensitivity matrix to cover the geometry, load, and fabrication factors for each of the 51 subject welds, as well as the uncertainty in key modeling parameters including the effect of multiple flaw initiation sites in a single weld. Other key Phase II activities included detailed welding residual stress simulations covering the subject welds, development of a conservative crack stability calculation

methodology, development of a leak rate calculation procedure using existing software tools (EPRI PICEP and NRC SQUIRT), and verification and validation studies.

Results

Based on the detailed input of an EPRI-led expert panel, researchers developed a set of criteria to evaluate the results of the crack growth, crack stability, and leak rate calculations for each sensitivity case investigated. The evaluation criteria provide safety margins based on explicit consideration of leak rate detection sensitivity, plant response time, and uncertainty in the crack stability calculations. An extensive sensitivity matrix of 119 cases was developed to robustly address the weld-specific geometry and load input parameters for the set of 51 subject welds, plus the key modeling uncertainties. All 109 cases in the main sensitivity matrix showed either stable crack arrest (60 cases) or crack leakage and crack stability results that satisfied the evaluation criteria (49 cases). In most cases, the results showed large evaluation margins in leakage time and in crack stability. Ten supplemental cases added to further investigate the potential effect of multiple flaws in the subject surge nozzles also satisfied the evaluation criteria with the exception of two cases that involved initial flaw assumptions that are not credible.

An additional key finding concerns the significant number of crack growth sensitivity cases that showed stable crack arrest prior to through-wall penetration. This type of behavior is consistent with the relatively narrow band of relative depths reported for the four largest Wolf Creek indications. Also, detailed evaluations tend to support the relaxation of piping thermal constraint stresses prior to rupture, but such relaxation was conservatively not credited in the base assumptions of the critical crack size methodology developed for this study. Instead, 100% of the normal operating thermal piping loads (excluding surge line thermal stratification effects) was included in the critical crack size calculations.

EPRI Perspective

This study extends the state of the art regarding modeling of PWSCC crack growth. EPRI report 1006696 (MRP-115), which developed a deterministic crack growth rate equation as a function of stress intensity factor on the basis of worldwide laboratory testing of controlled fracture mechanics specimens, provided key input to the crack growth calculations of this study. The crack growth methodology developed in support of this study may be applied in similar future applications for PWR components other than the pressurizer. EPRI report 1010087 (MRP-139) defines inspection and evaluation requirements for DM (Alloy 82/182) welds in U.S. PWRs. EPRI report 1011808 (MRP-140) evaluates previous regulatory leak-before-break (LBB) submittals to the NRC given the potential for the presence of PWSCC at Alloy 82/182 locations.

Keywords

Alloy 600
Alloy 82/182
Crack growth modeling
Dissimilar metal piping butt/girth welds
Leak before break (LBB)
Pressurizer nozzles
Primary water stress corrosion cracking (PWSCC)

ABSTRACT

In October 2006, several indications of circumferential flaws were reported in the Wolf Creek pressurizer nozzles. The indications were reported to be located in the nickel-based Alloy 82/182 dissimilar metal (DM) weld material, which is known to be susceptible to primary water stress corrosion cracking (PWSCC). In late 2006, the Materials Reliability Program (MRP) performed a series of short-term evaluations of the implications of the Wolf Creek indications for other PWR plants. This study extends the crack growth calculations of the short-term evaluations to consider flaw shape development based on the crack-tip stress intensity factor calculated at each point along the crack front.

The objective of this study is to evaluate the viability of operating plant leak detection, from a through-wall flaw perspective, to preclude the potential for rupture for the pressurizer nozzle DM welds in the group of nine PWRs originally scheduled to perform PDI inspection or mitigation during the spring 2008 outage season, given the potential concern for growing circumferential stress corrosion cracks. Commitments have been made for these nine PWRs to accelerate refueling outages or take mid-cycle outages. Should this study demonstrate flaw stability via sufficient time from initial detectable leakage until pipe rupture, as demonstrated to the NRC, these plants could then resume plans to perform PDI inspection or mitigation during the spring 2008 outage season. In Phase I of this study, newly enhanced FEACrack software tools were applied to the same basic weld geometry, piping load inputs, and welding residual stress distribution assumed in the late 2006 MRP calculation. In Phase II, an extensive crack growth sensitivity matrix of 119 cases was investigated to robustly address the geometry, load, and fabrication factors for each of the 51 subject welds, as well as the uncertainty in key modeling parameters including the effect of multiple flaw initiation sites in a single weld. Other key Phase II activities included detailed welding residual stress simulations, development of a conservative crack stability calculation methodology, development of a leak rate calculation procedure using existing software tools, and verification and validation studies.

This study demonstrated that the classical assumption of a semi-elliptical crack shape results in a large overestimation of the crack area and thus underestimation of the crack stability at the point in time at which the crack penetrates to the outside surface. All 109 cases in the main sensitivity matrix showed either stable crack arrest (60 cases) or crack leakage and crack stability results satisfying the evaluation criteria (49 cases). In most cases, the results showed large evaluation margins in leakage time and in crack stability. Ten supplemental cases were added to further investigate the potential effect of multiple flaws in the subject surge nozzles. With the exception of two cases that involved initial flaw assumptions that are not credible (as discussed in the report), the supplemental sensitivity cases also satisfied the evaluation criteria. In summary, this study demonstrated the viability of leak detection to preclude the potential for rupture for the subject pressurizer nozzle DM welds.

ACKNOWLEDGMENTS

This study was completed with the detailed support and input of the expert review panel assembled by EPRI and of utility reviewers:

EPRI Project Management and Support

C. Harrington (EPRI), C. King (EPRI), and T. Gilman (Structural Integrity Associates)

EPRI Expert Review Panel

T. Anderson (Quest Reliability, LLC), W. Bamford (Westinghouse), D. Harris (Structural Integrity Associates), D. Killian (AREVA), P. Riccardella (Structural Integrity Associates), and K. Yoon (AREVA)

Utility Reviewers

W. Borrero (APS), G. DeBoo (Exelon), M. Dove (Southern Co.), L. Goyette (PG&E), T. McAlister (SCANA), M. Melton (NEI), V. Penacerrada (Entergy), W. Sims (Entergy), D. Sutton (Southern Co.), and C. Tran (TXU Energy)

In direct support of this study, Quest Reliability, LLC extended its FEACrack software to model the growth of circumferential flaws having a custom profile. G. Thorwald and D. Revelle led the software development effort at Quest Reliability, LLC.

ACRONYMS

The following acronyms are used in the main body of this report:

ANSC	(Structural Integrity Associates) Arbitrary Net Section Collapse software
ASME	American Society of Mechanical Engineers
CE	Combustion Engineering
CGR	crack growth rate
CMTR	certified material test report
COA	crack opening area
COD	crack opening displacement
DEI	Dominion Engineering, Inc.
DM	dissimilar metal
DMW	dissimilar metal weld
DPZP	dimensionless plastic zone parameter
EMC^2	Engineering Mechanics Corporation of Columbus
EPFM	elastic-plastic fracture mechanics
EPRI	Electric Power Research Institute
FEA	finite-element analysis
ID	inside diameter
IGSCC	intergranular stress corrosion cracking
LBB	leak before break
MRP	Materials Reliability Program
ND	neutron diffraction
NDE	non-destructive examination
NRC	Nuclear Regulatory Commission
NSC	net section collapse
NSSS	nuclear steam supply system
OD	outside diameter
PDI	performance demonstration initiative
PICEP	(EPRI) Pipe Crack Evaluation Program
PWR	pressurized water reactor
PWSCC	primary water stress corrosion cracking
RCS	reactor coolant system
SCC	stress corrosion cracking
SIF	stress intensity factor
SQUIRT	(NRC) Seepage Quantification of Upsets in Reactor Tubes
UT	ultrasonic testing
WRS	welding residual stress

CONTENTS

LIST OF TABLES

LIST OF FIGURES

1
INTRODUCTION

This introductory section provides a brief background discussion, defines the purpose and scope of this study, and outlines the approach used. This section also outlines how this report is organized.

1.1 Background

1.1.1 Fall 2006 Wolf Creek Inspection Results and MRP White Paper

In October 2006, several indications of circumferential flaws were reported in the Wolf Creek pressurizer nozzles. The indications were reported to be located in the nickel-based Alloy 82/182 dissimilar metal weld material, which is known to be susceptible to primary water stress corrosion cracking (PWSCC). During its fall 2006 outage, Wolf Creek addressed the concern for growth of these circumferential indications through application of weld overlays that were previously scheduled. Because of the concern that circumferential flaws could grow via the PWSCC mechanism to critical size, the Materials Reliability Program (MRP) performed a series of short-term evaluations of the implications of the Wolf Creek indications for other PWR plants. The results of those short-term evaluations were released in January 2007 in the form of an MRP "white paper"[1].

1.1.2 December 2006 Crack Growth Evaluations

On November 30, 2006, the NRC staff presented the results of crack growth calculations investigating past and hypothetical future growth of the circumferential indications that were reported in three of the Wolf Creek pressurizer nozzle-to-safe-end dissimilar metal welds, assuming mitigation was not applied [2,3]. In December 2006 under sponsorship of the MRP, Dominion Engineering, Inc. (DEI) performed crack growth calculations [4] using a finite-element analysis (FEA) approach to calculate stress intensity factors (SIFs, also denoted as K) and crack growth for comparison with the crack growth time results presented by the NRC. The circumferential indication reported for the Wolf Creek relief nozzle was the largest indication reported relative to the weld cross sectional area. Therefore, the relief nozzle was selected as the geometry to investigate for this previous MRP calculation. Basic weld geometry and piping load inputs were maintained identical in the NRC and MRP calculations. Key findings of the December 2006 MRP calculation were as follows:

- The MRP results showed significantly longer time to through-wall penetration (4.4 years for the MRP calculation) than did the NRC calculation. The main source for this difference was identified as the use of conservative extrapolations of published SIF solutions in the NRC calculation versus the use of FEA calculations specific to the geometry of interest in

the MRP calculation. Using the FEA approach to calculate crack tip SIFs allowed evaluation of the actual low radius-to-thickness ratio (Ri/t = 2.00) for the Wolf Creek relief nozzle dissimilar metal weld instead of extrapolating from available stress intensity factor correlations for higher Ri/t ratios.

- Although the MRP calculation showed longer time to leakage, both calculations showed no time between through-wall penetration and rupture for the case of axisymmetric welding residual stress investigated in the MRP calculation.

- The FEA approach was also used to consider the potential effect of redistribution and relaxation of welding residual stress with crack growth, which is not possible through the use of standard stress intensity factor correlations based on the superposition principle. This effect did not appear to be a significant factor for the flaws considered and assumptions made in simulating welding residual stress.

- The FEA analysis results were used to calculate crack tip SIFs along the entire crack front for all flaw cases considered. These results showed that many of the larger flaw geometries had considerably lower crack tip SIFs at locations between flaw surface and the flaw center, including, in many cases, a region of crack tip closure. Therefore, assuming that the flaw maintains a semi-elliptical shape may not accurately reflect the actual crack growth under the assumed loading conditions.

In the current study presented in this report, an extensive matrix of crack growth cases was evaluated using newly developed software that models the growth of arbitrary shape flaws based on the SIF at each point along the crack front, reflecting the change in crack shape due to the influence of the complex crack loading.

1.2 Objective

The objective of this study is to evaluate the viability of operating plant leak detection, from a through-wall flaw perspective, to preclude the potential for rupture for the pressurizer nozzle dissimilar metal (DM) welds in the group of nine PWRs originally scheduled to perform PDI inspection or mitigation during the spring 2008 outage season, given the potential concern for growing circumferential stress corrosion cracks. Commitments have been made for these nine PWRs to accelerate refueling outages or take mid-cycle outages. Should this study demonstrate flaw stability via sufficient time from initial detectable leakage until pipe rupture, as demonstrated to the NRC, these plants could then resume plans to perform PDI inspection or mitigation during the spring 2008 outage season.

1.3 Scope

The scope of this study is limited to the pressurizer nozzle DM welds in the group of nine PWRs scheduled to performed PDI inspection or mitigation during the spring 2008 outage season. All other U.S. PWR plants either do not have any Alloy 82/182 pressurizer nozzle DM welds or are scheduled to complete PDI inspection or mitigation before December 31, 2007, the original implementation date established by the MRP for the pressurizer DM weld locations.

The nine subject PWR plants are Braidwood 2, Comanche Peak 2, Diablo Canyon 2, Palo Verde 2, Seabrook, South Texas Project 1, V.C. Summer, Vogtle 1, and Waterford 3. Fifty-one of the total number of 53 pressurizer nozzles in these plants are within the scope of this study. The spray nozzle in one plant was PDI inspected in 2005, and as such is not included in the scope. In addition, the surge nozzle in one plant has already had weld overlay application, and as such is not included in the scope. Seven of the nine subject plants are Westinghouse design plants, and the other two are CE design plants. Figures 1-1 through 1-3 illustrate the nozzle locations and example configurations for pressurizer nozzles in Westinghouse and CE design plants. As discussed in Section 2, detailed weld-specific geometry, load, and fabrication parameters were collected for all 51 subject welds.

1.4 Approach

In order to facilitate modeling of the crack shape development and in direct support of this study, Quest Reliability, LLC extended its FEACrack software to model the growth of circumferential flaws having a custom profile. In Phase I of this study, the new software tools were applied to the same basic weld geometry, piping load inputs, and welding residual stress distribution assumed in the previous MRP calculation [4]. In Phase II, an extensive crack growth sensitivity matrix was investigated to cover the geometry, load, and fabrication factors for each of the 51 subject welds, as well as the uncertainty in key modeling parameters such as those associated with welding residual stress, initial crack shape and depth, the K-dependence of the crack growth rate equation, and the effect of multiple flaw initiation sites in a single weld. Other key Phase II activities included detailed welding residual stress simulations covering the subject welds, development of a conservative crack stability calculation methodology, development of a leak rate calculation procedure using existing software tools (EPRI PICEP and NRC SQUIRT), and verification and validation studies.

1.5 Expert Panel

In support of this study, EPRI assembled a panel of experts experienced in the application of fracture mechanics tools to the evaluation of stress corrosion cracking. The panel included representation of individuals not recently involved in the evaluation of PWSCC in PWR components. The panel provided detailed input into all phases of the project as the work progressed.

1.6 Report Structure

The organization of this report is described below.

1. INTRODUCTION (SECTION 1)

   This introductory section provides a brief background discussion, defines the purpose and scope of this study, and outlines the approach used.

2. PLANT INPUTS (SECTION 2)

   Section 2 summarizes the extensive weld-specific dimensional, piping load, fabrication, and weld repair history inputs that were collected for the group of 51 subject pressurizer

nozzles. Detailed geometry and piping load inputs were collected for each subject weld to ensure that all welds are appropriately addressed by the crack growth sensitivity matrix (Section 7) developed as part of this study. Weld-specific fabrication and weld repair data were also collected as a key input to the welding residual stress simulations addressing the subject population (Section 3). Appendix A contains more detailed information on the design and fabrication of the subject nozzles and welds.

3. WELDING RESIDUAL STRESS (SECTION 3)

   Section 3 discusses the matrix of welding residual stress (WRS) simulations that were performed on the basis of the detailed design, fabrication, and weld repair information collected. Axisymmetric and non-axisymmetric weld repair WRS profiles were developed for input to the crack growth simulations under various assumptions in recognition of the uncertainty in calculation of WRS values. Section 3 also includes the results of validation work comparing a WRS simulation by the authors to stress measurements and the simulations of other organizations for a piping butt weld mockup.

4. CRACK GROWTH MODELING (SECTION 4)

   Section 4 describes the new crack growth simulation methodology, including development of the new extensions to the FEACrack software. This section also describes application of the new software in the Phase I calculations, which are based on the same Wolf Creek relief nozzle inputs previously evaluated on the basis of an assumed semi-elliptical crack shape. Section 4 also includes the results of verification and validation work, including calculation convergence checks.

5. CRITICAL CRACK SIZE CALCULATIONS (SECTION 5)

   Section 5 describes the development of a conservative critical crack size methodology specific to the subject nozzle-to-safe-end geometry and materials. This methodology is based on the net section collapse (NSC) equations for an arbitrary circumferential crack profile in a thin-walled pipe. As discussed in Section 5 and for the purposes of this project, normal thermal piping loads were included in the crack stability calculations, and a Z-factor approach reducing the NSC failure load was implemented in consideration of the possibility of an EPFM failure mechanism. Finally, in support of the methodology, available experimental failure data for complex cracks in materials similar to Alloy 82/182 were evaluated.

6. LEAK RATE MODELING (SECTION 6)

   Section 6 describes the leak rate calculation procedure applied to the through-wall portion of the crack growth simulations using EPRI's PICEP software. The crack opening area at the weld OD calculated in the crack growth finite-element simulations was applied directly in the PICEP leak rate calculations. NRC's SQUIRT software was also applied in a scoping study for the purpose of comparison.

7. SENSITIVITY CASE MATRIX (SECTION 7)

   Section 7 discusses the development and application of an extensive crack growth sensitivity matrix covering the geometry, load, and fabrication factors for each of the 51 subject welds, as well as the uncertainty in key modeling parameters such as those associated with welding residual stress, initial crack shape and depth, the K-dependence of the crack growth rate equation, and the effect of multiple flaw initiation sites in a single

weld. Section 7 also presents a set of evaluation criteria that was developed to guide interpretation of the matrix results. The evaluation criteria provide safety margins based on explicit consideration of leak rate detection sensitivity, plant response time, and uncertainty in the crack stability calculations.

8. SUMMARY AND CONCLUSIONS (SECTION 8)

   Section 8 summarizes this study, including the main conclusions. It is concluded that all 51 subject welds are adequately covered by crack growth sensitivity cases that satisfy the evaluation criteria presented in Section 7.2.

9. REFERENCES (SECTION 9)

   Section 9 lists the references cited in the main body of this report.

10. APPENDIX A: DISSIMILAR METAL BUTT WELD FABRICATION PROCESSES

    Appendix A describes the detailed nozzle fabrication practices for the subject set of pressurizer nozzle welds. In addition, Appendix A includes design sketches with key dimensions for the subject welds.

11. APPENDIX B: EVALUATION OF THE EFFECTS OF SECONDARY STRESSES ON SURGE LINE CRITICAL FLAW SIZE CALCULATIONS

    In support of the critical flaw size analyses described in Section 5, Appendix B describes analyses of the effects of secondary (displacement controlled) loads on critical flaw size. The evaluation included a review of test data from the NRC-sponsored Degraded Piping Program. Detailed test data from selected full scale pipe tests of relevant materials, pipe sizes, and flaw types were reviewed to determine the amount of crack plane rotation that was tolerated in the tests prior to failure. In addition, piping models were developed for the surge lines of two representative plants to evaluate the maximum capacity of the secondary loads to produce rotation at a cracked surge nozzle, relative to the rotational tolerance of a nozzle weld containing a large complex crack. The results of this study support the conclusion that the surge nozzle piping thermal loads are completely relieved prior to nozzle rupture.

12. APPENDIX C: SECONDARY STRESS STUDY—PIPE BENDING WITH A THROUGH-THICKNESS CRACK

    Appendix C describes elastic and elastic-plastic finite element analyses of a pipe with an idealized through-thickness crack that were used to determine the effect on bending moment and crack driving force due to an imposed end rotation. Because of the finite amount of strain imposed by the rotation, the results show that the moment knock-down factor and crack driving force relative to the load controlled case decrease significantly as the crack length increases. These results further support the conclusions of Appendix B, and demonstrate the general tendency for relief of secondary piping loads given sufficient crack plane rotation.

13. APPENDIX D: SCATTER IN LEAK RATE PREDICTIONS

    Appendix D describes a statistical study of experimental leak rate data for through-wall cracks having an IGSCC morphology. This study shows that a multiplicative factor of 1.5 to 2.0 on the leak rate calculated using the NRC SQUIRT code describes the uncertainty in leak rate due to scatter in the test data for the IGSCC samples tested. A leak rate margin factor of 4.0 is applied in Section 7 in recognition of other sources of uncertainty in the

leak rate calculation not addressed by this statistical evaluation such as the variability in the PWSCC crack morphology parameters (e.g., crack surface roughness and tortuosity) versus the PWSCC type assumptions in Section 6.

14. APPENDIX E: EVALUATION OF PRESSURIZER ALLOY 82/182 NOZZLE FAILURE PROBABILITY

Appendix E describes the methodology and results of a complementary probabilistic study. This study considered current inspection data to assess the effect of various inspection options on the probability of a nozzle failure in the time interval until all nozzles are inspected or mitigated. Appendix E concludes that there is no significant benefit, in terms of reduced nozzle failure probability, to accelerating the originally scheduled spring 2008 inspections.

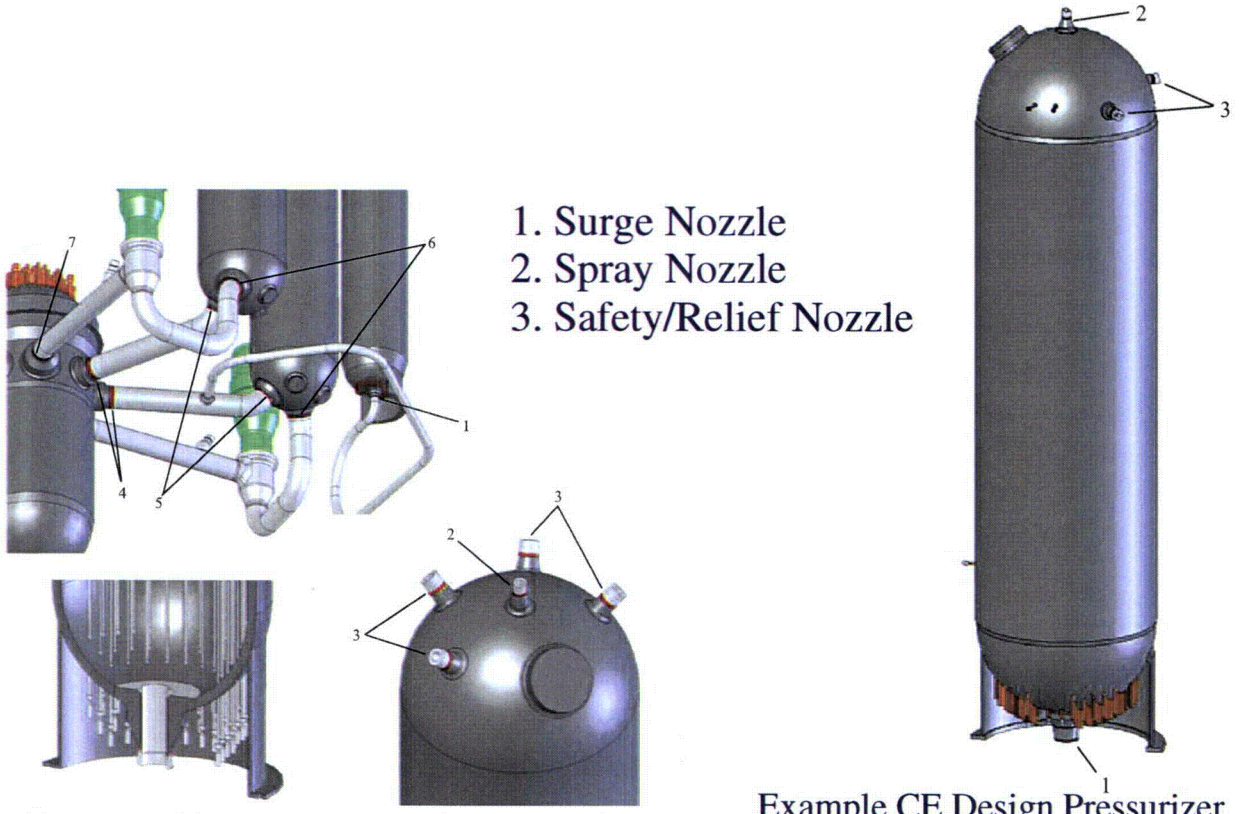

Figure 1-1
Pressurizer Nozzle Locations for Westinghouse and CE Design Plants

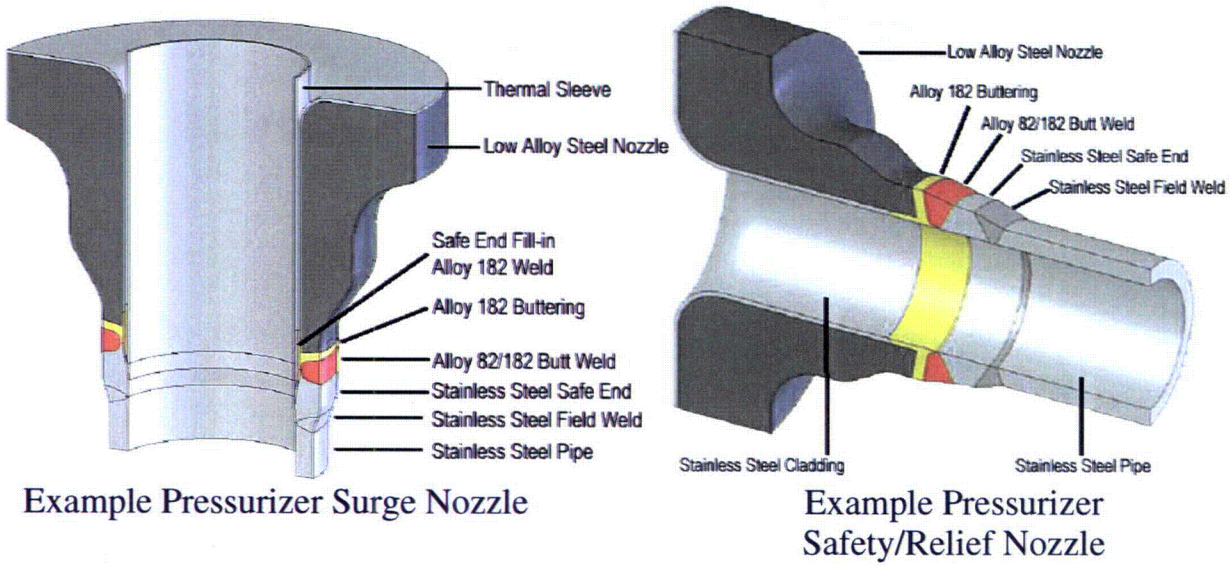

Figure 1-2
Example Westinghouse Design Pressurizer Nozzles

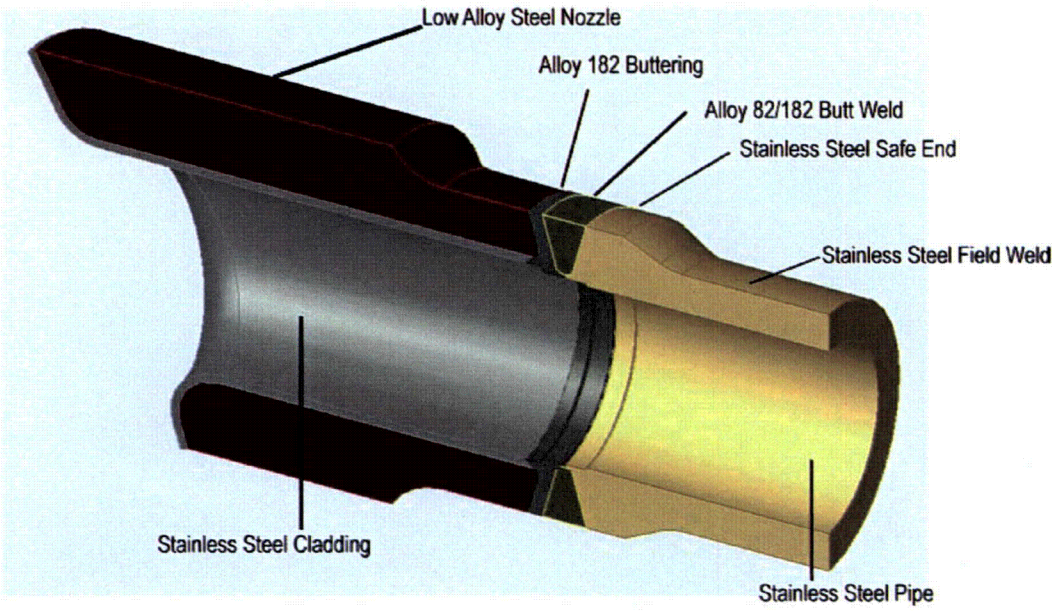

Figure 1-3
Example CE Design Pressurizer Safety/Relief Nozzle

2
PLANT INPUTS

This section summarizes the extensive weld-specific dimensional, piping load, fabrication, and weld repair history inputs that were collected for the group of 51 subject pressurizer nozzles. Detailed geometry and piping load inputs were collected for each subject weld to ensure that all welds are appropriately addressed by the crack growth sensitivity matrix (Section 7) developed as part of this study. Weld-specific fabrication and weld repair data were also collected as a key input to the welding residual stress simulations addressing the subject population (Section 3).

2.1 Geometry Cases

Among the nine plants covered in this report, there are a total of 51 pressurizer dissimilar metal welds of concern comprising: a) 35 safety and relief (S&R) nozzles, b) 8 surge nozzles, and c) 8 spray nozzles. Nozzle details are also included for a reference Plant J (Wolf Creek). Details of all nozzles at all plants are discussed fully in Appendix A [5,7]. The nozzle geometry information for the nozzles are summarized in Table 2-1 and Figure 2-1. The 51 nozzles may be further categorized into the following nozzle geometry cases. Note that nozzles with the same overall geometry may have been manufactured differently; see Section 2.3 for additional discussion.

2.1.1 Safety/Relief Nozzles

- Types 1a and 1b: Westinghouse design without liner, connected to 6″ pipe, used at plants A, E, H, and J (Type 1a) and plant F (Type 1b).
- Types 2a and 2b: Westinghouse design with liner directly covering DM weld, connected to 6″ pipe, used at plants B, C, and G.
- Type 3: CE design (no liner), connected to 6″ pipe, used at plants D and I.

2.1.2 Spray Nozzles

- Type 4: Westinghouse design with liner (does not extend to most of DM weld), connected to 4″ pipe, used at plants A, E, and J.
- Type 5: Westinghouse design with liner directly covering DM weld, connected to 4″ pipe, used at plants B, C, and G.
- Type 6: Westinghouse design without liner, connected to 6″ pipe, used at plant F.
- Type 7: CE design (no liner, sleeve not extending to DM weld), connected to 4″ pipe, used at plants D and I.

2.1.3 Surge Nozzles

- Type 8: Westinghouse design, sleeve directly covers DM weld area, connected to 14″ pipe. Used at plants A, B, C, E, F, G, H, and J. Note that this weld has already been mitigated at plant F.
- Type 9: CE design, DM weld machined at ID, sleeve does not extend to DM weld, connected to 12″ pipe. Used at plants D and I.

2.2 Piping Load Inputs

2.2.1 Pressure, Dead Weight, and Normal Thermal Loads

The piping loads for the 51 subject nozzle welds at the nine plants were also provided in References [5,7]. The loads are summarized in Figure 2-2 through Figure 2-6. In these figures, each point along the x-axis of the plots represents an individual nozzle weld. From left to right, the safety/relief nozzles at all plants are grouped together, followed by the spray nozzles, with the surge nozzles at the far right. The axial loads are displayed in Figure 2-2 and the bending moment loads are displayed in Figure 2-3 and Figure 2-4. Pressure and deadweight stresses (i.e., primary stresses) are displayed in Figure 2-5, and primary plus normal operating thermal stresses are displayed in Figure 2-6. As noted in Section 5, the primary plus normal operating thermal stress is used to calculate the critical flaw size.

For the purpose of showing the relative magnitudes of the membrane stress in these figures, the ASME Section XI Code definition $pD_o/4t$ where p is the pressure, D_o is the outside diameter, and t is the wall thickness has been used for the pressure loading component. Because this ASME Code definition is based on the outside diameter, it conservatively captures the effect of pressure acting on the crack face. However, in the crack growth and crack stability calculations performed for the sensitivity matrix of Section 7, the end cap pressure loading is based on the inside diameter cross sectional area plus the crack area, which depends on the particular calculated crack profile. The piping load stresses presented in Section 2 are independent of any particular crack profile assumption.

2.2.2 Surge Line Thermal Stratification Effects

An additional load condition that is unique to the surge nozzles (among the nozzles considered) is thermal stratification. Thermal stratification occurs in the surge line of every operating plant, due to the temperature difference between the pressurizer and the hot leg, which are connected by the surge line. The stratification produces a piping bending load, which can affect the surge nozzle safe end region. The normal operating thermal stratification loadings existing on the piping system during steady state operation are typically not significantly different from the normal operating thermal expansion loadings without thermal stratification (and sometimes ameliorate the loadings). Therefore, normal operating thermal stratification loadings are not considered in the crack growth or critical crack size analysis. It is noted that Reference [5] includes loads under the heading "Normal Thermal Stratification". However, recent investigation has revealed that, in some cases, the loads listed in this table are for other, more limiting, cases and should not be considered.

The stratification loads for some plants become significant during heat-up and cooldown of the plant, when the pressurizer and hot leg temperature differential may be larger. The limiting thermal loads for all surge nozzles are reported in Reference [7]; these loads are the entire maximum thermal load including all other effects, such as piping expansion. This table also notes that the limiting thermal load sometimes occurs during the normal operating condition (i.e., no thermal stratification). A series of comparison figures are included in this report comparing the normal and limiting thermal loads. In each figure, the primary (pressure plus dead weight) plus normal thermal loads are compared to the primary plus limiting thermal loads. Figure 2-7 compares the axial (membrane, Pm) stress between the two conditions at all plants; Figure 2-8 compares the bending (Pb) stress between the two conditions at all plants; and Figure 2-9 compares the combined membrane plus bending stress (Pm+Pb) between the two conditions at all plants. The ratio between the primary plus normal thermal and primary plus limiting thermal conditions for the Pm, Pb, and Pm+Pb stresses are compared in Figure 2-10.

As shown in Figure 2-10, when the normal and limiting stresses differ, they differ only in bending stress. Additionally, the primary plus normal thermal stress at any plant is no less than 45% of the corresponding primary plus limiting thermal stress, and, in many cases, it is closer to 100% of the primary plus limiting thermal stress. Given that Appendix B and Appendix C include separate calculations detailing how thermal bending loads would be expected to significantly relax in the presence of a large circumferential flaw, calculation of the critical flaw size using primary plus normal thermal loads is considered appropriate.

2.3 Weld Fabrication

The fabrication information for the 51 subject nozzle welds is summarized in Table 2-1. As described in Appendix A, the fabrication process for all nozzles falls under one of two general classifications identified in Table A-1, "Back-Weld" or "Machined." All the nozzles at a given plant share the same general fabrication process; i.e., no plant has some nozzles fabricated per the "Back-Weld" classification and others per "Machined." The two processes are summarized as follows; further detail is provided in Appendix A [5,7].

2.3.1 "Back-Weld" Process

The "Back-Weld" process uses a U-groove type design with a specified back-weld; i.e., a weld on the "back" side (in this case the ID side) of the weld joint. In this design, the two sides of the weld meet at an initial land that is 0.060 inches thick. Initial passes are applied to melt through the land and join the two sections. The weld is performed from ID to OD from the outside of the weld preparation. Once the initial weld is complete, the inside surface at the land joint is dye penetrant inspected, and the ID is ground until no separation is observed between the two sides of the land. While the design of the initial passes was intended to melt through and join the land, it is possible that the land region was ground in a fully circumferential manner to the approximate thickness of the land. Any material removed by grinding was filled in with a back-weld out to the ID surface. The complete weld was then radiographed, and repairs were made as necessary.

In the case of the surge nozzle, an additional step is applied following the radiograph/repair process. Following this process, a weld cladding layer (referred to as a fill-in weld) was deposited over the ID of the weld region to create a flat mating surface for the thermal sleeve. At its thickest point, the fill-in weld is about 0.3 inches thick. The fill-in weld layer was not radiographed.

Plants with nozzles manufactured using the "back-weld" process are A, B, C, F, G, and J.

2.3.2 "Machined" Process

The nozzle weld preparation design for the plants that use the "Machined" process differs from the "Back-Weld" process in that the ID of the weld prep was smaller than the desired finished ID. The weld is completed from ID to OD. After the weld is complete, the inside surface material is machined away to the desired finished dimension. Typically, in this type of joint, the initial root passes are machined away as part of the final machining to the finished ID. Surge nozzles fabricated using the "Machined" process do not have a fill-in weld layer.

Plants with nozzles manufactured using the "Machined" process are E and H (Westinghouse design) and D and I (CE design). As noted in Section A.5, the original design for plants E and H was to use a "Back-Weld" process; the change was made during the fabrication of the pressurizer and is not reflected in the design drawings shown in Appendix A.

2.4 Weld Repair History

The weld repair history for the 51 subject nozzle welds is noted in Table 2-1, and is described in greater detail in Table 2-2 [5,6,8]. Table 2-2 shows, when available, the number, depth, and length of the repairs for each weld.

Table 2-1
Nozzle Geometry and Repair History Summary Table

Plant Code	Relief											Safety A										
	Design #	Piping NPS	Liner?	Land Thick (in.)	Fill-In Weld Thick. (in.)	DM Weld t (in.)	DM Weld R_i/t	Weld Sep. (in.)	Butter Weld Repairs	ID Weld Repairs	OD Weld Repairs	Design #	Piping NPS	Liner?	Land Thick (in.)	Fill-In Weld Thick. (in.)	DM Weld t (in.)	DM Weld R_i/t	Weld Sep. (in.)	Butter Weld Repairs	ID Weld Repairs	OD Weld Repairs
Plant A	1a	6"	N	0.06	None	1.29	2.0	2.2	NR	NR	NR	1a	6"	N	0.06	None	1.29	2.0	2.2	NR	NR	R4
Plant E	1a	6"	N	Mach	None	1.29	2.0	2.2	NR	NR	R	1a	6"	N	Mach	None	1.29	2.0	2.2	NR	NR	NR
Plant H	1a	6"	N	Mach	None	1.29	2.0	2.2	NR	NR	NR	1a	6"	N	Mach	None	1.29	2.0	2.2	NR	R	R
Plant B	2a	6"	Y	0.06	None	1.07	2.6	2.6	NR	NR	R1	2a	6"	Y	0.06	None	1.07	2.6	2.6	NR	NR	NR
Plant G	2a	6"	Y	0.06	None	1.07	2.6	2.6	NR	NR	NR	2a	6"	Y	0.06	None	1.07	2.6	2.6	NR	NR	NR
Plant C	2b	6"	Y	0.06	None	1.07	2.6	2.3	NR	NR	NR	2b	6"	Y	0.06	None	1.07	2.6	2.3	NR	NR	NR
Plant F	1b	6"	N	0.06	None	1.41	1.8	3.3	NR	NR	NR	1b	6"	N	0.06	None	1.41	1.8	3.3	NR	NR	NR
Plant D	3	6"	N	Mach	None	1.41	1.8	6.8	NR	NR	NR	3	6"	N	Mach	None	1.41	1.8	6.8	R	NR	NR
Plant I	3	6"	N	Mach	None	1.41	1.8	6.8	NR	Rx2		3	6"	N	Mach	None	1.41	1.8	6.8	NR	NR	NR
Plant J	1a	6"	N	0.06	None	1.29	2.0	2.2	Rx5	R1	R1	1a	6"	N	0.06	None	1.29	2.0	2.2	R	R2	NR

Notes:

1. For Designs #2a, #2b, and #5, liner directly covers DM weld.
2. For Design #4, liner does not extend to most of DM weld.
3. For Designs #4, #5, and #6, sleeve covers but does not contact DM weld.
4. For Design #8, sleeve directly covers DM weld.
5. For Designs #7 and #9, sleeve does not extend to DM weld.
6. NR = No weld repairs reported
7. Rn = Repairs reported (n indicates number of defect or repaired areas if reported; "x" indicates repeat weld repair operations)
8. All pressurizer nozzle DM welds in Plant H are reported to be Alloy 82, not Alloy 82/182.
9. Mach = Initial land thickness of 0.09" to 0.10" machined away as part of weld prep design.
10. Plant I capped relief nozzle listed under "Relief" heading.

Table 2-1 (cont'd)
Nozzle Geometry and Repair History Summary Table

Plant Code	Safety B											Safety C										
	Design #	Piping NPS	Liner?	Land Thick (in.)	Fill-In Weld Thick. (in.)	DM Weld t (in.)	DM Weld R_f/t	Weld Sep. (in.)	Butter Weld Repairs	ID Weld Repairs	OD Weld Repairs	Design #	Piping NPS	Liner?	Land Thick (in.)	Fill-In Weld Thick. (in.)	DM Weld t (in.)	DM Weld R_f/t	Weld Sep. (in.)	Butter Weld Repairs	ID Weld Repairs	OD Weld Repairs
Plant A	1a	6"	N	0.06	None	1.29	2.0	2.2	NR	R1	NR	1a	6"	N	0.06	None	1.29	2.0	2.2	NR	NR	NR
Plant E	1a	6"	N	Mach	None	1.29	2.0	2.2	NR	NR	NR	1a	6"	N	Mach	None	1.29	2.0	2.2	NR	R	NR
Plant H	1a	6"	N	Mach	None	1.29	2.0	2.2	NR	NR	NR	1a	6"	N	Mach	None	1.29	2.0	2.2	NR	NR	NR
Plant B	2a	6"	Y	0.06	None	1.07	2.6	2.6	NR	NR	NR	2a	6"	Y	0.06	None	1.07	2.6	2.6	NR	NR	NR
Plant G	2a	6"	Y	0.06	None	1.07	2.6	2.6	NR	NR	NR	2a	6"	Y	0.06	None	1.07	2.6	2.6	NR	NR	NR
Plant C	2b	6"	Y	0.06	None	1.07	2.6	2.3	NR	NR	NR	2b	6"	Y	0.06	None	1.07	2.6	2.3	NR	NR	NR
Plant F	1b	6"	N	0.06	None	1.41	1.8	3.3	NR	NR	NR	1b	6"	N	0.06	None	1.41	1.8	3.3	NR	NR	NR
Plant D	3	6"	N	Mach	None	1.41	1.8	6.8	NR	NR	NR	3	6"	N	Mach	None	1.41	1.8	6.8	NR	NR	NR
Plant I	3	6"	N	Mach	None	1.41	1.8	6.8	NR	NR	NR	No Safety C										
Plant J	1a	6"	N	0.06	None	1.29	2.0	2.2	NR	R6x2	NR	1a	6"	N	0.06	None	1.29	2.0	2.2	NR	NR	NR

Notes:

1. For Designs #2a, #2b, and #5, liner directly covers DM weld.
2. For Design #4, liner does not extend to most of DM weld.
3. For Designs #4, #5, and #6, sleeve covers but does not contact DM weld.
4. For Design #8, sleeve directly covers DM weld.
5. For Designs #7 and #9, sleeve does not extend to DM weld.
6. NR = No weld repairs reported
7. Rn = Repairs reported (n indicates number of defect or repaired areas if reported; "x" indicates repeat weld repair operations)
8. All pressurizer nozzle DM welds in Plant H are reported to be Alloy 82, not Alloy 82/182.
9. Mach = Initial land thickness of 0.09" to 0.10" machined away as part of weld prep design.
10. Plant I capped relief nozzle listed under "Relief" heading.

Table 2-1 (cont'd)
Nozzle Geometry and Repair History Summary Table

Plant Code	Spray (all have thermal sleeve)											Surge (all have thermal sleeve)										
	Design #	Piping NPS	Liner?	Land Thick (in.)	Fill-In Weld Thick. (in.)	DM Weld t (in.)	DM Weld R_i/t	Weld Sep. (in.)	Butter Weld Repairs	ID Weld Repairs	OD Weld Repairs	Design #	Piping NPS	Liner?	Land Thick (in.)	Fill-In Weld Thick. (in.)	DM Weld t (in.)	DM Weld R_i/t	Weld Sep. (in.)	Butter Weld Repairs	ID Weld Repairs	OD Weld Repairs
Plant A	4	4"	Y	0.06	None	0.90	2.2	~2.3	NR	NR	NR	8	14"	N	0.06	0.30	1.58	3.8	3.4	NR	R5	R3
Plant E	4	4"	Y	Mach	None	0.90	2.2	~2.3	R	NR	R	8	14"	N	Mach	None	1.58	3.8	3.4	NR	R3	NR
Plant H	Already PDI examined											8	14"	N	Mach	None	1.58	3.8	3.4	NR	NR	NR
Plant B	5	4"	Y	0.06	None	0.78	2.7	2.2	NR	NR	NR	8	14"	N	0.06	0.30	1.58	3.8	3.4	R1	R1x2	R2
Plant G	5	4"	Y	0.06	None	0.78	2.7	2.2	NR	NR	NR	8	14"	N	0.06	0.30	1.58	3.8	3.4	NR	NR	NR
Plant C	5	4"	Y	0.06	None	0.78	2.7	~2.2	NR	NR	NR	8	14"	N	0.06	0.29	1.56	3.8	3.5	NR	NR	NR
Plant F	6	6"	N	0.06	None	1.15	2.5	3.6	R	NR	NR	Already structural overlayed										
Plant D	7	4"	N	Mach	None	1.06	1.4	3.3	NR	NR	NR	9	12"	N	Mach	None	1.47	3.4	3.0	NR	NR	NR
Plant I	7	4"	N	Mach	None	1.06	1.4	3.3	NR	NR	NR	9	12"	N	Mach	None	1.47	3.4	3.0	NR	Rx2	
Plant J	4	4"	Y	0.06	None	0.90	2.2	~2.3	R	NR	NR	8	14"	N	0.06	0.30	1.58	3.8	3.4	R2	R1	NR

Notes:

1. For Designs #2a, #2b, and #5, liner directly covers DM weld.
2. For Design #4, liner does not extend to most of DM weld.
3. For Designs #4, #5, and #6, sleeve covers but does not contact DM weld.
4. For Design #8, sleeve directly covers DM weld.
5. For Designs #7 and #9, sleeve does not extend to DM weld.
6. NR = No weld repairs reported
7. Rn = Repairs reported (n indicates number of defect or repaired areas if reported; "x" indicates repeat weld repair operations)
8. All pressurizer nozzle DM welds in Plant H are reported to be Alloy 82, not Alloy 82/182.
9. Mach = Initial land thickness of 0.09" to 0.10" machined away as part of weld prep design.
10. Plant I capped relief nozzle listed under "Relief" heading.

Table 2-2
Weld Repair Summary Table

Table Line	Plant Code	Nozzle Type	Nozzle Count	Design #	Buttering or Weld	ID/OD (% circ.)	Alloy 82 or 182	PWHT after Repair?	# Defect or Repair Areas	Defect/Repair Area #1		Defect/Repair Area #2		Defect/Repair Area #3		Defect/Repair Area #4		Defect/Repair Area #5		Defect/Repair Area #6	
										Length (in.)	Depth (in.)	Length (in.)	Depth (in.)	Length (in.)	Depth (in.)	Length (in.)	Depth (in.)	Length (in.)	Depth (in.)	Length (in.)	Depth (in.)
1	A	Safety A	1	1a	weld	OD	N/A	N/A	4	N/A	~1/2	N/A	~1/2	N/A	~1/2	N/A	~1/2				
2	A	Safety B	2	1a	weld	ID	N/A	N/A	1	1/2	5/8										
3	E	Relief	3	1a	weld	OD	N/A	N	N/A	N/A	N/A										
4	E	Safety C	4	1a	weld	ID<22%	N/A	N	N/A	N/A	N/A										
5	H	Safety A	5	1a	weld	ID	82	Y	N/A	N/A	N/A										
6						OD	82	Y	N/A	N/A	N/A										
7	B	Relief	6	2a	weld	OD	182	N/A	1	0.5	0.375										
8	D	Safety A	7	3	butter	N/A	N/A	Y	N/A	N/A	N/A										
9	I	Relief	8	3	weld	ID+OD	82/182	N	8	N/A	N/A										
10	E	Spray	9	4	butter	ID	82	Y	N/A	N/A	~0.3										
11					weld	OD	N/A	N	N/A	N/A	N/A										
12	F	Spray	10	6	butter	N/A	82	Y	N/A	N/A	N/A										
13	A	Surge	11	8	weld	ID	N/A	N/A	5	1.5	5/16	3.75	0.5	2	3/16	2.5	5/16	2	5/16		
14						OD	N/A	N/A	3	2.5	0.5	2	0.5	1	3/16						
15	E	Surge	12	8	weld	ID<10%	82	N	3	N/A	N/A	N/A	N/A	N/A	N/A						
16	B	Surge	13	8	butter	N/A	82	Y	1	N/A	N/A										
17					weld	OD	182	N/A	2	1.75	0.875	1.5	1								
18						ID	182	N/A	1	1.0	0.625										
19						ID	182	N/A	1	4	0.75										
20	I	Surge	14	9	weld	ID+OD	82/182	N	4	N/A	N/A										
WC1	J	Relief	WC1	1a	butter	N/A	82/182	Y	N/A	N/A	N/A										
WC2						ID+OD	82	Y	2	1/2	7/16ID	1	7/16OD								
WC3						OD	182	Y	1	1	3/4										
WC4						ID	82	Y	3	3/4	3/4	2-1/4	3/4	1/2	3/4						
WC5						OD	182	Y	3	1	3/4	2-1/4	3/4	1/2	3/4						
WC6					weld	OD	82	N/A	1	1-1/4	1/2										
WC7						ID	82	N/A	1	1/2	1/2										
WC8	J	Safety A	WC2	1a	butter	N/A	182	Y	N/A	N/A	1/8										
WC9					weld	ID	82	N/A	2	1-1/4	11/32	7/8	11/32								
WC10	J	Safety B	WC3	1a	weld	ID	82	N/A	6	2-1/2	3/4	1	1/2	1-1/2	1/2	1	1/2	2-1/2	3/4	2-1/2	3/4
WC11							82	N/A	6	1-1/2	1/2	1-1/4	1	3/4	7/8	1-1/2	3/8	1	1-1/16	1/2	1/2
WC12	J	Spray	WC4	4	butter	lip/bondline	82	Y	N/A	N/A	N/A										
WC13	J	Surge	WC5	8	butter	OD	182	Y	2	7/8	9/16	1-1/8	1								
WC14					weld	ID	82	Y	1	1	7/16										

Notes:

1. For Designs #2a, #2b, and #5, liner directly covers DM weld.
2. For Design #4, liner does not extend to most of DM weld.
3. For Designs #4, #5, and #6, sleeve covers but does not contact DM weld.
4. For Design #8, sleeve directly covers DM weld.
5. N/A = Information not available

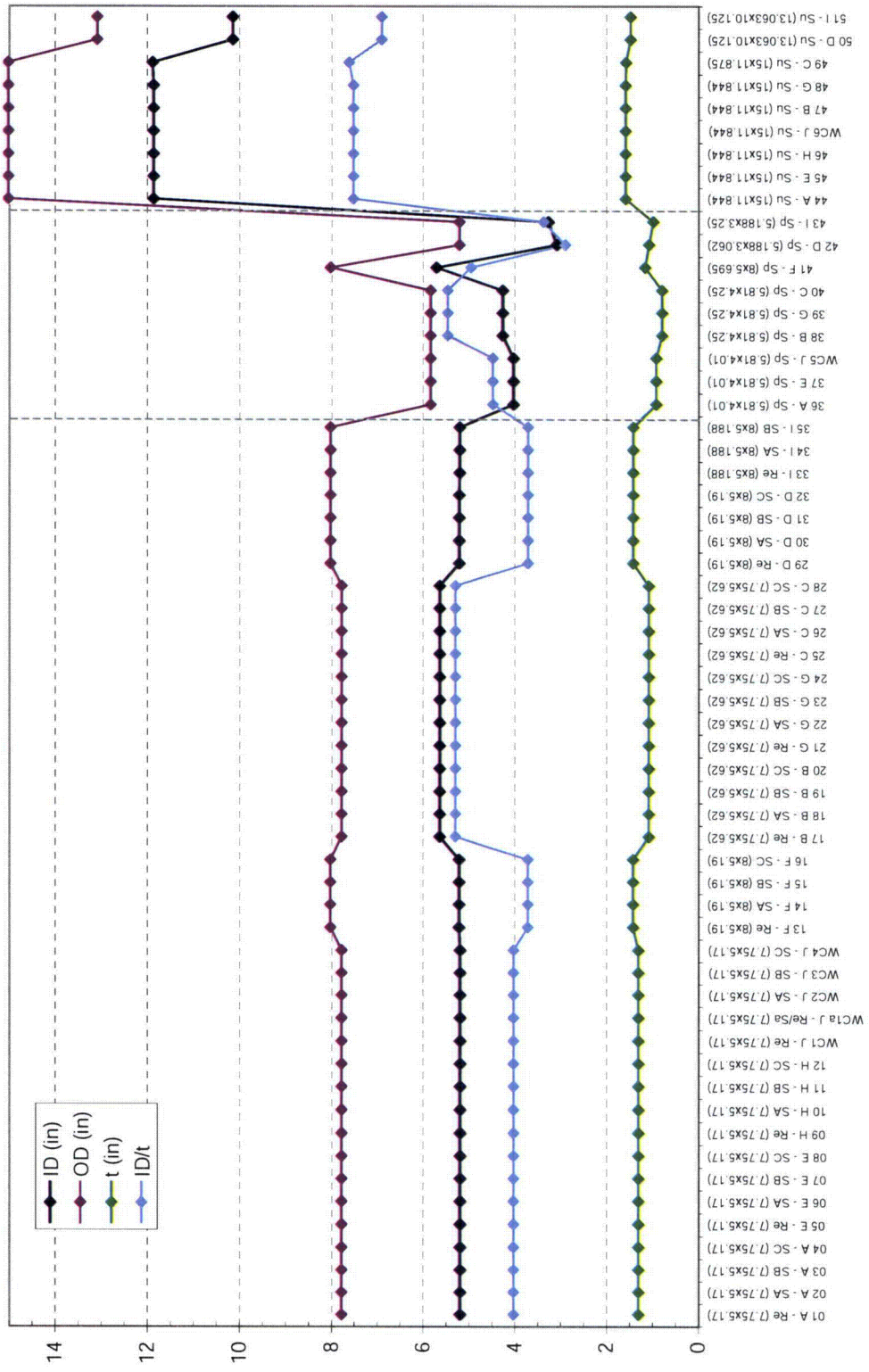

Figure 2-1
Nominal Basic Design Dimensions for Each Subject Weld

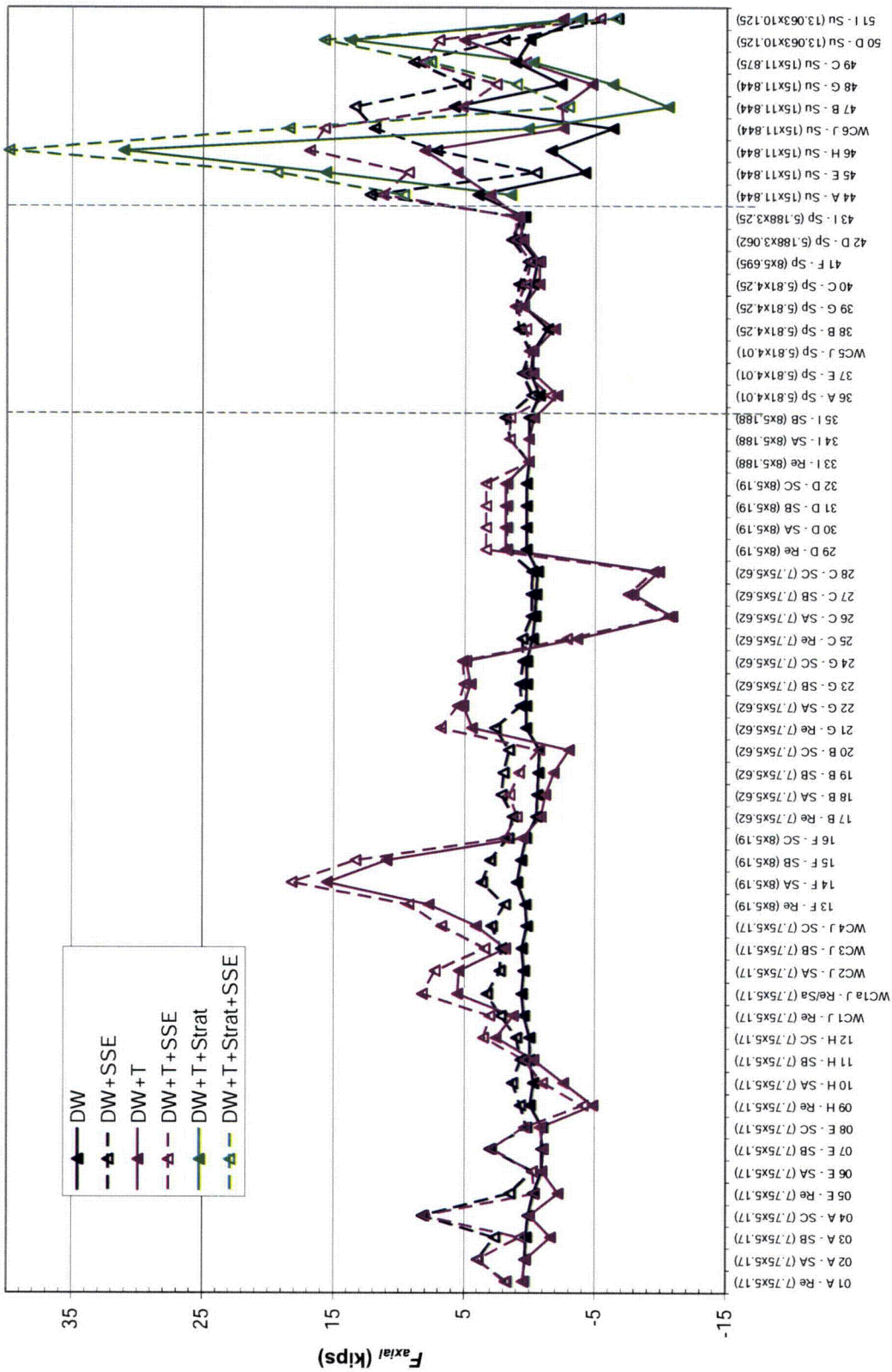

Figure 2-2
Nominal Axial Piping Loads (Not Including Endcap Pressure Load)

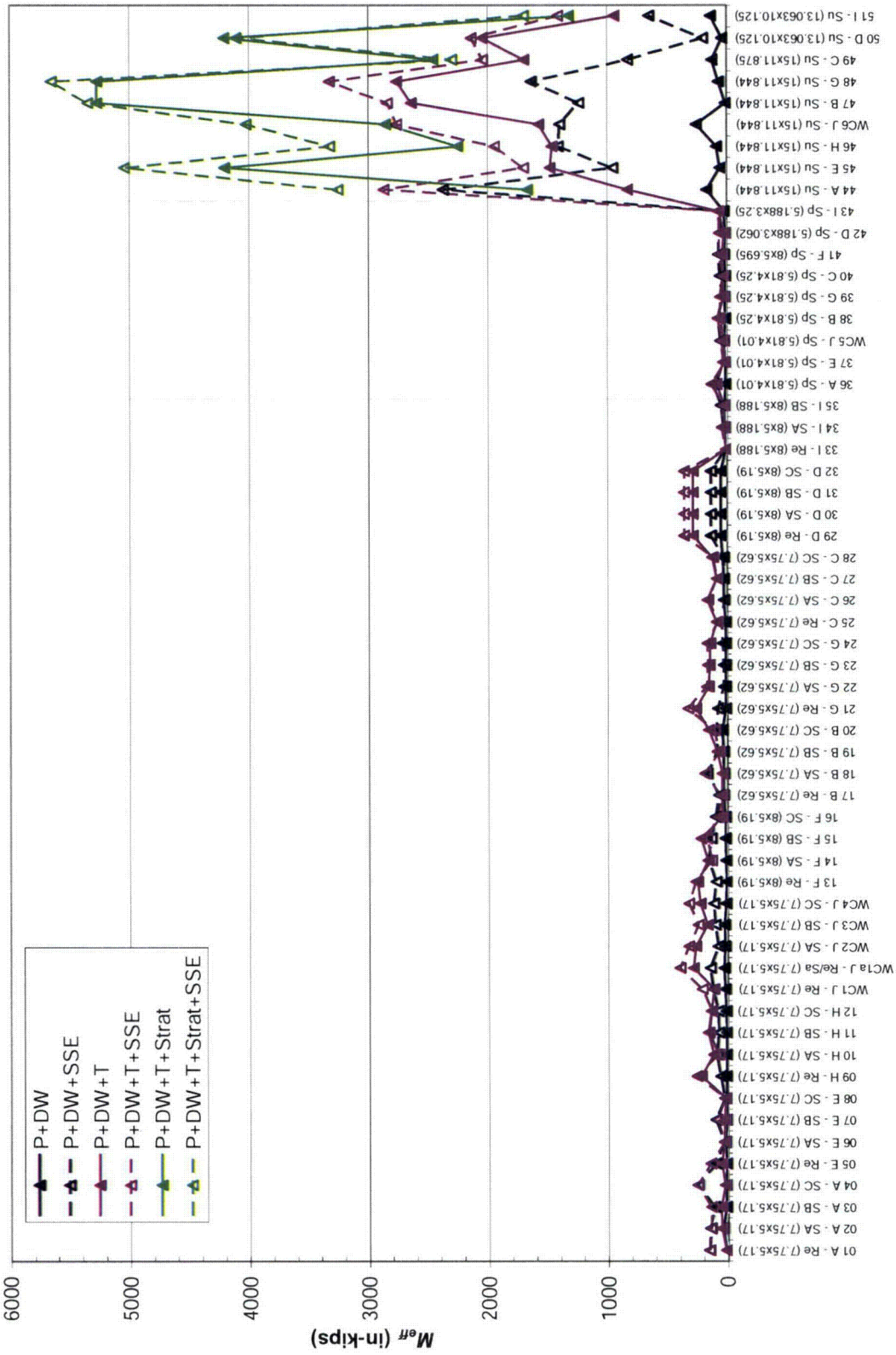

Figure 2-3
Nominal Effective Bending Moment Loads (Full Scale)

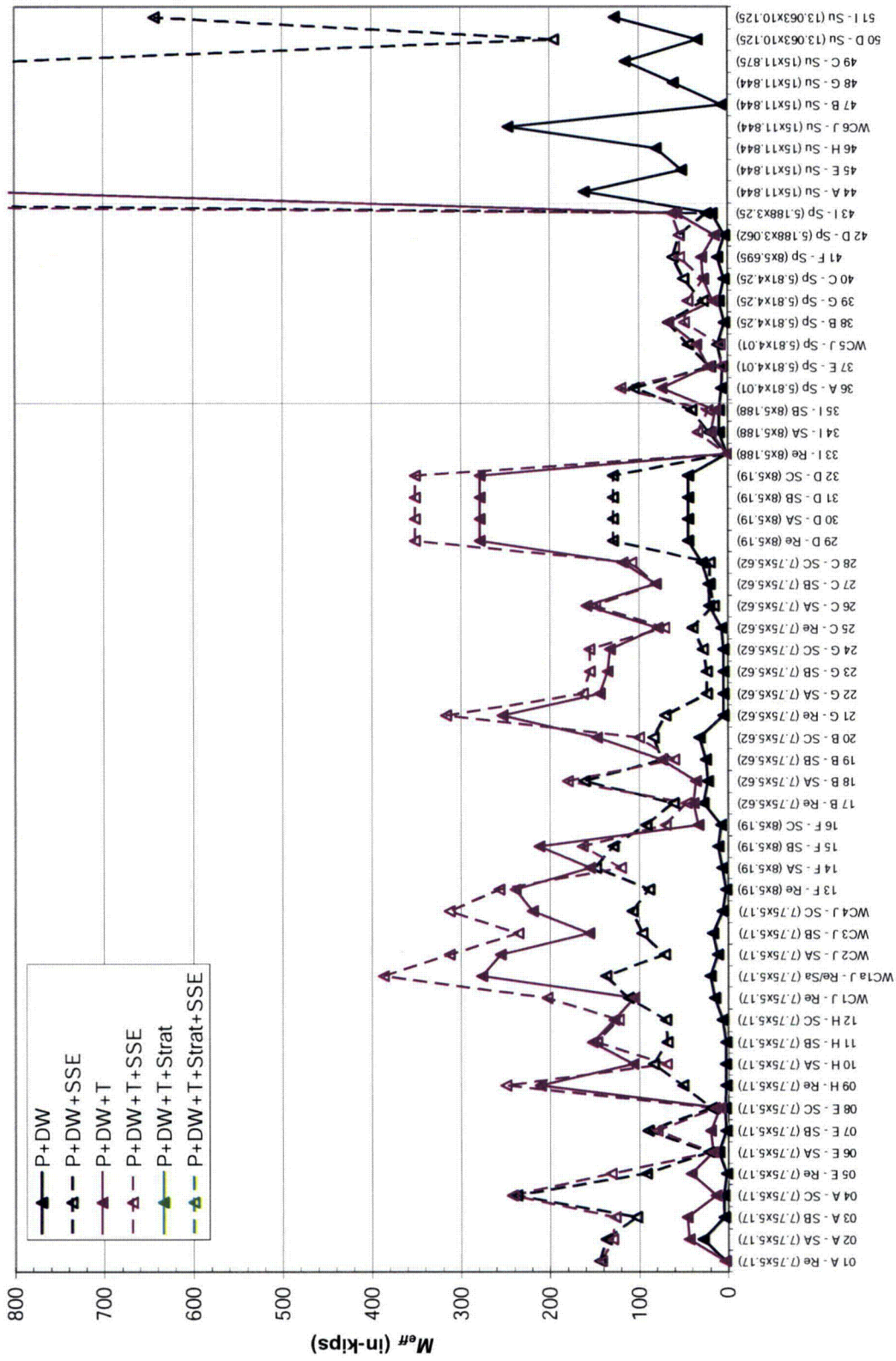

Figure 2-4
Nominal Effective Bending Moment Loads (Partial Scale)

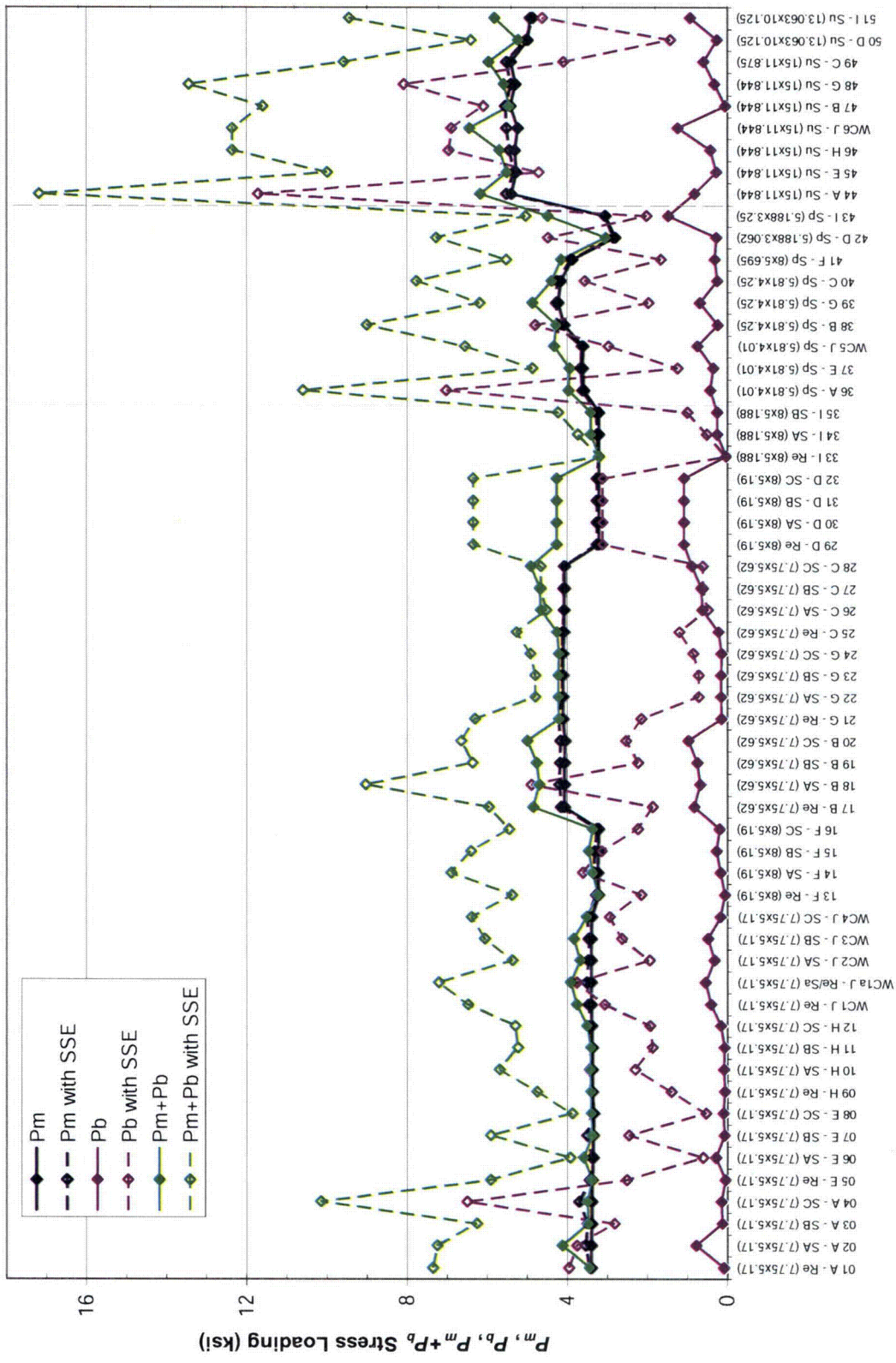

Figure 2-5
ASME Code Nominal Stress Loading for Pressure and Dead Weight Loading

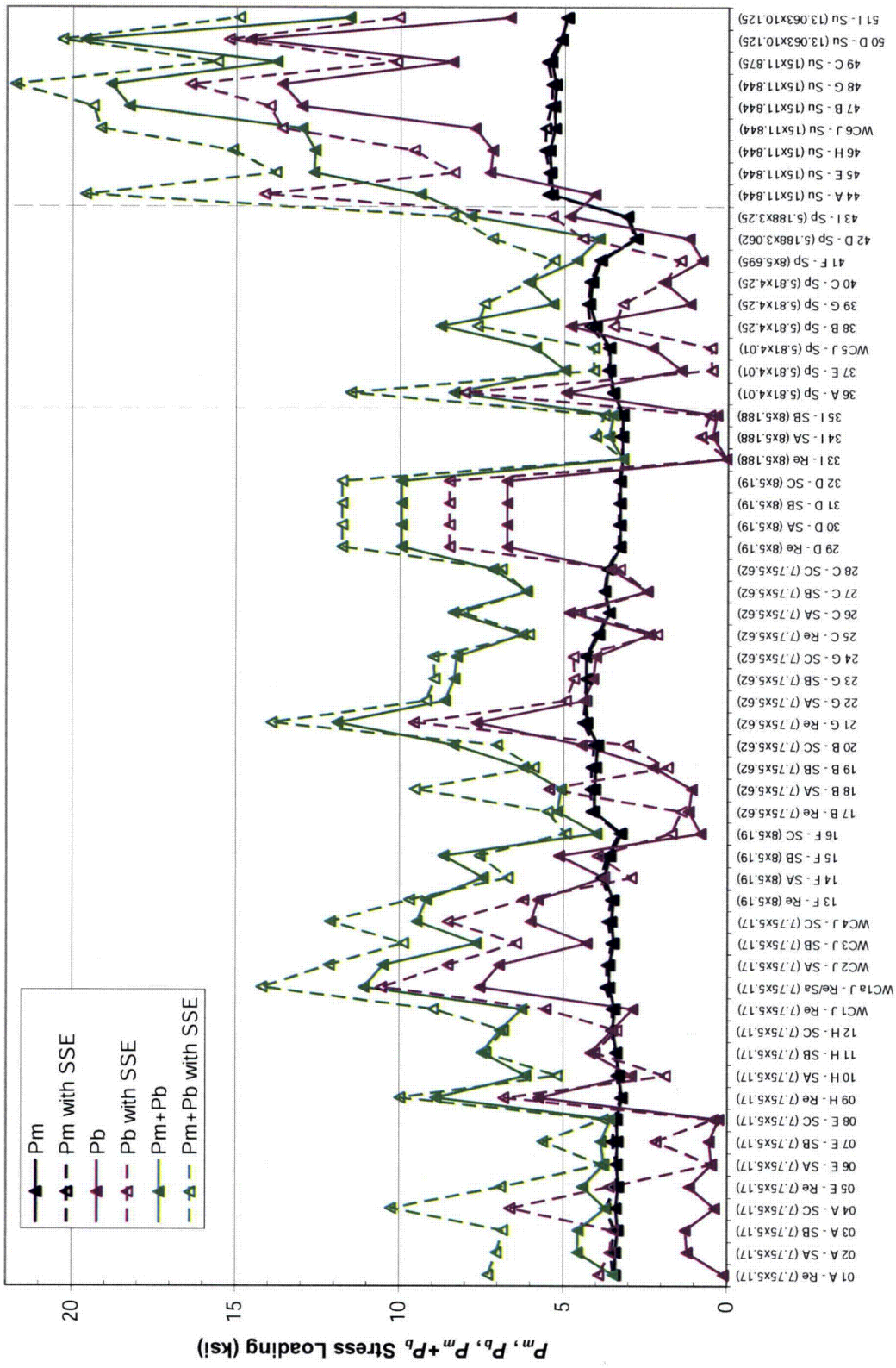

Figure 2-6
ASME Code Nominal Stress Loading for Pressure, Dead Weight, and Normal Thermal Loading

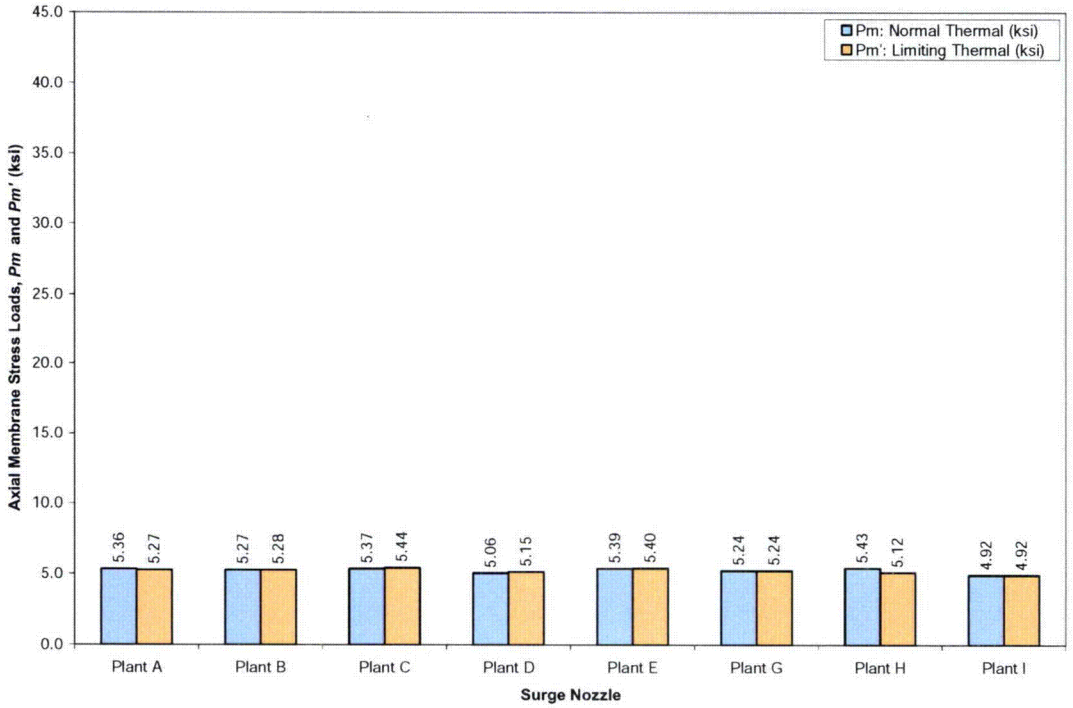

Figure 2-7
Axial Membrane Stress Loading for Surge Nozzles: Pressure and Dead Weight plus Normal or Limiting Thermal Loads

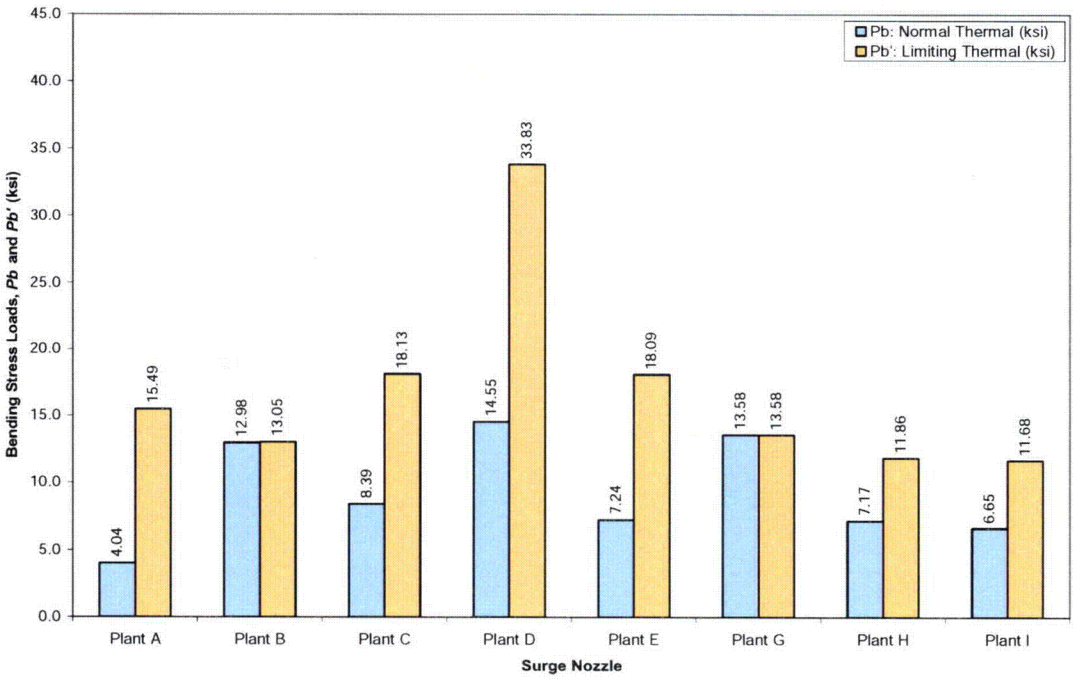

Figure 2-8
Thick-Wall Bending Stress Loading for Surge Nozzles: Pressure and Dead Weight plus Normal or Limiting Thermal Loads

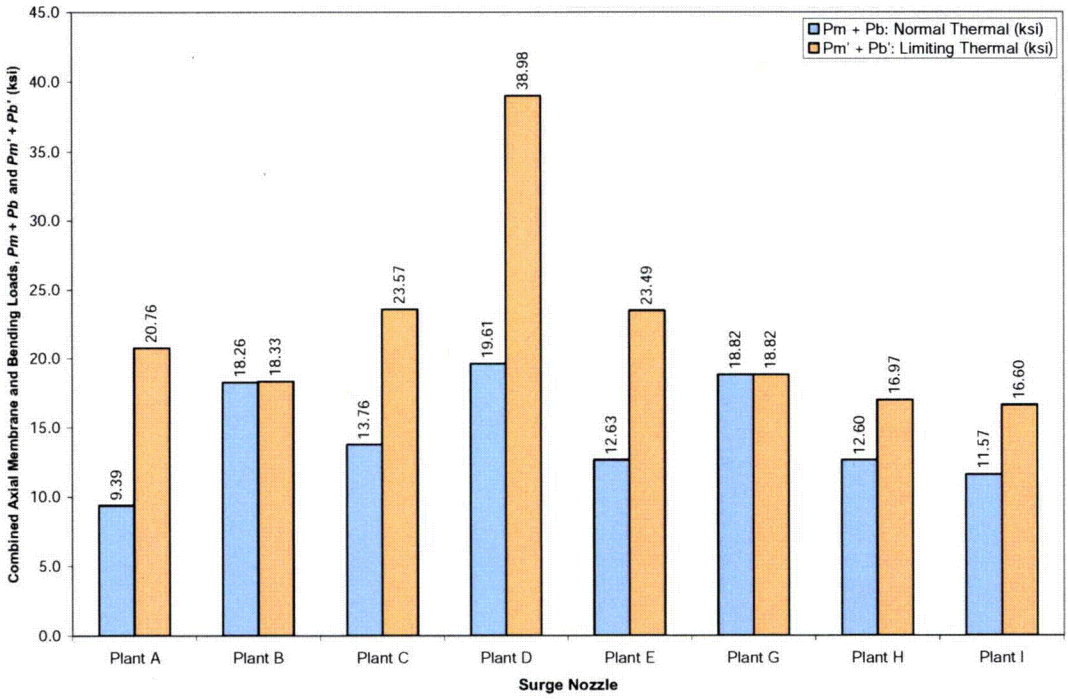

Figure 2-9
Combined Membrane Pm and Bending Pb Stress Loading for Surge Nozzles: Pressure and Dead Weight plus Normal or Limiting Thermal Loads

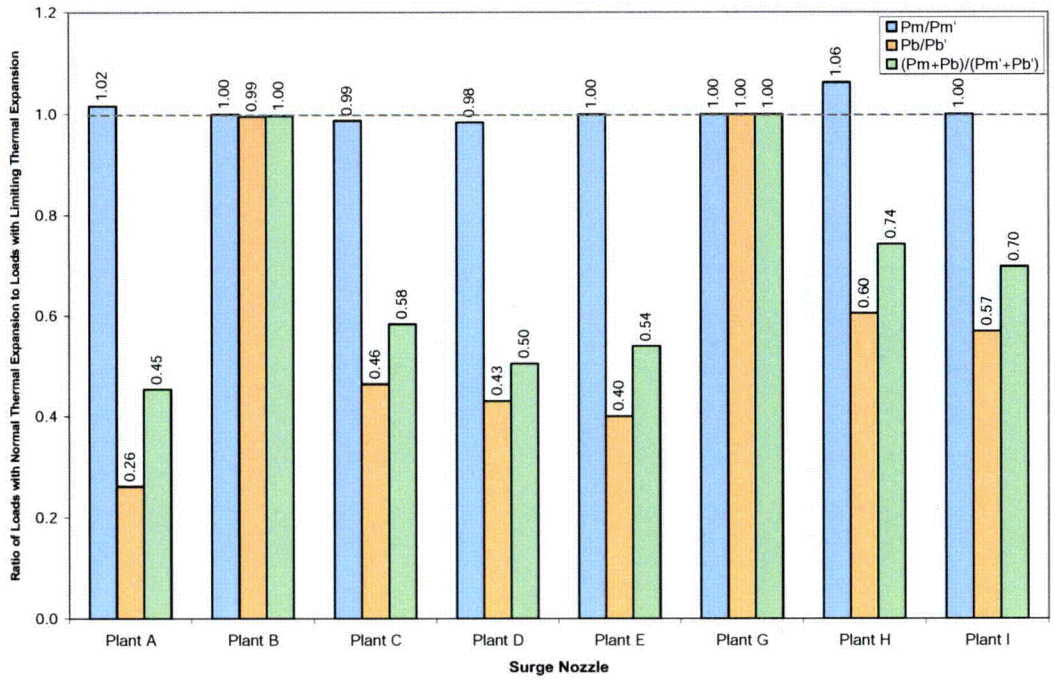

Figure 2-10
Ratio of Total Stress Loads with Normal Thermal Loads versus Limiting Thermal Loads

3
WELDING RESIDUAL STRESS

The purpose of this section is to describe analyses which investigate the residual stress distributions in a range of nozzle to safe end dissimilar metal welds in the as welded condition and in the presence of weld repairs. The axial stress distributions calculated from these analyses are used as inputs to the matrix of fracture mechanics calculations, described in Section 7 of this report. Finite element analysis is used to simulate the thermal and mechanical effects of the welds and any repairs of the weld region. Select details regarding the model and relevant stress results are provided in the remainder of this section. Additionally, the analysis results are discussed in the context of additional work on welding residual stresses identified in existing literature. Finally, validation work on the welding residual stress methods used is discussed in this section.

3.1 Finite Element Analysis of Welding Residual Stress

3.1.1 Cases Considered

Safety/Relief Nozzle Cases

The safety and relief nozzles generally have the same geometry and configuration within the plants considered. Two similar configurations were considered for welding residual stress analysis: the Type 1a and Type 2b safety/relief nozzles described in Section 2. The difference between the two is that Type 1a safety/relief nozzles have no liner, and Type 2b nozzles have an ID liner. Figure 3-1 and Figure 3-2 show the geometry of the two safety/relief nozzle models considered. The following cases were analyzed:

- Nozzle butt weld alone with and without safe end to pipe weld
- Nozzle butt weld with weld buildup at safe end ID (with safe end weld)
- Nozzle butt weld with liner fillet weld (with safe end weld)
- Nozzle butt weld with 0.75-inch deep x 360° ID weld repair (no safe end weld)
- Nozzle butt weld with 0.75-inch deep x 20° (0.9 inch) ID weld repair (no safe end weld)

Surge Nozzle Cases

Two different surge nozzle models were considered: one for the Type 8 nozzles and one for the Type 9 nozzles. Figure 3-3 and Figure 3-4 show the geometry of the Type 8 and Type 9 nozzle models, respectively. The following surge nozzle cases were considered:

- Type 8 nozzle butt weld plus fill-in weld, with and without safe end to pipe weld
- Type 8 nozzle butt weld with 5/16-inch deep x 360° ID weld repair plus fill-in weld (with safe end weld)
- Type 9 nozzle butt weld alone, includes ID machining

It is noted that since the Type 8 nozzle repair region encompasses the portion of the land that is ground and re-welded, this step is not included for the repair model.

Bounded Cases

The nozzle geometries considered in this analysis do not encompass the entire range of nozzle geometries or fabrication processes identified in Section 2 and Appendix A. However, the selection of cases is expected to either bound or represent the results of the remaining cases. The CE-design Type 3 safety/relief nozzles and the safety/relief and surge nozzles at plants E and H have a machined ID; these cases are expected to have a through-wall distribution similar to that of a CE-design Type 9 nozzle. As noted later in this section, this type of through-wall distribution is bounded by the other safety/relief and surge nozzle cases. Additionally, no spray nozzle geometry analysis cases (Types 4 through 7) are included; these smaller nozzles are similar to the safety/relief nozzles and are considered either represented or bounded by their analysis cases.

3.1.2 FEA Modeling and Methodology

Model Geometry and Boundary Conditions

Figure 3-3 shows the overall model geometry for the Type 8 surge nozzle butt weld analysis cases. As shown in the figure, the model includes the low alloy steel nozzle, the nozzle buttering, the stainless steel safe end, a section of stainless steel piping, and the welds attaching a) the nozzle to the safe end, and b) the safe end to the piping. Similar model geometry plots for the safety/relief nozzle cases and the Type 9 surge nozzle are included in Figure 3-1, Figure 3-2, and Figure 3-4. All but one of the analysis cases are performed using two-dimensional axisymmetric models. These models simulate a welding process that is simultaneous around the entire circumference of the model. This is appropriate given that the standard fabrication steps described in Section 2 are fully circumferential in nature. Repairs, however, are typically not fully circumferential. In order to consider the circumferential effects of a limited repair zone, one analysis case considers a 180° symmetric three-dimensional analysis of a weld followed by a repair. Figure 3-5 shows the three dimensional model used to simulate the safety/relief nozzle repair case. As noted above, this repair case considers a 0.9-inch long (ID surface) repair; because a half symmetric model is used, half the total repair length is included in the model.

The model geometries are developed from the nozzle, weld, and piping dimensions described in Section 2 and Appendix A. Where appropriate, minor simplifications are made to the overall geometry in developing the model geometry. For example, the rounded U-groove weld preparation geometry is squared off in the FEA model. Additionally, dimensions that are not specified in the drawings are approximated by scaling. A view of the finite element mesh for the

Type 8 surge nozzle, which also shows the layers used to simulate the weld process, is shown in Figure 3-6.

The welding residual stress model performs a thermal and structural analysis of the nozzle region. During the thermal analysis, convection cooling from the nozzle, safe end and piping to air at an ambient temperature of 70°F was modeled using a heat transfer coefficient of 5 BTU/hr-ft^2-°F, consistent with natural convection cooling in still air. Convection cooling of the weld elements was not included in the model, i.e., only the dominant effects of conduction cooling of the weld metal to the base metal sections was simulated. During the structural analysis, the nozzle end of the model was fixed in the axial direction. In addition, the entire plane of nodes at the opposite end of the pipe was coupled in the axial direction (constrained to have the same axial displacement) to simulate continuation of the pipe beyond the model boundary. This boundary condition is not in effect during the dissimilar metal weld, since the safe end is not constrained during the weld process. The length of stainless steel pipe in the model is about 10 inches, sufficient that local wall thickness effects have damped out. No representation is made for the axial stiffness of the remainder of the piping run beyond the model geometry. When the model is pressurized, internal pressure is applied to the wetted surface, and an endcap axial load was applied at the coupled side of the model.

The welding residual stress analysis was performed using ANSYS finite element analysis software. When two-dimensional axisymmetric analyses were performed, four-node planar thermal and structural elements were used to develop the FEA mesh; eight-node structural solid elements were used for the three dimensional analysis. Higher order elements were not used since they provide no greater accuracy for elastic-plastic analyses than the four-node planes and eight-node solids [9].

Material Properties

Four materials were used in the modeling of the nozzle butt welds: the nozzle is low alloy steel, the nozzle buttering and weld metal is Alloy 82/182, the safe end, safe end to pipe weld, and attached piping are stainless steel, and the safe end to piping attachment is a stainless steel weld. Temperature dependent thermal and mechanical properties were input for each of these materials. All materials were assumed to strain-harden using the von Mises yield criterion with a bilinear input curve and a tangent modulus of zero (elastic-perfectly plastic). When using ANSYS, this assumption gives more realistic stresses where a high degree of plastic strain occurs at elevated temperatures, such as within the welds and the base material HAZ.

Specific information regarding the properties for the materials is as follows. It is noted that the material property information listed below applies only to the welding residual stress model; different values may have been used for other calculations in other sections of this report (e.g., different yield strength for critical crack size).

Alloy 82/182 Weld and Buttering

The bilinear elastic limit for these materials is based on an average of the yield and tensile strengths reported in Reference [10]. An elastic limit of 75.0 ksi was used at 70°F, and the elastic limit at 653°F is 56.8 ksi. A Poisson's ratio of 0.29 was used; this value was assumed to be invariant with temperature. Additional material property data were taken from a number of

sources, including the 1992 ASME Boiler and Pressure Vessel Code [11], data provided by EdF for EPRI analyses [12], and Inconel product literature [10].

Low Alloy Steel Nozzle

The elastic limit values for the low alloy steel are based on typical values for the 0.2% offset yield strength of this material. An elastic limit of 50.0 ksi was used at 70°F, and the elastic limit at 653°F is 40.9 ksi. A Poisson's ratio of 0.29 was used; this value was assumed to be invariant with temperature. Additional material property data were taken from a number of sources, including the 1992 ASME Boiler and Pressure Vessel Code [11], low alloy steel data provided by EdF for EPRI analyses [12], and research by Karlsson [13].

Stainless Steel Base Metal

The stainless steel base metal (safe end and piping) uses elastic limit values that are based on the 0.2% offset yield strength for the material. It is recognized that a small region of base metal material adjacent to the dissimilar metal and stainless steel welds will be affected by the welding process and will have a higher effective yield strength. The effect of this difference is likely bounded by the overall uncertainty of the analysis. An elastic limit of 40.0 ksi was used at 70°F, and the elastic limit at 653°F is 28.4 ksi. A Poisson's ratio of 0.29 was used; this value was assumed to be invariant with temperature. Additional material property data were taken from a number of sources, including the 1992 ASME Boiler and Pressure Vessel Code [11], data provided by EdF for EPRI analyses [12], and research by Rybicki [14]. The values used in this analysis are identical to those used for BWR stainless steel shroud welds in [15]. Additionally, the CMTR data for the stainless steel piping materials from the plants considered in this report indicate that the values selected are appropriate (see Section 5.1).

Stainless Steel Weld Metal

The stainless steel material used to join the safe end to the piping uses material strength properties that differ from the stainless steel base metal described above. An elastic limit of 67.0 ksi was used at 70°F, and the elastic limit at 653°F is 49.8 ksi. The values for the elastic limit were taken from previous analytical work performed for BWR stainless steel shroud welds [15]. All other material property data for the weld material is the same as the base metal.

Analysis Load Steps

The welding residual stress analysis involves four general loading steps: (a) welding, (b) weld repair (if applicable), (c) hydrostatic testing, and (d) operating conditions. These processes are simulated as follows:

Welding Simulation

The welding process was simulated by combined thermal and structural analyses. A transient thermal analysis was used to generate nodal temperature distributions throughout the welding process. These nodal temperatures were then used as inputs to the structural analysis which calculates resultant thermally-induced stresses. The sequence of thermal analyses followed by

structural analyses was duplicated for each simulated weld pass. When the model is three-dimensional, the base welding simulation was performed in an axisymmetric fashion, with welding passes simulated as rings of weld metal. In all cases, the weld passes were simulated using layers of material, with layers approximately 0.1 inches thick.

A layer-based methodology has typically been used in previous industry welding residual stress analyses for butt welds. It is recognized that the actual welds are fabricated using discrete beads, rather than layers of weld metal. However, the specific sequence and pattern of the weld beads is frequently unknown. Using a layer based approach, with the layer thickness chosen to approximate the bead size, is a way to simulate the welding process while minimizing the impact of the simulated sequence on the analysis results. Additionally, simulating certain weld repair geometries is simplified when a layer geometry is implemented. In Section 3.3, the layer-based methodology used for this work is compared to actual measured residual stresses and to the analysis results for models where a specific bead-by-bead sequence was simulated. The results shown in Section 3.3 are typical of other analysis comparisons, where a layer-based approach tends to produce similar results to bead-based models.

Heat is rapidly input to the weld pass material, using internal volumetric heat generation, at a rate which raises the peak weld metal temperature to 3,000–3,500 °F and the base metal adjacent to the weld to about 2,000 °F. These are approximately the temperatures that the weld metal and surrounding base materials reach during welding [16]. Additionally, the penetration of temperatures above 1,000°F is limited by adjusting the heat input rate and time. Rapid heating of the weld material is necessary in order to reach the desired peak weld puddle temperatures without overheating the surrounding base metal. Conversely, if the heat is applied too rapidly, the surrounding base metal materials do not reach a high enough temperature for good fusion. As noted above, thermal properties for the materials are specified in the model for temperatures up to 3,500 °F; properties at elevated temperatures are estimated or extrapolated from those at lower temperatures.

Weld Repairs

Weld repairs were simulated by deactivating elements associated with previously welded material and reapplying new weld metal in its place. Deactivation of elements essentially results in elimination of the conductive capacity and stiffness of the deactivated element in heat transfer and structural analyses, respectively. Repair welds are also done in layers approximately 0.1 inches thick.

Hydrostatic Testing

Components were hydrostatically tested to approximately 3,110 psig after installation. This step was included in the analysis since applied hydrostatic pressure further yields any material stressed to near yield by welding and, therefore, results in a reduction of the peak residual tensile stresses after the hydrostatic test pressure is released. In this manner, the hydrostatic testing represents a form of stress improvement in areas of high stress. In addition to applying pressure to all wetted inside surfaces, an axial tensile stress is applied to the end of the pipe equal to the longitudinal pressure stress in the pipe wall.

Operating Conditions

Operating conditions are simulated by pressurizing the inside of the model to 2,235 psig and heating all of the material uniformly to the nominal 653°F operating temperature. The pressure and thermal conditions are added to the model which has already been subjected to welding (and weld repairs) and hydrostatic testing. Operating loads due to piping forces and moments are not considered in this analysis. The operating temperature is applied first as a separate load case, since this analysis result is the one that will be used to load the fracture mechanics models.

Case Specific Analysis Steps

Because of the different geometries and conditions being considered, each of the analysis models have case-specific analysis steps. While each were done using the general procedures outlined in Section 3.2.3 above, case-specific methods were used as follows:

Type 8 Surge Nozzle

The fabrication records for the Type 8 surge nozzle show that the dissimilar metal weld has the following aspects as part of its fabrication: 1) the initial weld is built radially outwards starting from the ID, 2) the initial weld land is ground until sound weld metal is reached, 3) the ground region is rewelded to the original inner diameter, 4) the weld is inspected and any repairs are made, and 5) a fill-in weld cladding layer is deposited to seat the thermal liner. Following these weld steps, the pressurizer is delivered and the stainless steel weld is made connecting the safe end to the plant piping. This sequence is depicted in Figure 3-7, which shows the model geometry at various points during this process. This figure also shows the repaired model condition prior to starting the repair.

Type 9 Surge Nozzle

The fabrication records for this surge nozzle type indicate that it was fabricated with a smaller than nominal inner diameter, material which was then machined to the finished ID. Therefore, no inside surface finishing pass was considered for this analysis case. For this analysis case, a butt weld similar to the Type 8 weld is performed, but the inside diameter is 0.25 inches smaller than the finished radius. After completion of the weld, the inner region is analytically removed as indicated, back to the finished inside radius.

Type 1a/2b Safety/Relief Nozzle

Similar to the Type 8 surge nozzle, the weld cases for this nozzle geometry were completed with an initial U-groove weld, followed by an ID grindout and back-weld, both with and without the stainless steel safe end to pipe weld. As noted in Section 2, a back-weld is a weld on the "back" side (in this case the ID side) of the weld joint. A pair of 0.75-inch deep repair cases were also considered; following the butt weld process, the repair region shown in Figure 3-1 was analytically removed and rewelded. As noted in Section 3.1.1, the repair process was analyzed using an axisymmetric (360°) model as well as a three-dimensional model where the repair occurs over 20° over the inside circumference. The Type 2b nozzle liner fillet weld was performed in two layers following the ID grindout and back-weld. Additionally, a case was considered where a single weld layer, 0.1 inches thick, was deposited at the ID of the safe end.

3.1.3 Analysis Results

In examining the results of the welding residual stress models, stresses in the axial direction are of particular interest since they are the driving force behind circumferential cracking. Therefore, in this section, axial stress contour plots and graphs comparing axial stress data are presented. The operating temperature welding residual stress condition is primarily used for reporting results. The through-wall stresses at this condition are most appropriate for application to the fracture mechanics model, since pressure and other external force loads are applied separately to the fracture mechanics model.

Stress Contour Plots

Figure 3-8 through Figure 3-13 present the axial stresses at operating temperature conditions for the various safety/relief nozzle geometry cases described in Section 3.1.1. Figure 3-8 and Figure 3-9 show results for the "standard" weld case (including back-weld), with and without the presence of the stainless steel safe end to pipe weld. Figure 3-10 shows the results from the safe end ID weld buildup case, and the liner fillet weld case is included in Figure 3-11. Finally, Figure 3-12 and Figure 3-13 show the stress results for the 0.75-inch deep ID repair; Figure 3-12 is for an axisymmetric (360°) version of the repair and Figure 3-13 shows the results for the 20° (total) extent repair three-dimensional model.

Figure 3-14 through Figure 3-17 present the axial stress results for the surge nozzle cases described in Section 3.1.2. Figure 3-14 and Figure 3-15 show results for the standard weld case (including back-weld and fill-in weld), with and without the presence of the safe end to pipe weld. Figure 3-16 shows the results for the 5/16-inch ID repair case. Figure 3-17 presents the results for the Type 9 surge nozzle, after the inner region has been analytically removed.

Through-Wall Stress Distributions

In addition to the stress contour plots, through-wall stress distributions were taken for the various analysis cases considered. Stress paths were used that considered the regions of elevated stress at the ID surface of the model, and that remained mostly perpendicular to the axial direction. The purpose of these distributions was to determine the through-wall stress profiles that would be applied to the fracture mechanics analysis models, described in Section 4. The sensitivity to stress path direction was considered by including results from less conservative analyses in the analysis matrix. The paths used for the stress distributions are shown on the stress contour plots described above. Unless otherwise noted, all stresses are axial stresses at operating temperature conditions.

Figure 3-18 is a plot comparing the various safety/relief nozzle analysis cases. This figure demonstrates that the safe end ID weld buildup and the liner fillet weld stress distributions are similar to the base analysis model (that includes the stainless steel weld). Therefore, it can be concluded that the impact of these conditions is negligible for the purposes of the overall analysis work. Figure 3-18 also demonstrates the impact of the stainless steel weld on the through-wall stress distribution location selected. Note that comparing Figure 3-8 (with SS weld) and Figure 3-10 (without SS weld) shows the axial stress contour patterns are similar; therefore, the path directions for these two cases are the same. The stainless steel weld imparts a

through-wall bending moment to the model, one that reduces the ID stress by about 10 to 15 ksi. Additionally, Figure 3-18 demonstrates that the 360° ID repair case with a deep repair imparts tensile stresses at the ID surface that are balanced by compressive stresses towards the OD; further analysis of this repair is included in Figure 3-19, discussed below. Finally, the stress results may also be compared to the through-wall stress distribution selected for previous analysis work considering through-wall circumferential crack growth, labeled "ASME Modified" [3]. This stress distribution is less compressive than the ones predicted by the welding residual stress analysis model. EMC^2 developed the "ASME Modified" WRS profile based on the "thick-wall" stress data from stress measurements performed on BWR piping weld mockups [42,43], scaled to account for the higher yield strength of Alloy 182 weld material.

Figure 3-19 is a plot that focuses on the 0.75-inch deep ID repair case considered for the safety/relief nozzle geometry. The repair geometry was considered both as a 360° repair and as a limited extent (and more realistic) 20° ID arc length repair. The stress distributions shown in Figure 3-19 are at a series of circumferential positions around the nozzle. Because the model is a 180° symmetric model, the center of the repair zone is at 0°, and the edge of the repair zone is at 10°. Also shown in this figure are the results for the axisymmetric unrepaired case and the axisymmetric 0.75-inch ID repair case. This figure shows that, for a limited circumferential extent repair, the center of the repair differs substantially from the 360° version of the same repair geometry. The figure also shows that the effect of the repair on through-wall axial stresses extends for approximately 20° beyond the edge of the repair, after which the through-wall stress distributions become: 1) similar to one another and 2) similar to the unrepaired axisymmetric model results.

Figure 3-20 presents the results from the surge nozzle analysis cases. This figure demonstrates that the safe end to pipe weld has a similar through-wall bending effect as seen in the safety/relief analysis cases. The analysis results may also be compared to the welding residual stress distribution used in previous fracture mechanics analyses for the surge nozzle case [3]; it is noted that the distribution used in [3] was taken from the analysis of a nozzle geometry that does not have a fill-in weld. The axisymmetric repair analysis results show a more tensile ID region balanced by a more compressive OD section; limited extent repairs were not analyzed for the surge nozzle geometry. Figure 3-20 also demonstrates that the Type 9 surge nozzle geometry, as analyzed, has compressive stresses on the ID surface.

3.2 WRS Literature Data

In addition to the new work on welding residual stress simulation performed in support of this project, a review of existing literature on welding residual stress was conducted. A number of papers were identified that described analysis results and residual stress measurements for axial stresses in piping butt welds, particularly in the presence of partial arc extent repairs. The papers identified the following characteristics for butt weld axial stresses:

- Repair regions tend to cause more compressive axial stresses in the approximately 20° of material beyond the edge of the repair zone [17]
- Repair regions may have significantly higher axial through-wall stresses since the repair through-wall section is balanced by the remainder of the pipe cross section [18]

As demonstrated by the results in Figure 3-13 and Figure 3-19, the welding residual stress results for the safety/relief nozzle with a partial arc repair region are in agreement with these characteristics.

3.3 Validation and Benchmarking

The finite element analysis methodologies described in this section were also used to simulate the fabrication of a mockup where residual stresses were measured and compared to analyzed residual stresses. Comparisons were performed using geometry and results from a research project completed by the European Commission Joint Research Centre's (JRC) Institute for Energy [19]. The project investigated a wide range of issues related to the structural integrity assessment of a stainless steel weld joining stainless steel and low alloy steel components.

One of the task groups implemented by the JRC research project focused on the reliability of finite element analyses to predict residual stress in the welded joint. This task group organized a series of round-robin exercises that compared predicted welding residual stress distributions to those measured for a welded joint mockup. Complete details of the mockup geometry and welding process were made available to all participants in the round-robin, and their welding residual stress analysis results were compared to each other and to through-wall stresses measured by neutron diffraction (ND).

A drawing of the welded joint mockup as described in the round robin task group problem definition [20] is shown in Figure 3-21. This figure depicts the finished weld preparation geometry, following deposition and machining of the stainless steel butter layer on the A508 spool piece. As shown in Figure 3-21, the mockup comprised two piping spool pieces, each approximately 500 mm (20 inches) long, one made of 316L stainless steel and one from A508 low alloy steel. The weld preparation for the mockup was a V-bevel type, with the 316L piping spool forming a backing strip for the initial weld layers. The initial A508 spool piece was 64 mm (2.5 inches) thick, and the initial 316L spool piece was 73 mm (2.9 inches) thick. According to Figure 5 of [20], the dissimilar metal weld was performed in 96 total passes, comprising roughly 18 layers. Following completion of the weld, the assembly was heat treated at about 600°C (1,100°F); then the assembly was machined to the final dimensions depicted in Figure 3-21.

As noted above, the finite element analysis methodologies described in Section 3.1 were used to analyze the mockup geometry prepared for the JRC report. While the round robin problem definition provided extensive material property characterization data for the base and weld materials used for the mockup, the materials as defined in Section 3.1 were used for the comparison analysis. Additionally, since the models described in Section 3.1 did not simulate the butter weld deposition, the mockup simulation model likewise did not simulate the butter welding and machining process. Rather, the model started in a stress free condition from the machined weld preparation state depicted in Figure 3-21. While the specific bead sequence and weld process was provided for the round robin participants, the analysis model used 18 layers spanning the width of the weld groove. The geometry and the boundary conditions of the analysis model were specified to match the mockup conditions. In particular, the mockup was welded on rollers with no axial constraint; this boundary condition was preserved in the analysis model. The post weld heat treatment process was simulated using a uniform application of the

1,100°F temperature in a single structural load step, then removing the temperature in a single structural load step. Simulation of the ramp heating and cooling process was not performed, and creep relaxation properties for the materials were not included.

The final machining welding residual stresses for the analysis mockup are presented as contour plots in Figure 3-22 and Figure 3-23 for the axial and hoop directions, respectively. In addition to these contour plots, section lines were taken as appropriate to compare with data presented in the JRC report [19]. Figure 3-24 through Figure 3-27 are reproductions of Figure 6.10 through 6.13 in the JRC report, with data from the DEI analysis model also included. Figure 3-24 and Figure 3-25 examine the hoop and axial stresses along an axial cut line starting in the 316L material, running through the weld and butter, and into the A508 material, all located at 4.25 mm below the OD surface.

The DEI model is seen to compare very well for hoop stresses, and somewhat high for axial stresses along this cut line. The JRC report notes when describing these figures that the measured hoop stresses using neutron diffraction are considered more reliable and complete than the axial or radial results, and that the equivalent of Figure 3-24 is particularly important for verifying the finite element analysis results. Figure 3-26 and Figure 3-27 examine hoop and axial stresses along a through-wall cut line at the center of the butter. Despite not simulating the butter weld deposition process, the DEI model axial stress results compare well with the other finite element models from the JRC round robin, all of which did simulate the butter weld process. The hoop stress results compare less favorably, which is not unexpected given the difference in the modeling performed. This difference does not impact the axial stress results considered for circumferential flaws. The JRC report places particular emphasis, for model validation purposes, on the transition from tension to compression in the hoop direction from the weld to the A508 material in Figure 3-24; it is noted that the DEI model also captures this trend.

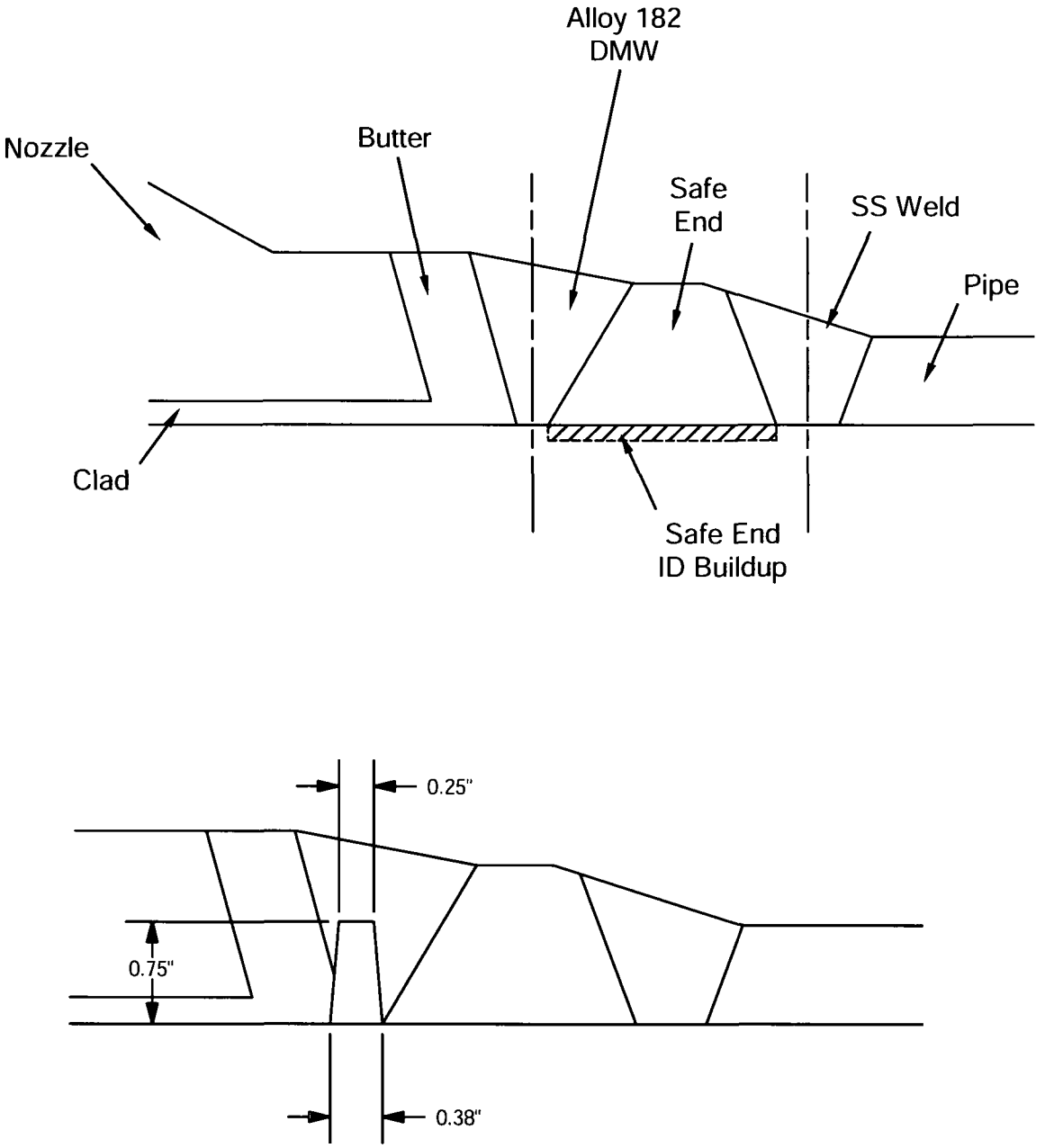

Figure 3-1
Type 1a Safety/Relief Nozzle Model Geometry

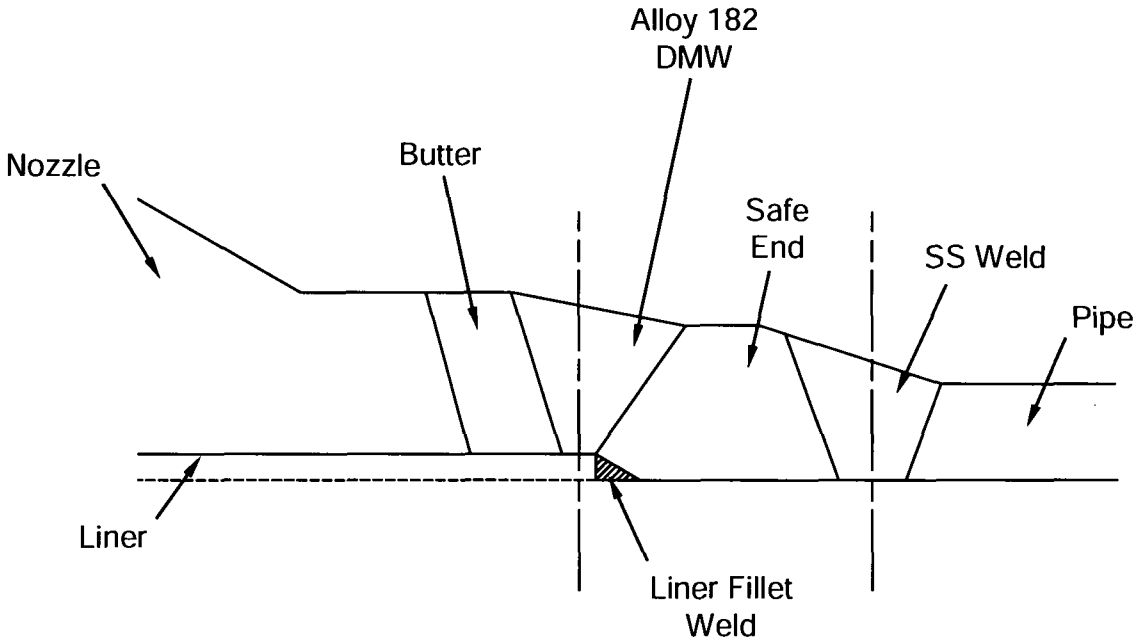

Figure 3-2
Type 2b Safety/Relief Nozzle Model Geometry

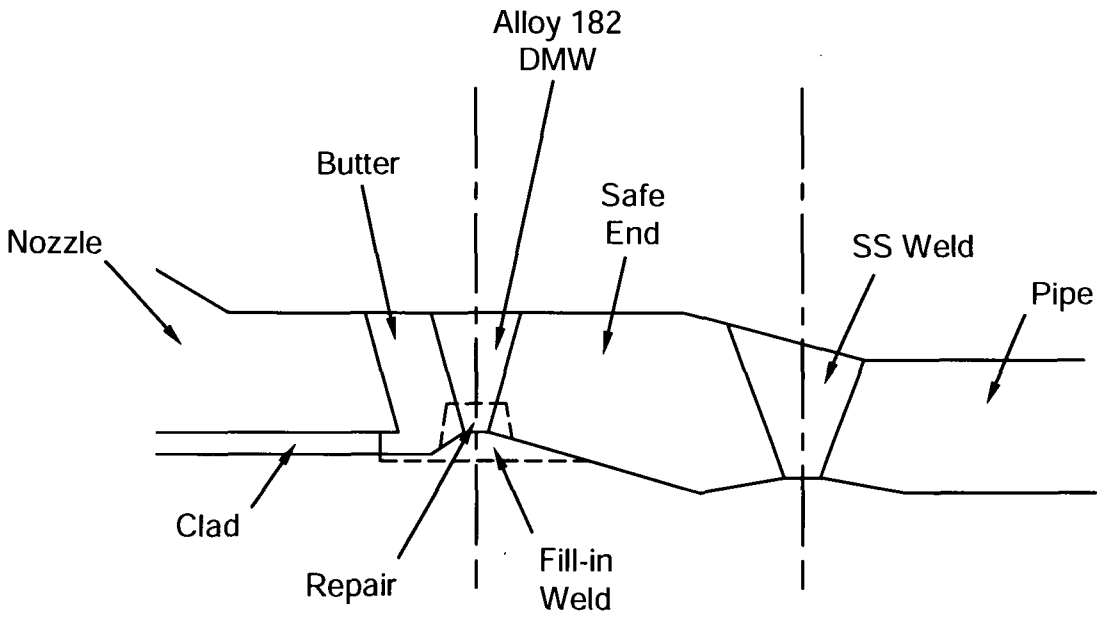

Figure 3-3
Type 8 Surge Nozzle Model Geometry

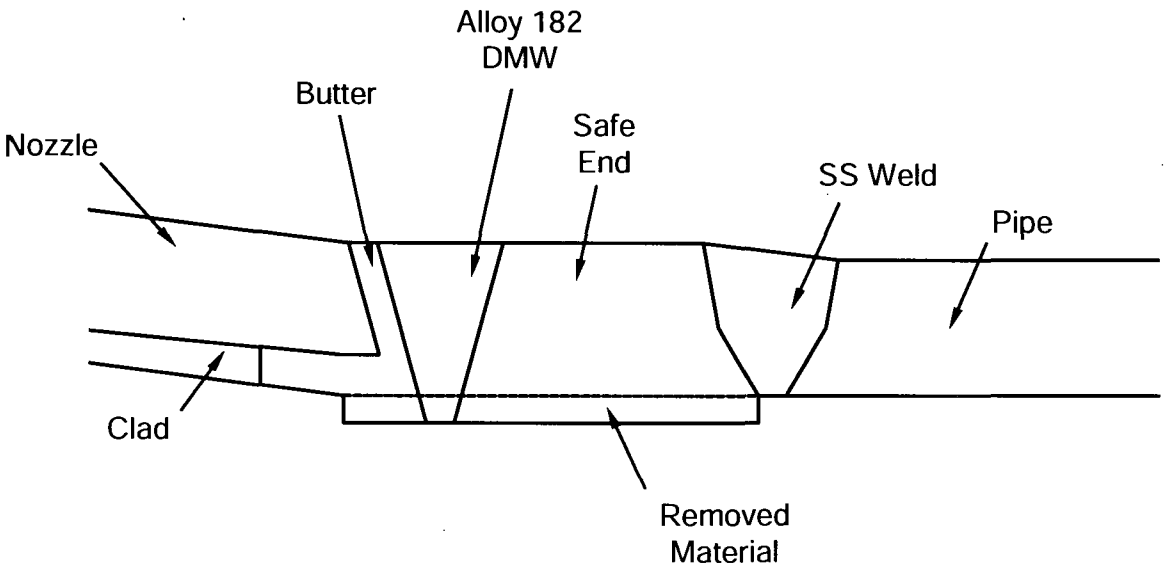

Figure 3-4
Type 9 Surge Nozzle Model Geometry

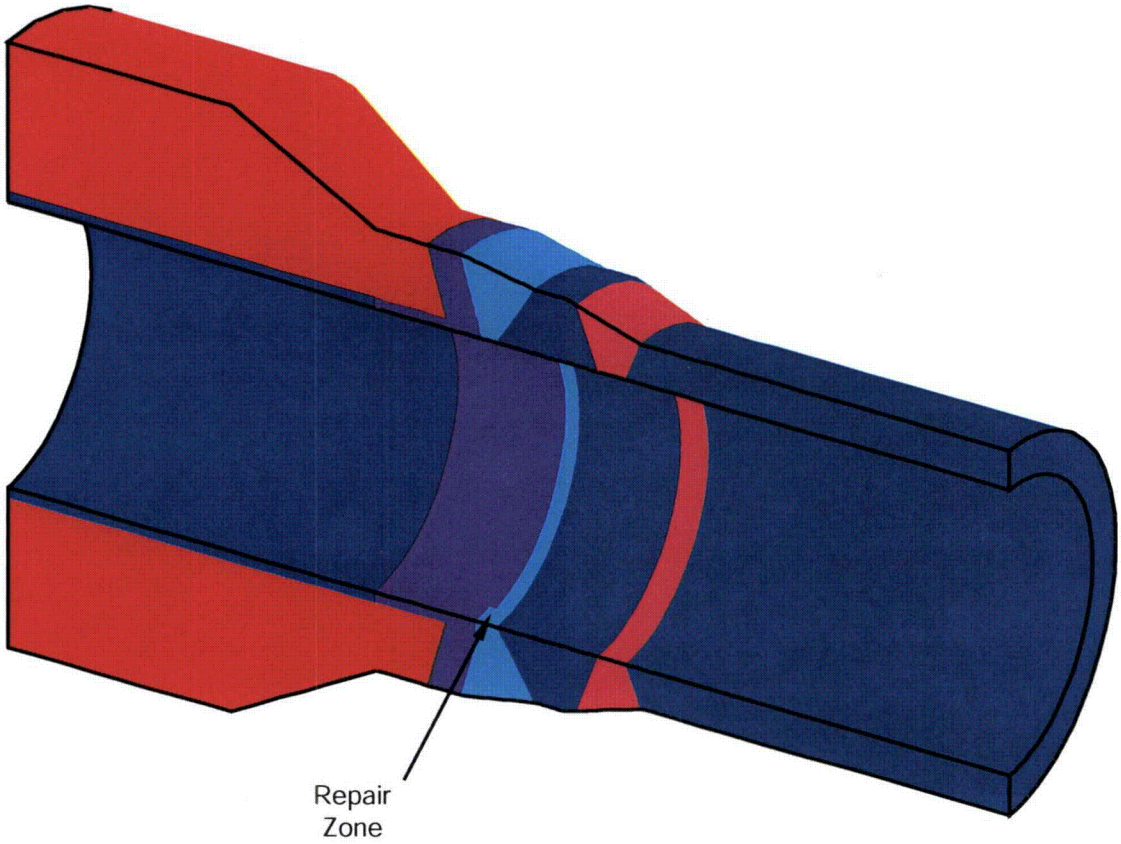

Figure 3-5
Safety/Relief Nozzle Repair Model Geometry

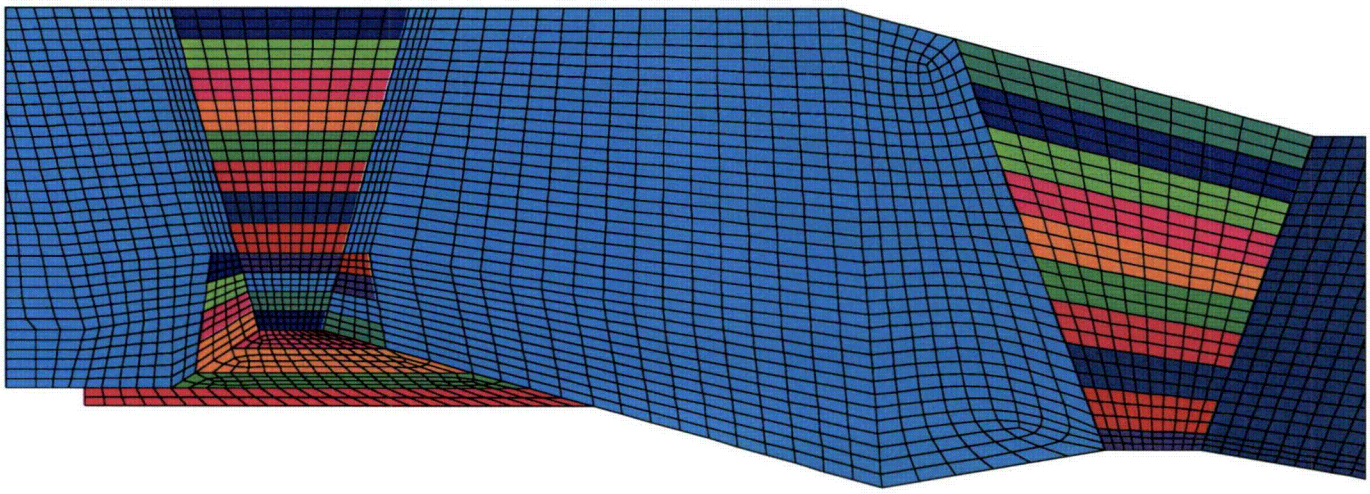

Figure 3-6
Type 8 Surge Nozzle Model – Element Mesh and Weld Layers

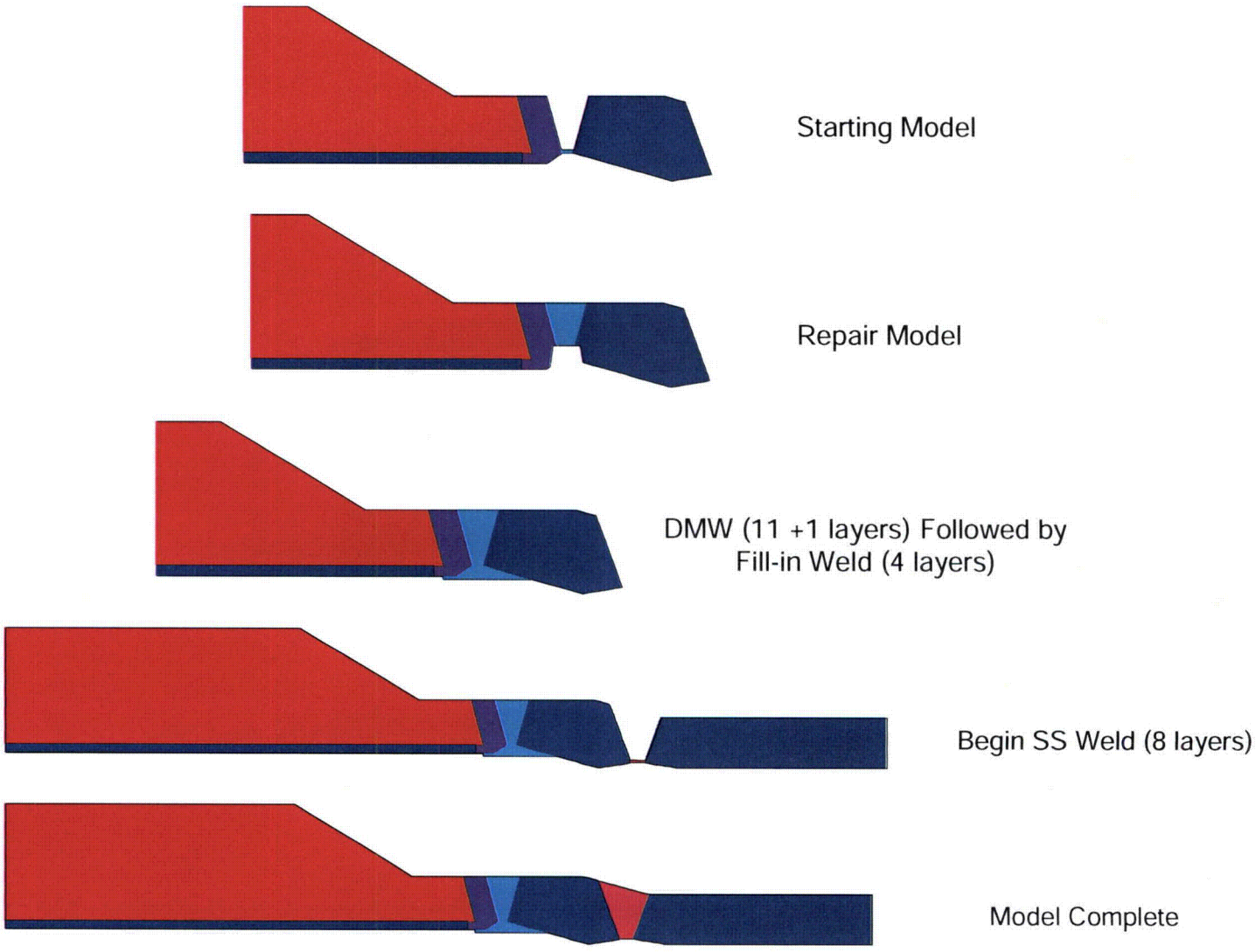

Figure 3-7
Type 8 Surge Nozzle Analysis Progression

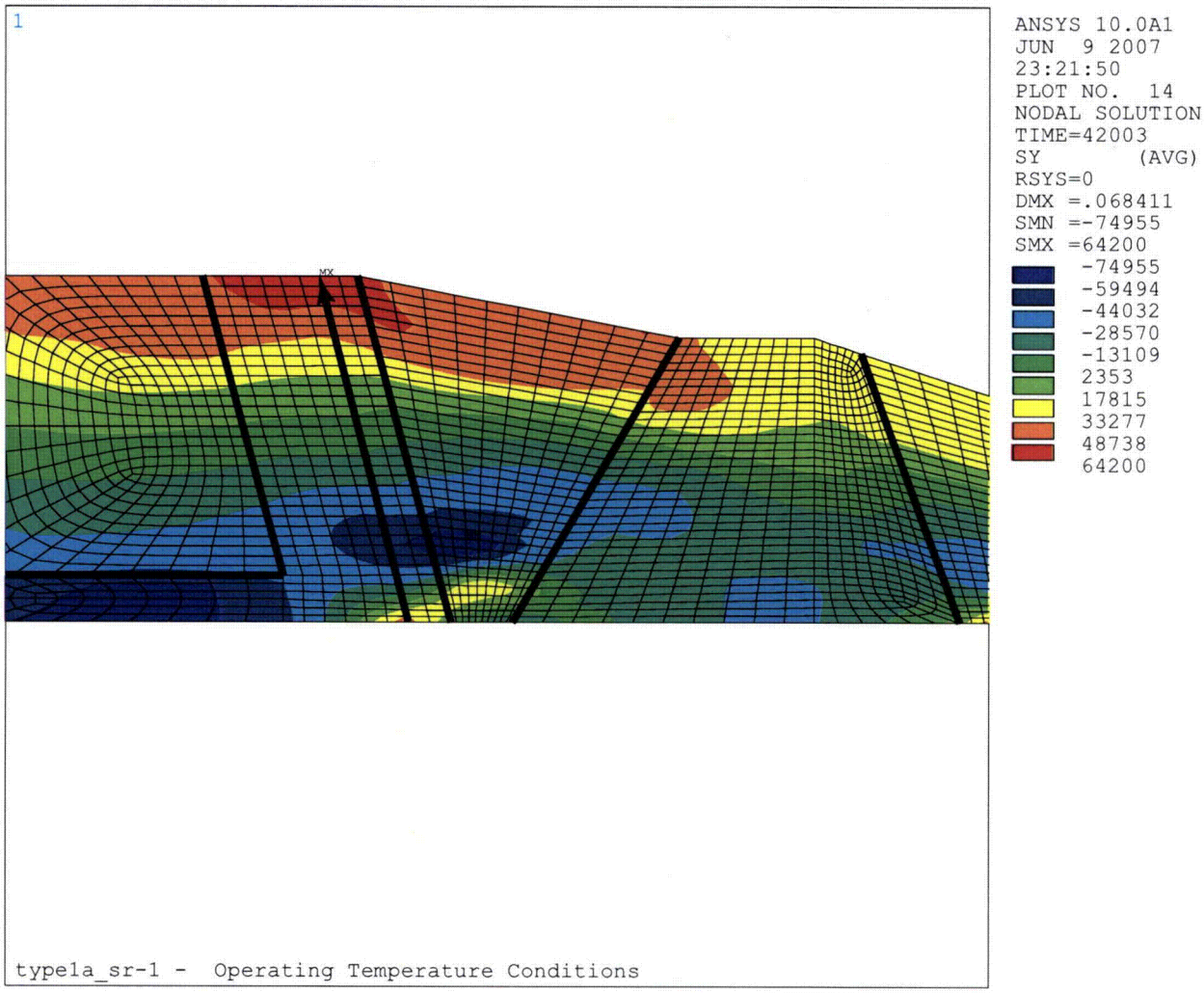

Figure 3-8
Axial Stress at Normal Operating Temperature for Safety/Relief Nozzle (DMW + back-weld + SS weld)

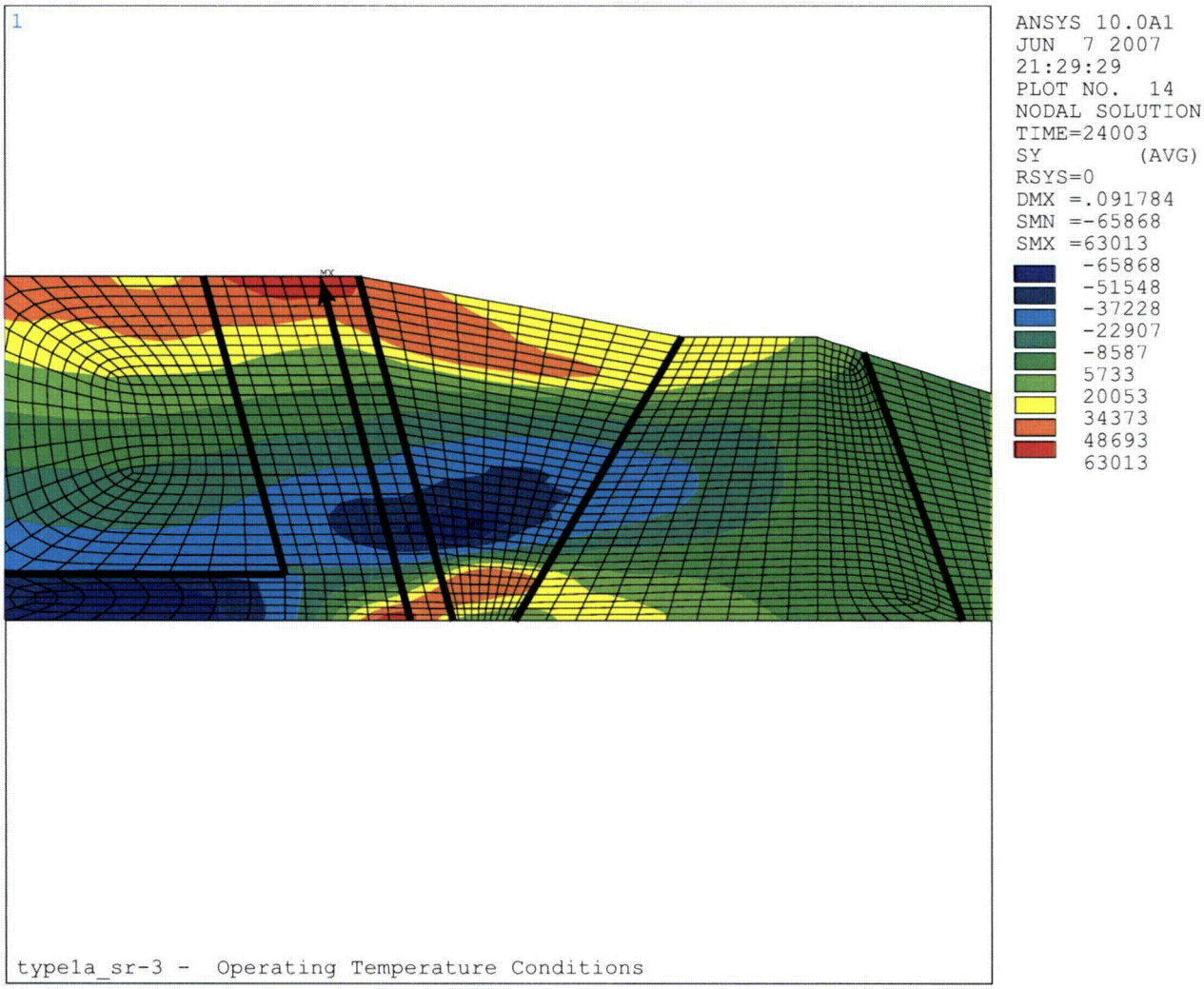

Figure 3-9
Axial Stress at Normal Operating Temperature for Safety/Relief Nozzle (DMW + back-weld, no SS weld)

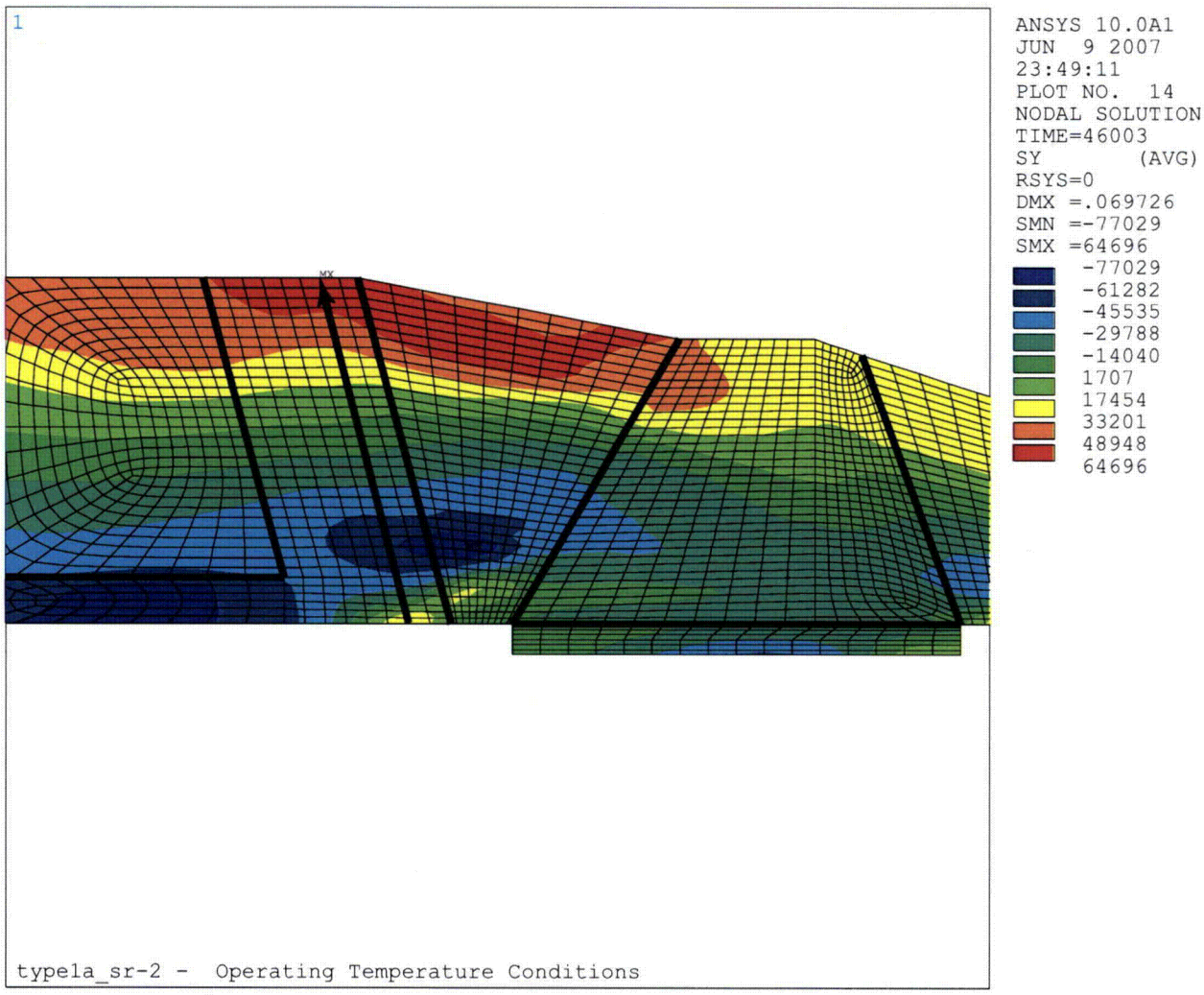

Figure 3-10
Axial Stress at Normal Operating Temperature for Safety/Relief Nozzle (DMW + back-weld + safe end ID weld + SS weld)

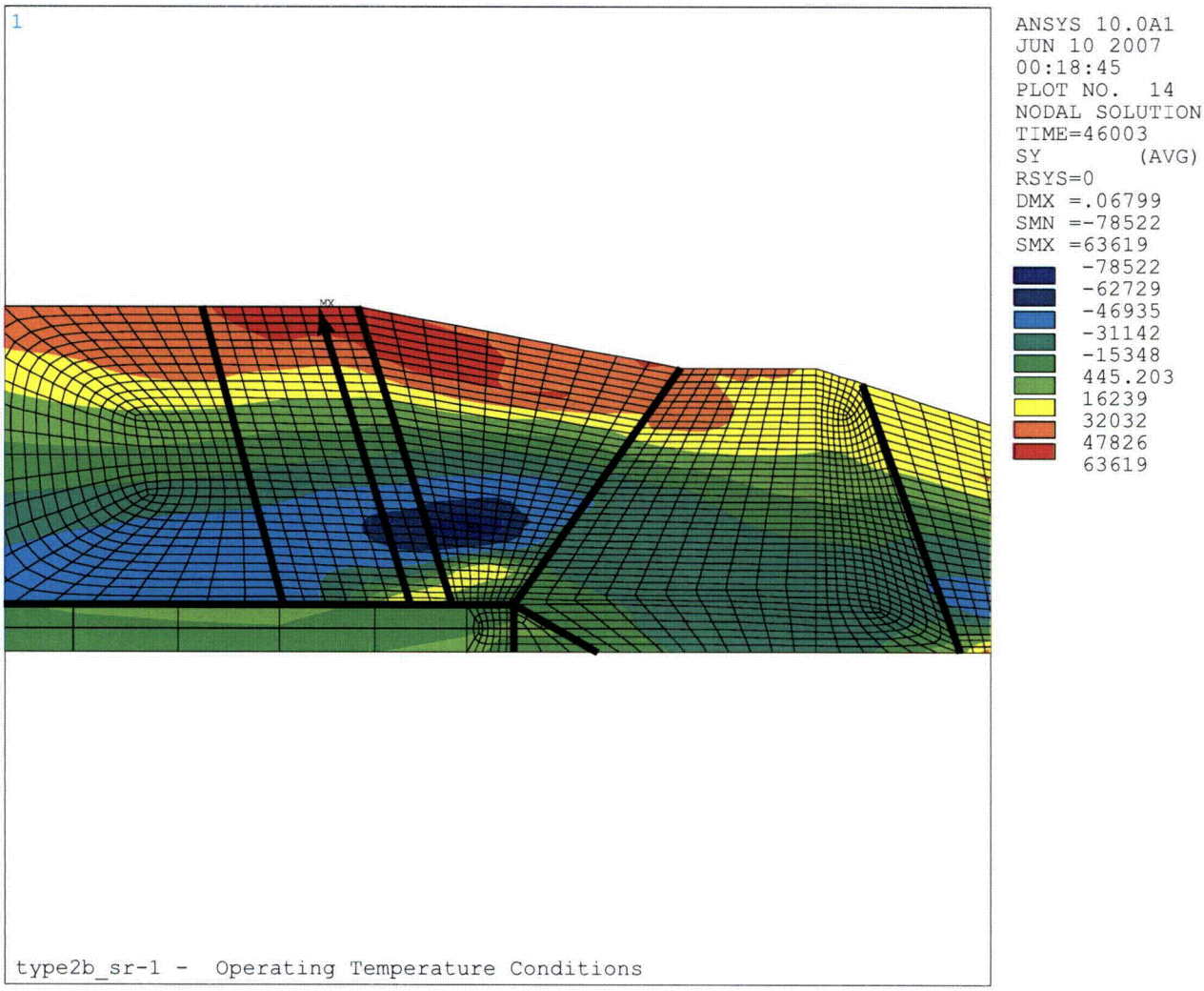

Figure 3-11
Axial Stress at Normal Operating Temperature for Safety/Relief Nozzle (DMW + back-weld + liner fillet weld + SS weld)

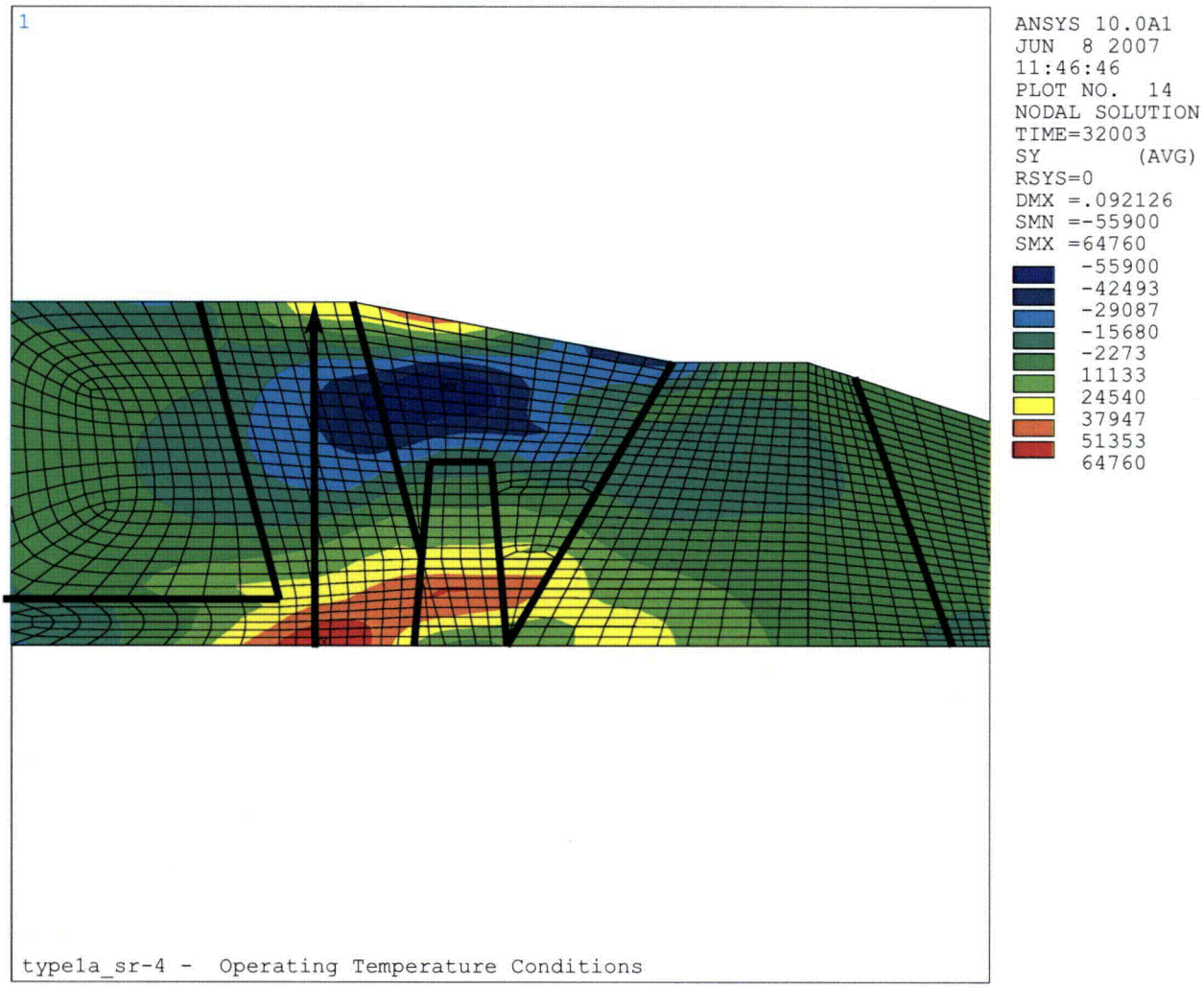

Figure 3-12
Axial Stress at Normal Operating Temperature for Safety/Relief Nozzle (DMW + back-weld + 360° ID repair, no SS weld)

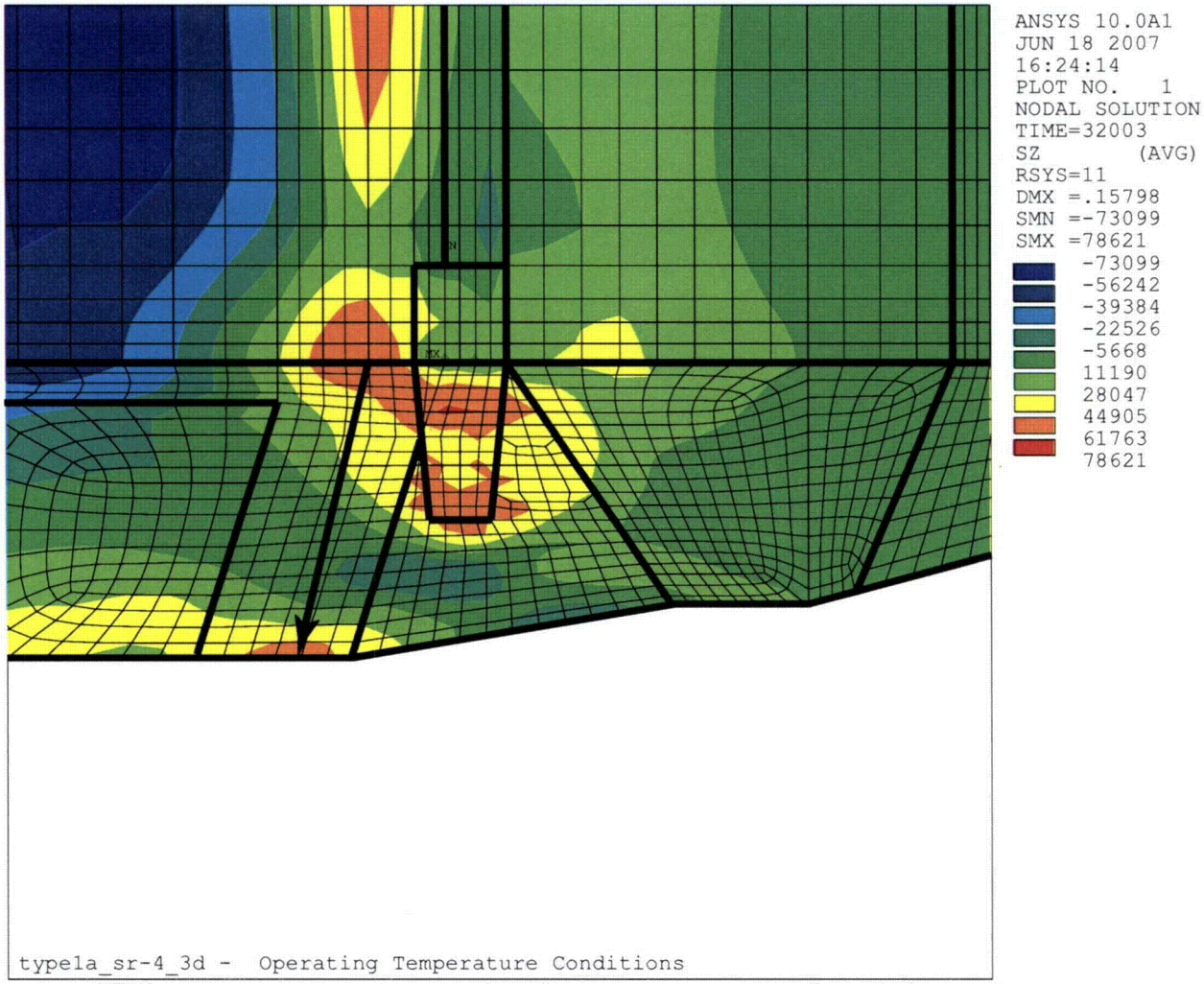

Figure 3-13
Axial Stress at Normal Operating Temperature for Safety/Relief Nozzle (DMW + back-weld + 20° ID repair, no SS weld)

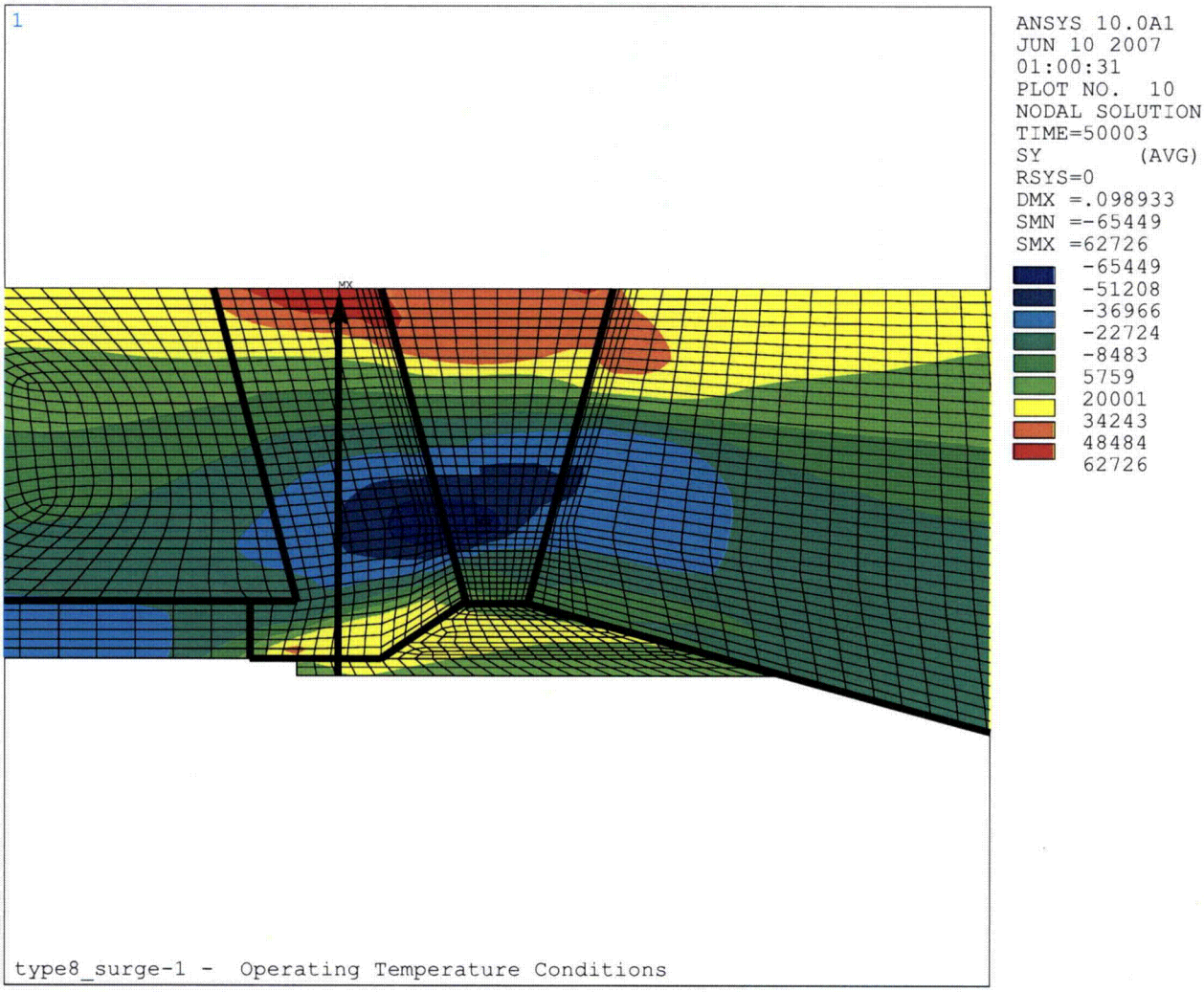

Figure 3-14
Axial Stress at Normal Operating Temperature for Type 8 Surge Nozzle (DMW + back-weld + fill-in weld + SS weld)

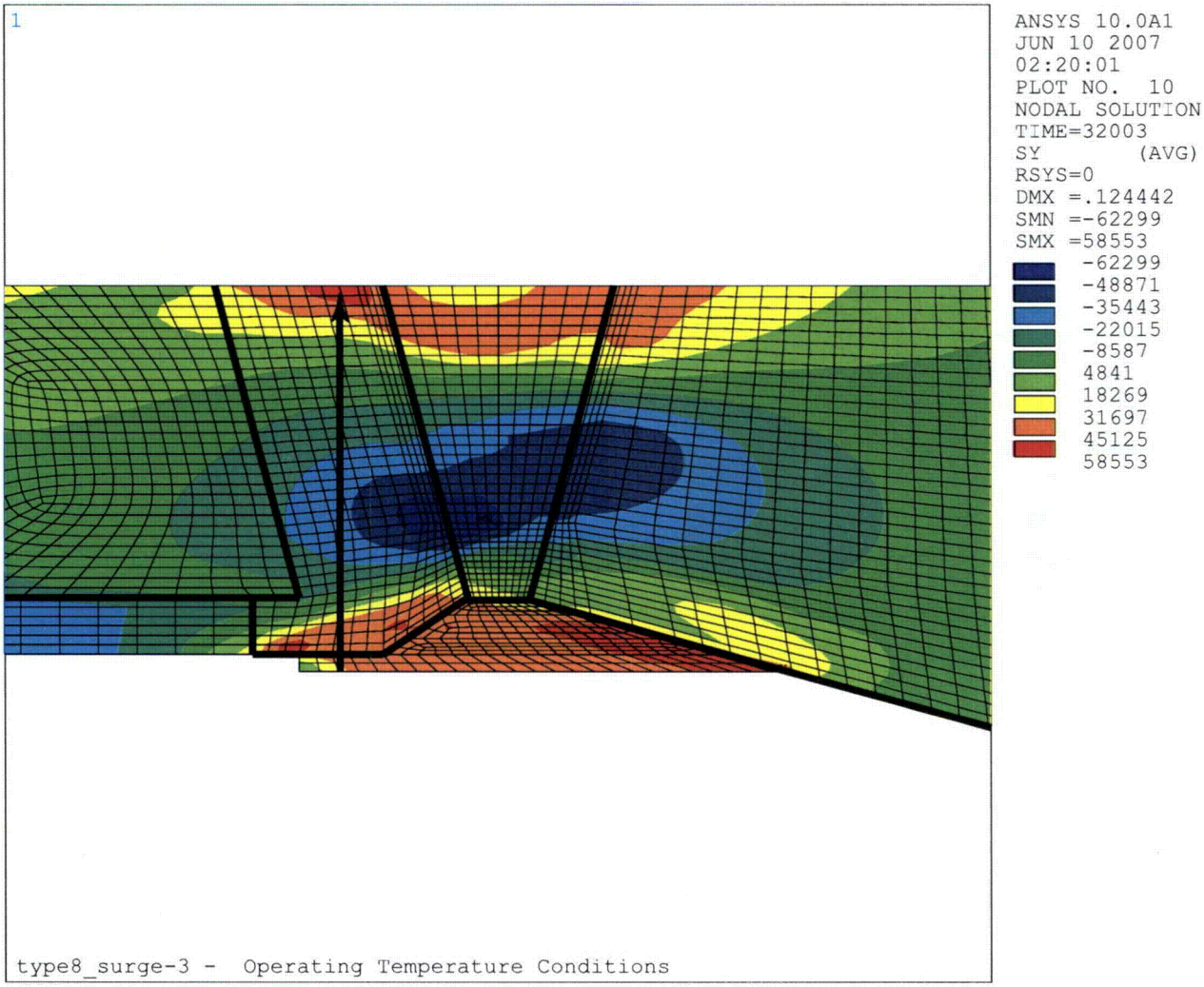

Figure 3-15
Axial Stress at Normal Operating Temperature for Type 8 Surge Nozzle (DMW + back-weld + fill-in weld, no SS weld)

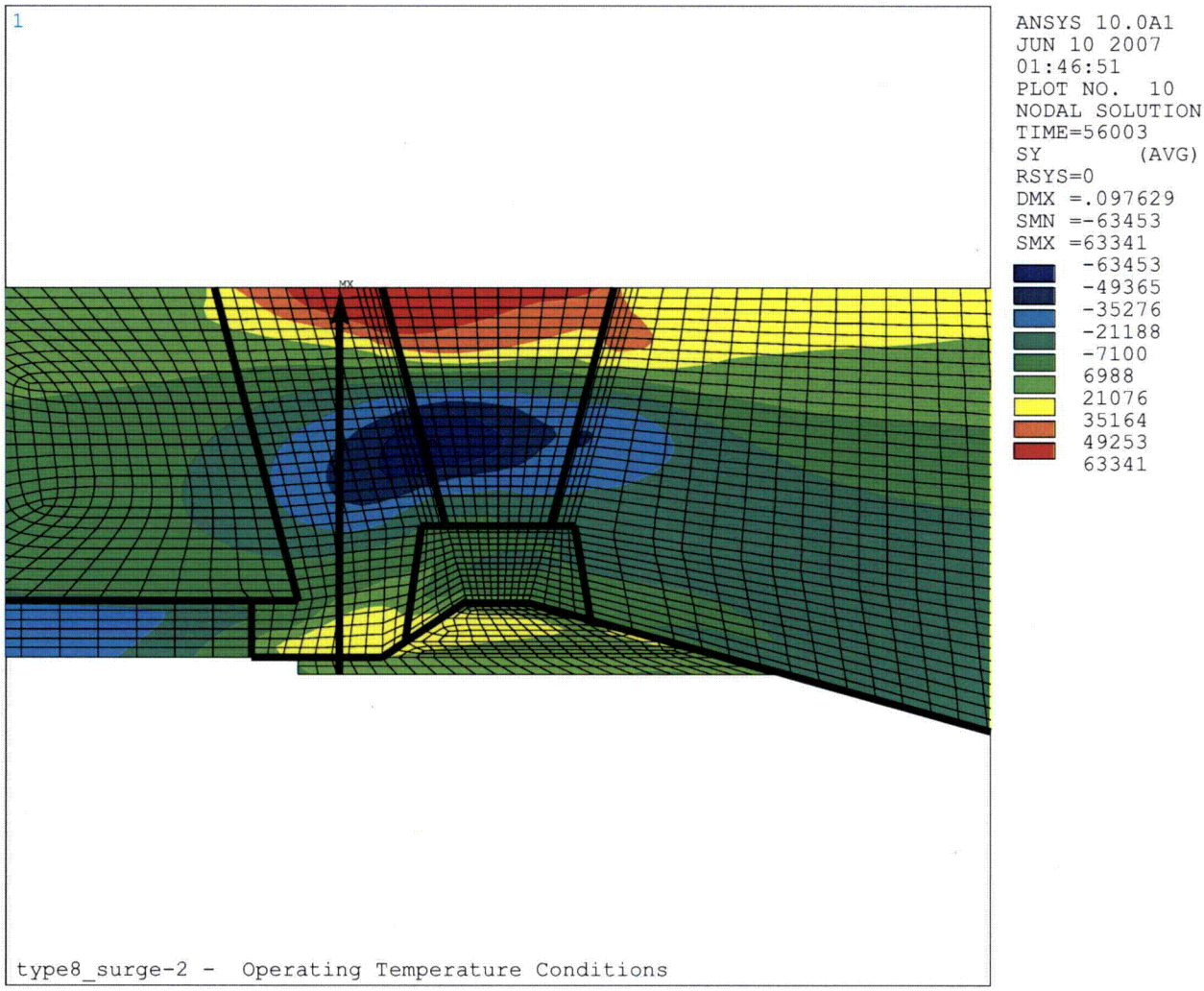

Figure 3-16
Axial Stress at Normal Operating Temperature for Type 8 Surge Nozzle (DMW + ID repair + fill-in weld + SS weld)

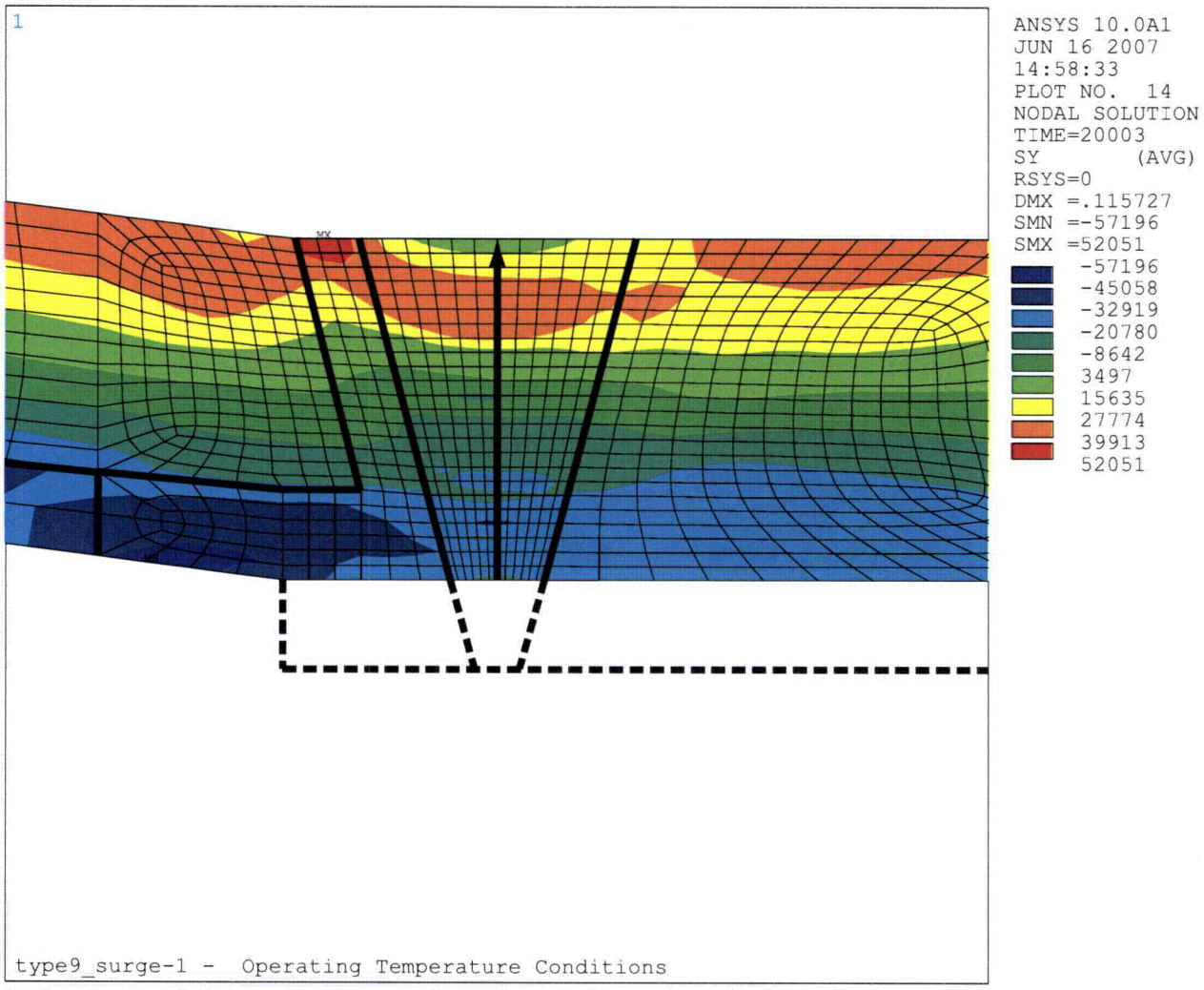

Figure 3-17
Axial Stress at Normal Operating Temperature for Type 9 Surge Nozzle (DMW + final machining, no SS weld)

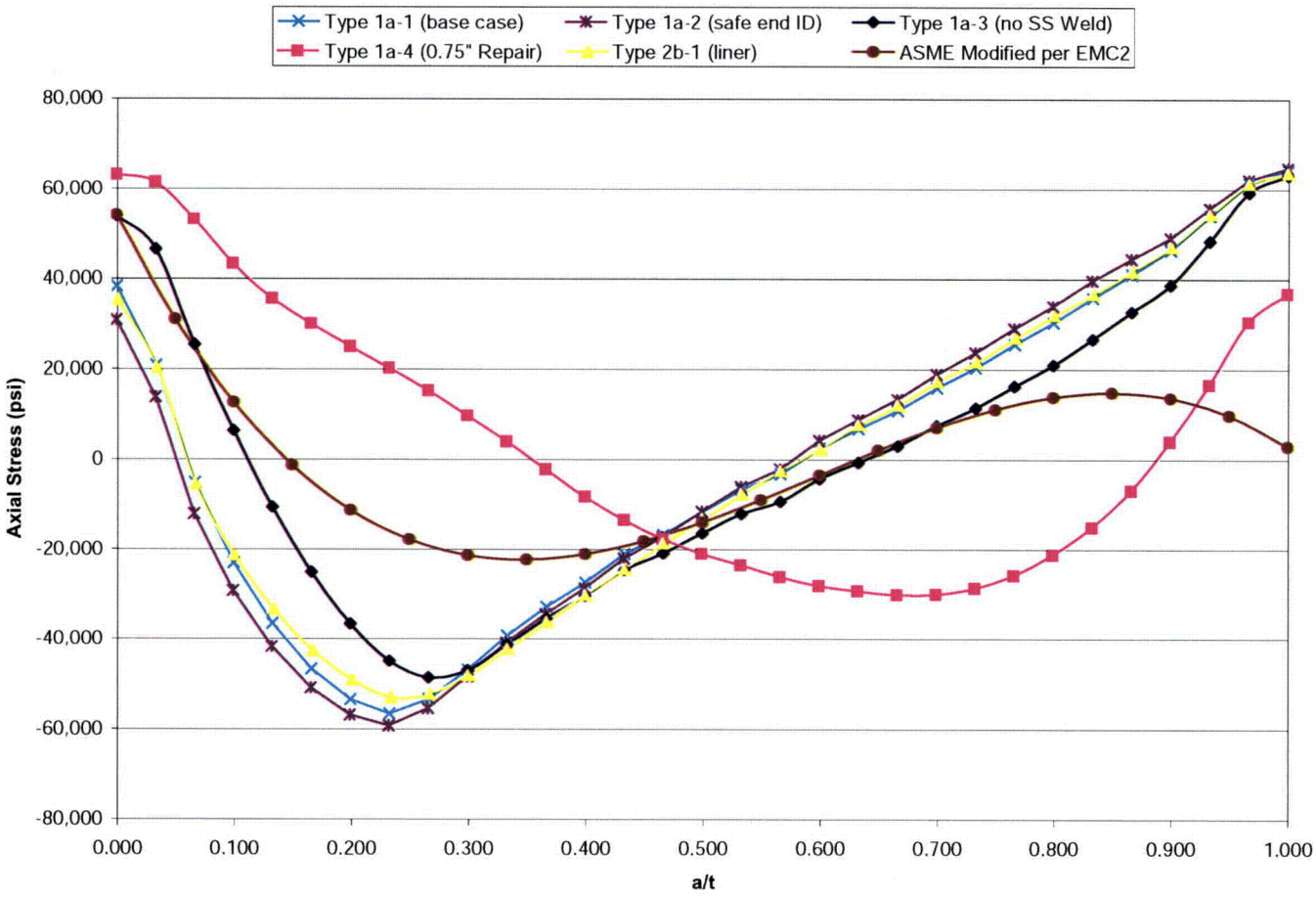

Legend:
Type 1a-1 (base case) = DMW + back-weld + SS Weld, see Figure 3-8
Type 1a-2 (safe end ID) = DMW + back-weld + safe end ID weld + SS weld, see Figure 3-10
Type 1a-3 (no SS Weld) = DMW + back-weld, no SS Weld, see Figure 3-9
Type 1a-4 (0.75″ repair) = DMW + back-weld + 360° ID repair, no SS Weld, see Figure 3-12
Type 2b-1 (liner) = DMW + back-weld + liner fillet weld + SS weld, see Figure 3-11
ASME Modified per EMC2 = Reference curve from [3]

Figure 3-18
Axial Stress Comparison – Safety/Relief Nozzle Analysis Cases

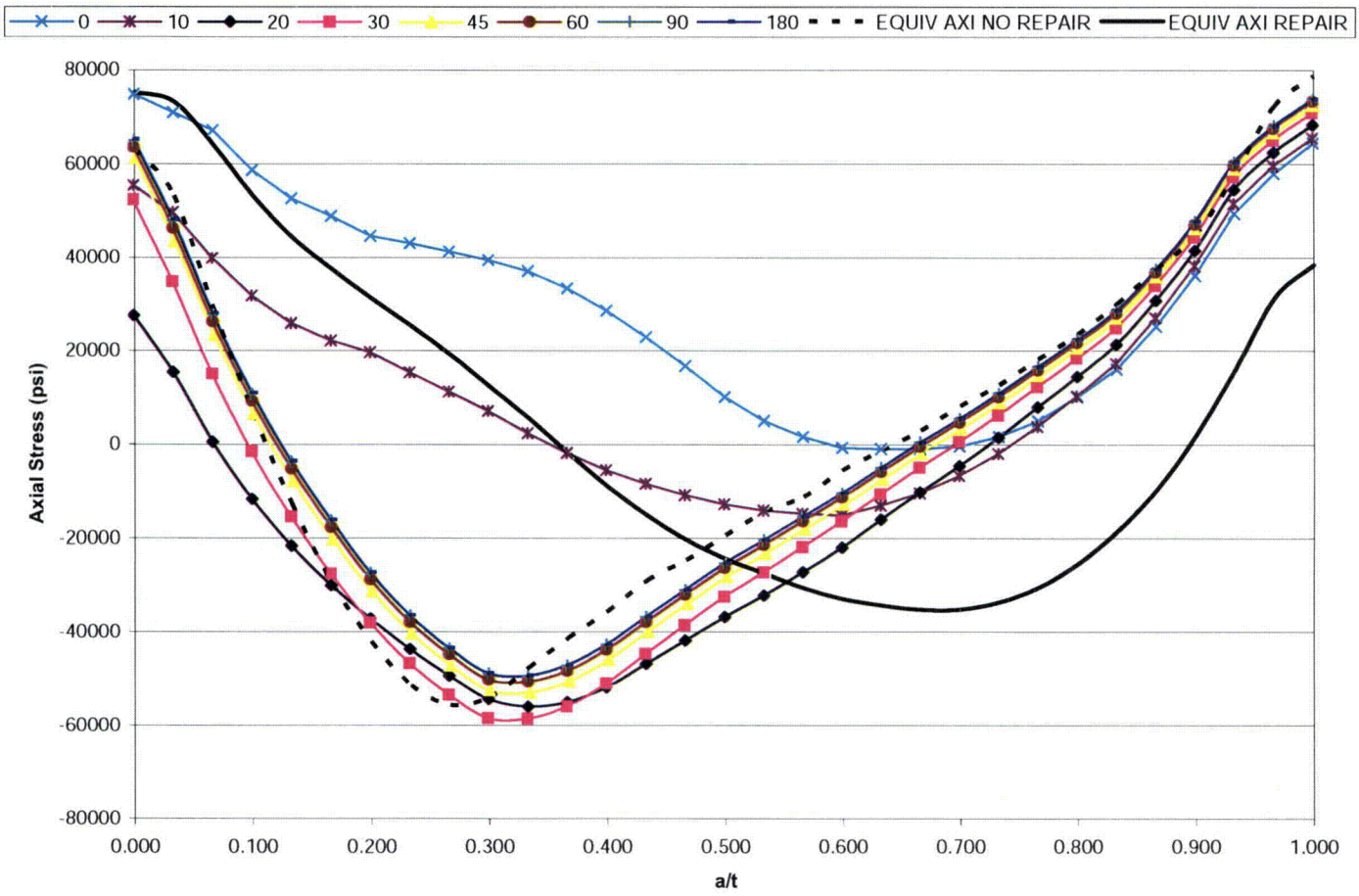

Legend:
0 = Center of 3D repair model, see Figure 3-13
10 = Circumferential edge of repair region, see Figure 3-13
20 – 180 = Arc length from center of repair, see Figure 3-13
EQUIV AXI NO REPAIR = Axisymmetric model with no repair, see Figure 3-9
EQUIV AXI REPAIR = Axisymmetric model with ID repair, see Figure 3-12

Figure 3-19
Axial Stress Comparison – Safety/Relief Partial Arc ID Repair Case

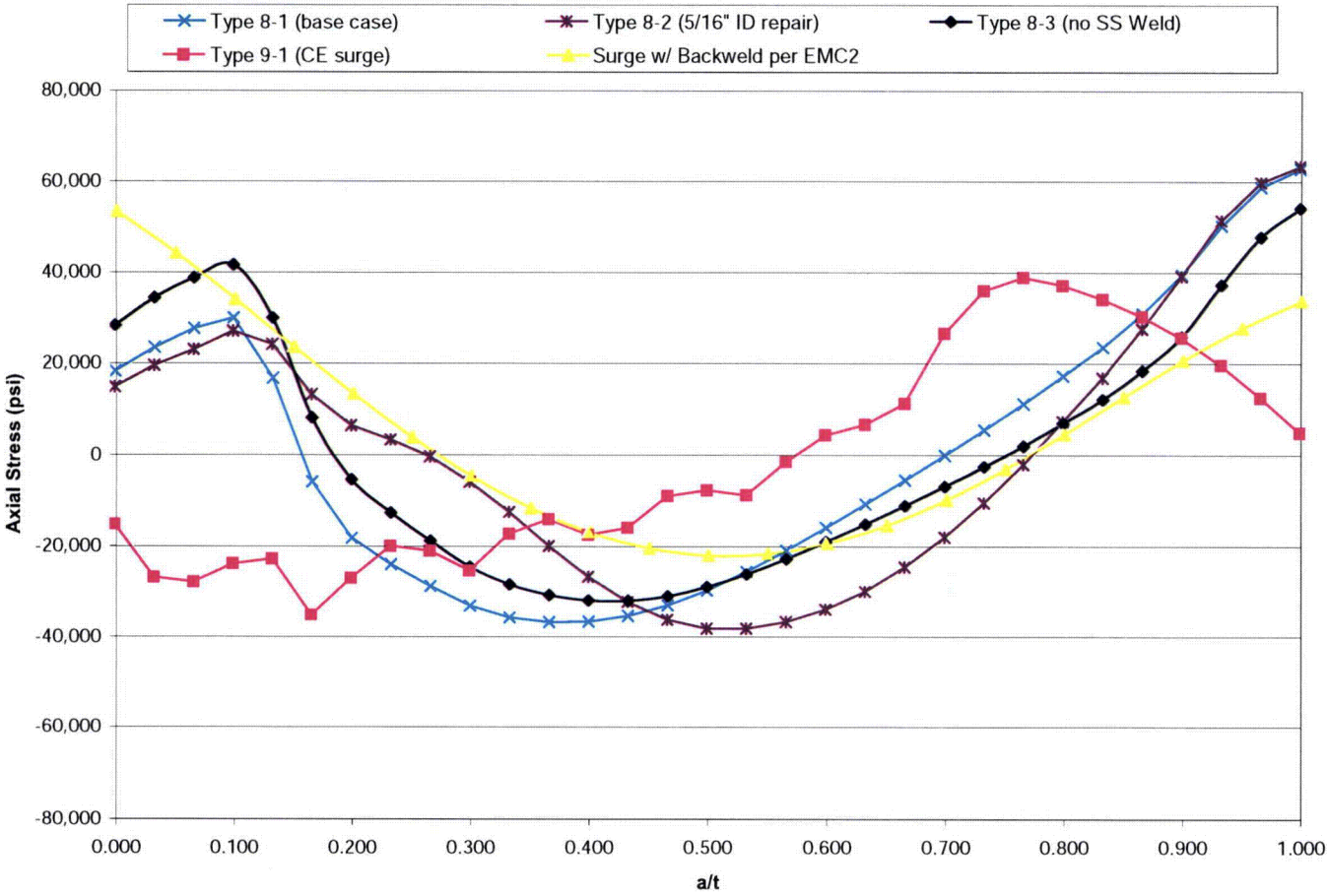

Legend:
Type 8-1 (base case) = DMW + back-weld + fill-in weld + SS weld, see Figure 3-14
Type 8-2 (5/16″ ID repair) = DMW + ID repair + fill-in weld + SS weld, see Figure 3-16
Type 8-3 (no SS weld) = DMW + back-weld + fill-in weld, no SS weld, see Figure 3-15
Type 9-1 (CE surge) = DMW + final machining, no SS weld, see Figure 3-17
Surge w/ Back-weld per EMC2 = Reference curve from [3]

Figure 3-20
Axial Stress Comparison – Surge Nozzle Analysis Cases

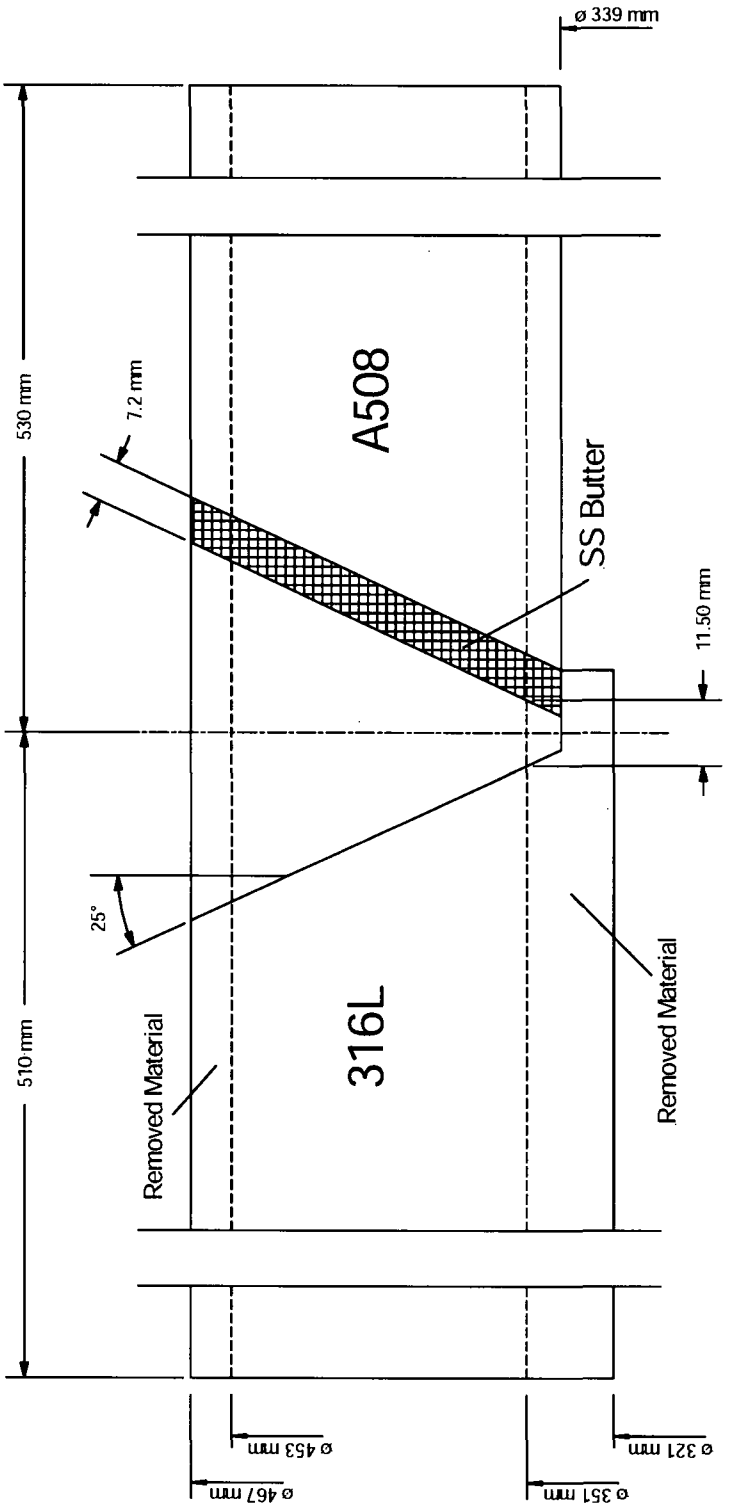

Figure 3-21
Welding Residual Stress Validation Mockup Drawing [20]

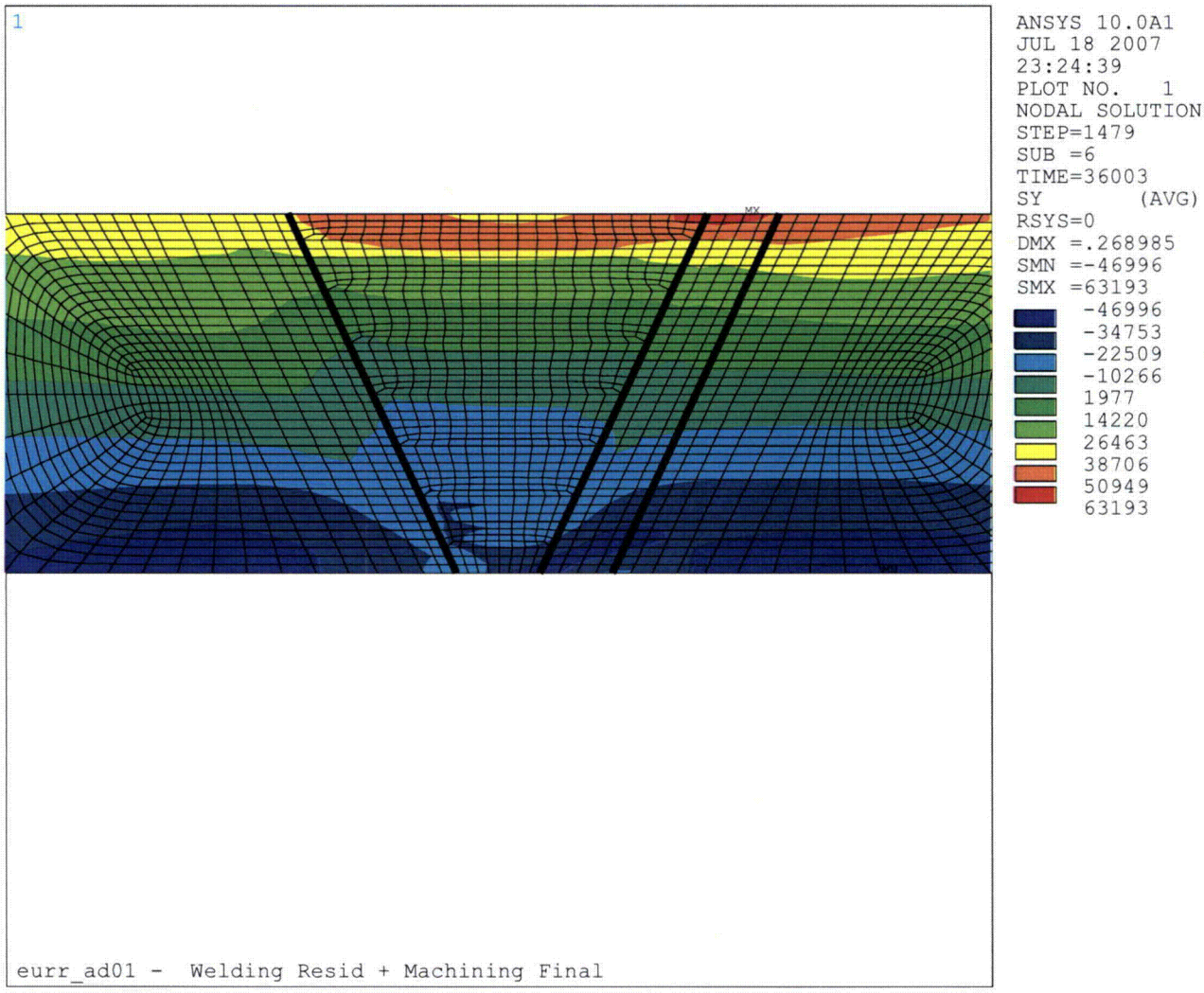

Figure 3-22
Validation Model Axial Stress Results – Final Machining

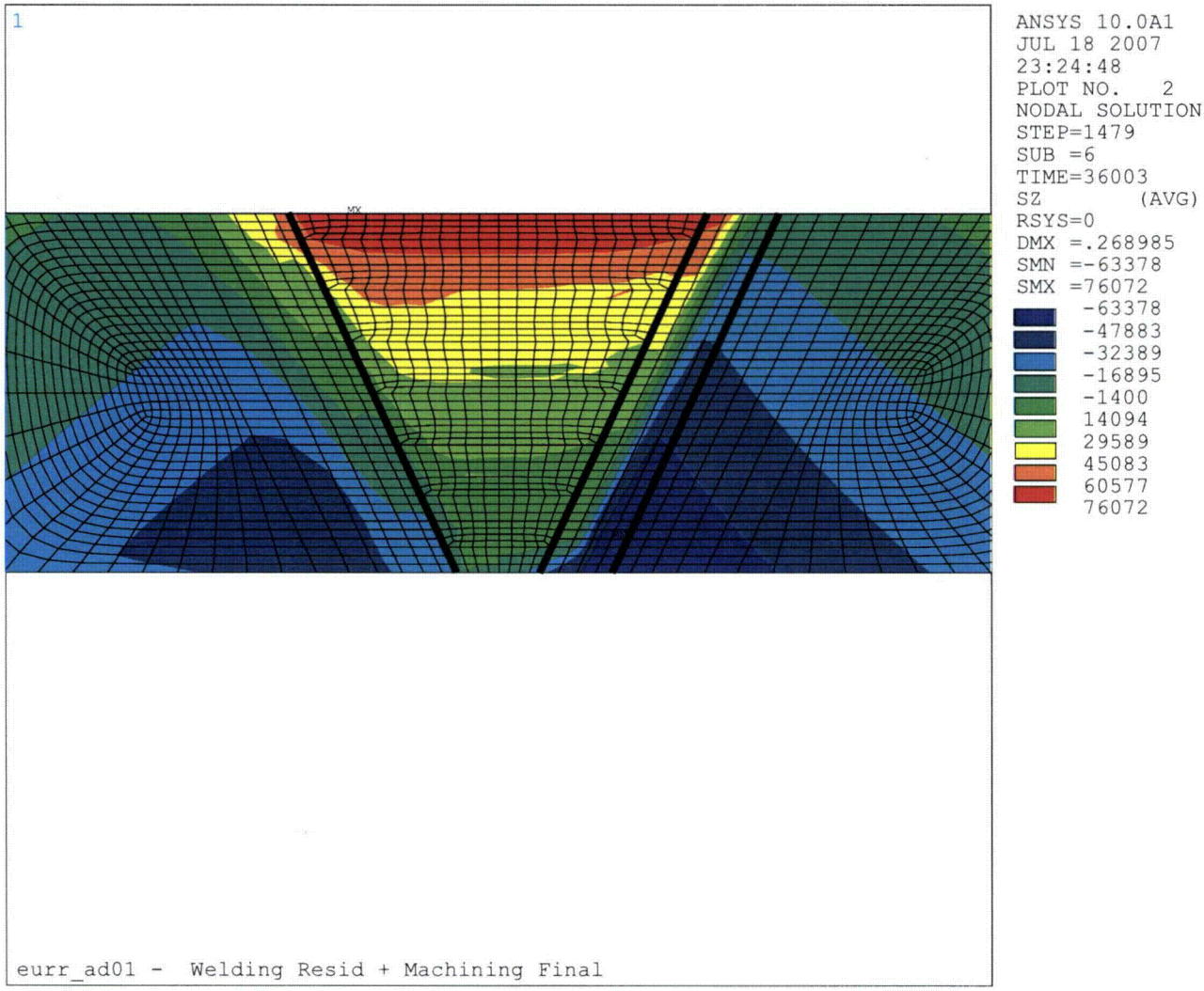

Figure 3-23
Validation Model Hoop Stress Results – Final Machining

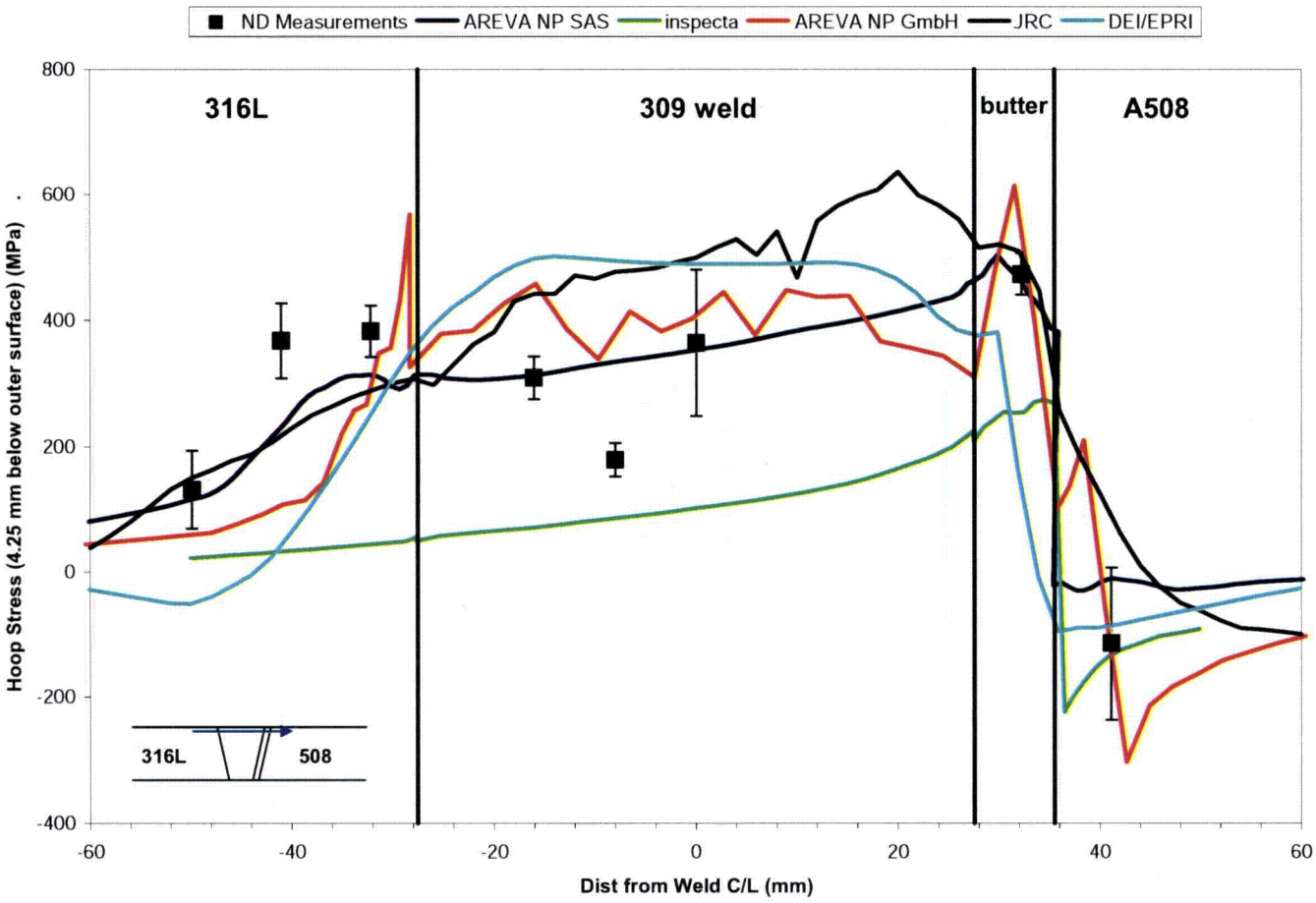

Figure 3-24
Validation Model Predicted vs. Measured Results, Hoop Direction, 4.25 mm Below the Outer Surface

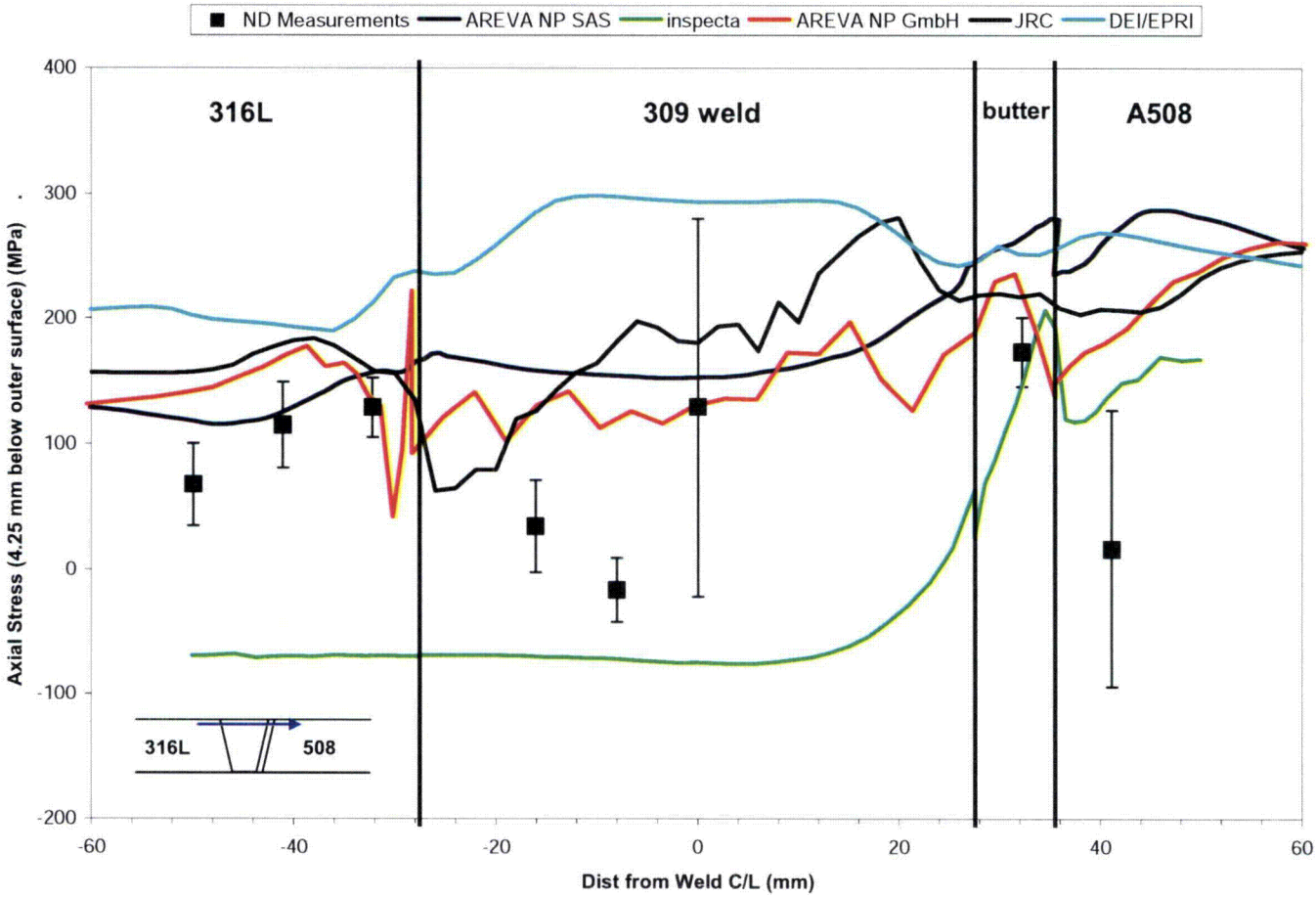

Figure 3-25
Validation Model Predicted vs. Measured Results, Axial Direction, 4.25 mm Below the Outer Surface

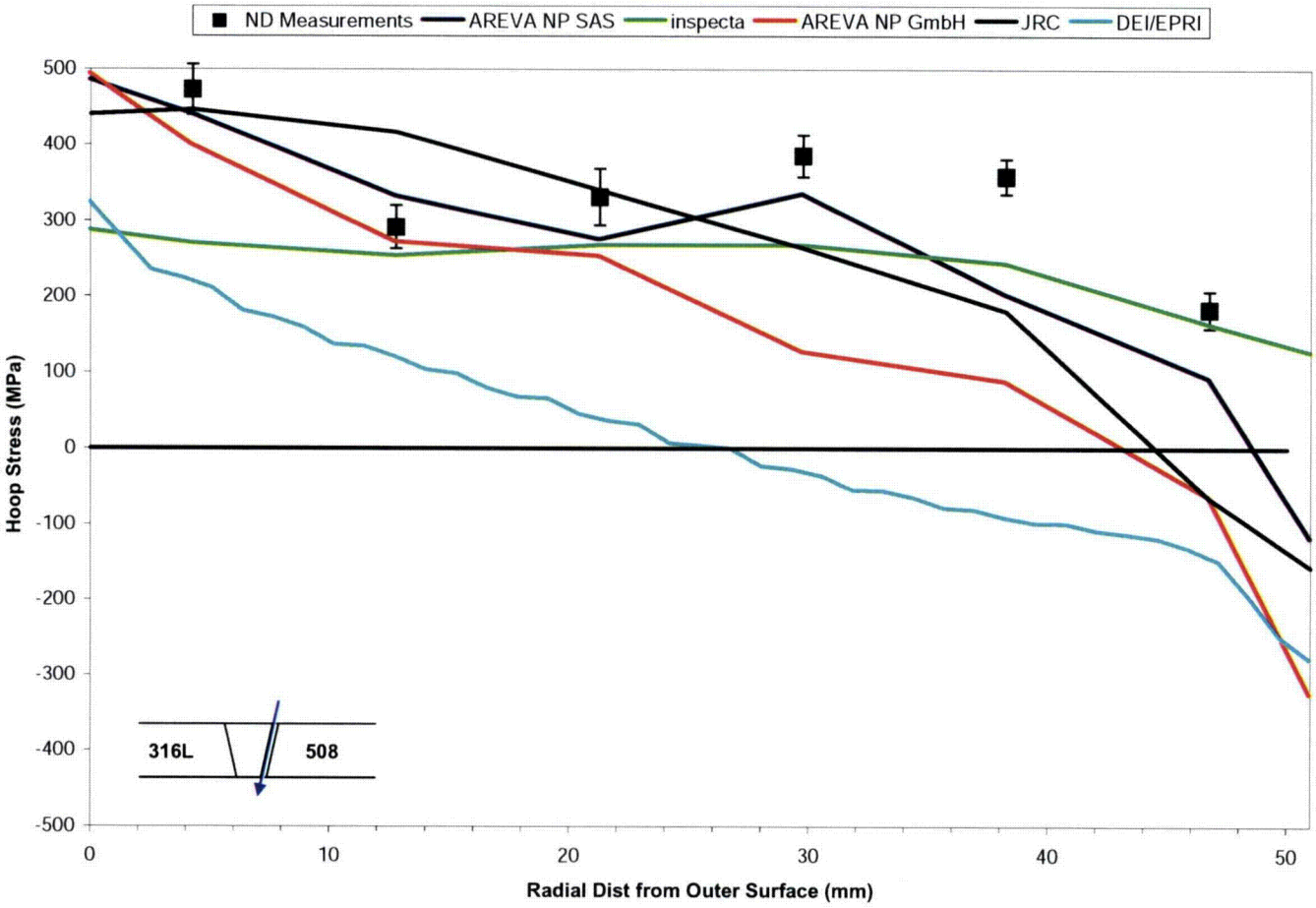

Figure 3-26
Validation Model Predicted vs. Measured Results, Hoop Direction, Through-Wall Section at Butter Layer Center

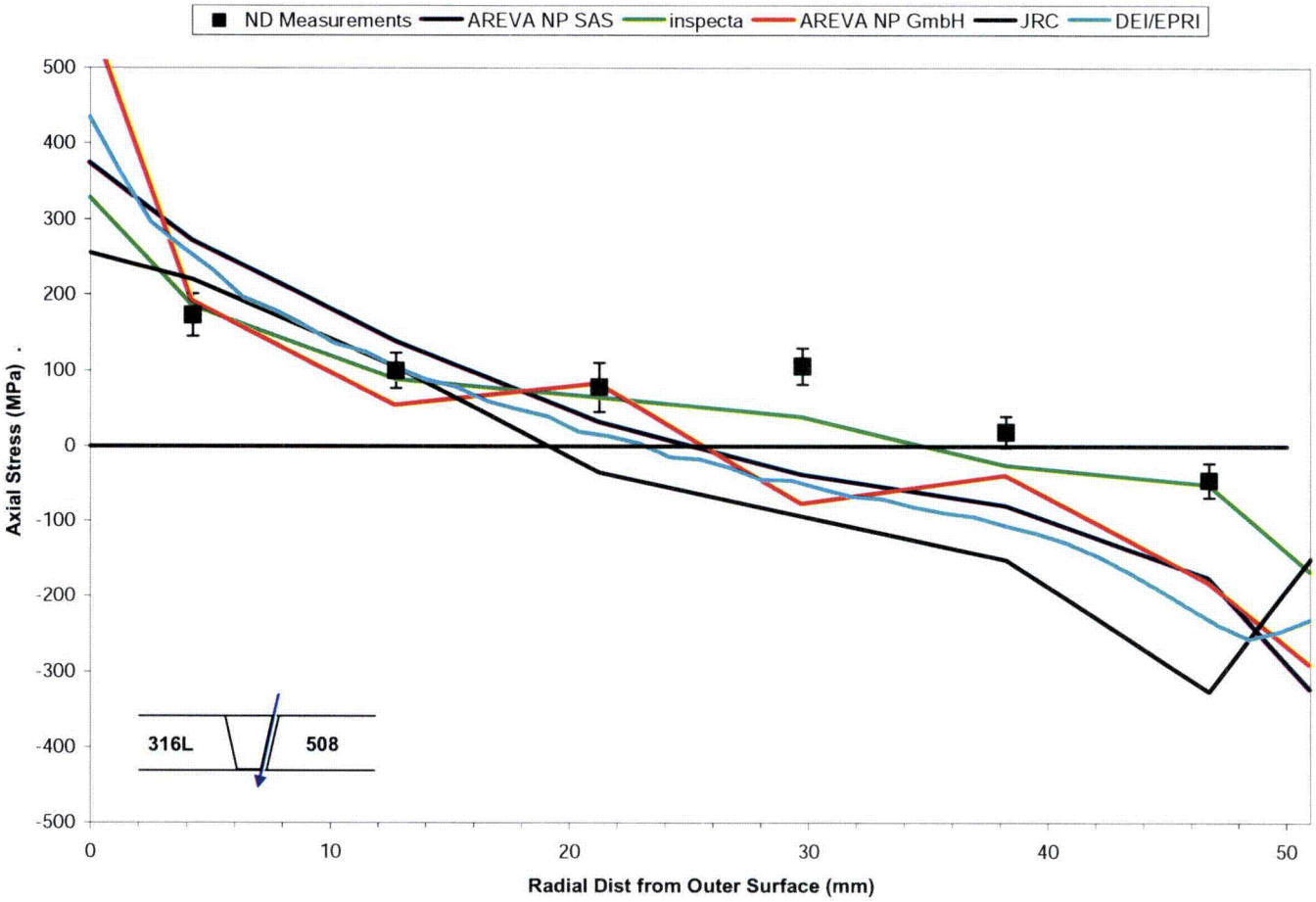

Figure 3-27
Validation Model Predicted vs. Measured Results, Axial Direction, Through-Wall Section at Butter Layer Center

4
CRACK GROWTH MODELING

The purpose of this section is to describe the fracture mechanics and crack growth calculations that were used to take into account the change in flaw shape that will occur with varying crack tip stress intensity factors (SIFs, also denoted as K) along the crack front. These calculations were performed using software developed specifically to consider crack growth with an arbitrary profile geometry. This section describes the overall approach used for the calculations. Additional results from a sensitivity matrix of loading cases are provided in Section 7. This section also includes, as an example, the detailed results from the Phase I portion of the overall work scope, where the loads and initial flaw geometry used in previous flaw growth analyses were used to perform the arbitrary profile crack growth calculations.

4.1 Modeling Approach

4.1.1 FEA Model

Cylindrical FEA Model

Finite element analysis was used to calculate the crack tip stress intensity factor (SIF) for all flaws considered in this calculation. Figure 4-1 shows the FEA model geometry for a typical starting surface flaw case. As shown in Figure 4-1, the analysis model is three-dimensional and is symmetric about both the plane of the flaw and about the deepest point of the flaw (quarter symmetric). The geometries of the nozzle welds are simplified to be represented by a basic cylindrical geometry with a strip of material representing the weld. As shown in Section 2 and Section 3 of this report, the actual geometry of the dissimilar metal welds is a single U-groove attachment to a safe end, which then transitions in thickness and diameter over a short length to the attached piping. The simplified geometry assumption permits more analysis cases to be performed since the models are smaller and solve more quickly. Additionally, the simplified cylindrical geometry more readily permits application of arbitrary through-wall stress distributions. The effect of the actual nozzle geometry is also considered as part of the sensitivity case matrix in Section 7.

The meshes generated for this calculation make use of 8-node brick elements, with collapsed-front crack-tip nodes. The 8-node brick elements were used for their computational efficiency, particularly for cases where contact surfaces were being used. The crack front region of the fracture mechanics model's mesh is detailed in Figure 4-1. This figure shows the arrangement of the nodes near the crack front region, demonstrating the concentric rings of nodes that radiate outwards from the crack front location. The rings are used to perform J-integral calculations as part of the analysis model post-processing.

Comparisons were performed between fracture mechanics models using 8-node bricks and those using 20-node bricks with quarter-point location of the mid-side nodes. No significant difference was found between the crack tip SIF values calculated, nor between crack growth results for the two model types. Additionally, as detailed in Section 4.6, a mesh convergence study was performed with the 8-node brick mesh; the results indicate that sufficient mesh refinement is being used. These effects were explored by Anderson in Reference [38], where he found the J-integral method of K_I calculation to be insensitive to the presence of a quarter-point singularity in the mesh and, to a certain degree, the level of overall mesh refinement. He does note that the first J-integral contour is more sensitive to these effects, but any remaining contours beyond the first are not affected.

External forces and moments are applied as pressures at the edge of the model, with moments applied as a pressure gradient. The desired residual through-wall stress distribution is applied to the model using differential thermal expansion loading in the strip of weld material. Because the simulated residual stress distribution is generated through displacement, any effect of stress redistribution caused by elastic unloading in the model is captured in the analysis. A sensitivity case that considers the axial thickness of the strip of weld material is included in Section 7. Stress distributions are typically applied to the three-dimensional model in an axisymmetric fashion, varying through the wall the same at all circumferential positions. However, in some cases, they are applied as varying in the circumferential direction as well as through the wall to simulate the effect of local repairs. Figure 4-2 is an example axial stress plot showing an applied axisymmetric through-wall stress distribution in the fracture mechanics model. Figure 4-3 is an example axial stress plot for a local repair stress field distribution. In order to generate these stress plots, a zero axial displacement boundary condition is applied to the crack face.

Nozzle-to-Safe-End FEA Model

As noted above, in addition to the simplified cylindrical geometry used for the majority of cases, a selection of sensitivity cases were evaluated using actual safety/relief and surge nozzle geometries. The general characteristics of the nozzle geometry models are similar to those of the cylinder models; both types of models are three dimensional and make use of 8-node brick elements. The nozzle geometry models are symmetric about the deepest point in the flaw, but not about the plane of the flaw (half symmetric). A model geometry for the safety/relief nozzle is shown in Figure 4-4, and a model geometry for the surge nozzle is shown in Figure 4-5. The safety/relief nozzle model geometry profile is identical to the welding residual stress nozzle analysis case described in Section 3. The profile for the surge nozzle model geometry is slightly simplified relative to the welding residual stress nozzle geometry as follows: 1) the inside diameter of the nozzle region is the same as the finished dissimilar metal weld dimension, and 2) the region near the safe end to pipe weld is all at the inside diameter of the pipe.

The appropriate force and moment for the case being considered are applied at the piping end of the model, and the nozzle end is held fixed in the axial direction. Two different methods are used to apply a desired welding residual stress distribution to the fracture mechanics models, depending on the model case. When an arbitrary axial stress distribution is desired, it can be imposed on the model using the same differential thermal expansion technique at the weld material as used for the cylinder models. For these cases, the model is iteratively solved until the through-wall temperature distribution results in the desired stress distribution at the location of

the crack plane. Example cases of imposed through-wall distributions are shown in Figure 4-6 and Figure 4-7. In order to generate these stress plots, the crack faces are held coupled together.

In addition to the arbitrary stress distributions considered for the safety/relief and surge nozzle cases, a safety/relief case was also considered where the welding residual stresses were interpolated into the fracture mechanics model geometry. The interpolation process includes the complete triaxial stress state of the model, rather than axial stresses alone. The stress state for the fracture mechanics model is an elastic one based on the elastic-plastic stress state of the welding residual stress model. Therefore, all calculations are based in linear elastic fracture mechanics. The starting welding residual stress model for this case includes the complete nozzle butt weld, but without the stainless steel weld. The circumferential flaw in the fracture mechanics model was placed at the axial location of highest ID axial stress (see Figure 3-9). The axial stresses resulting from the imposed stress distribution for the fracture mechanics model are shown in Figure 4-8. Comparing the welding residual stress model results to those resulting from interpolation, it is demonstrated that the interpolation process generates a model stress distribution that closely resembles the welding model stress state. Similar to other analysis models, the crack face is loaded with pressure and the piping end of the model is loaded with axial force and bending moment prior to being solved.

4.1.2 Calculation of Crack Tip Stress Intensity Factor

Because the model is linear elastic, the J-integral calculations are not of the total strain energy (since there is no plastic strain), but of the elastic strain energy, frequently referred to as G. For convenience and for consistency with the software outputs, the strain energy values calculated from the ANSYS results files (using an external program called FEACrack, see Section 4.2) are hereafter referred to as J values. Using the relationship between J and K for the special case of linear elastic materials and using plane strain conditions, the crack tip stress intensity is calculated from the J-integral values with the following equation:

$$K = \sqrt{J \times E'} \qquad [4\text{-}1]$$

where,

K = crack tip stress intensity factor (psi•in)
J = calculated J-integral value (psi•in)
$E' = E / (1-\nu^2)$
E = Young's modulus
ν = Poisson's ratio = 0.30

It is noted that the J-integral value calculated by the software results from Mode I loading due to the symmetry boundary conditions of the model.

4.1.3 Crack Growth for an Arbitrary Flaw Shape

Once the crack tip SIF along the entire front has been calculated, the results are used to determine the shape of the flaw after a small time increment has passed. The crack growth

increment at each point (i.e., node) on the crack front is based on the SIF calculated at that point, with growth occurring in the direction normal to the crack front. The crack growth rate is calculated using the SIF in combination with the MRP-115 [21] crack growth rate equation for Alloy 182 weld metal, which recommends a SIF exponent of 1.6 and the use of a zero SIF threshold. Sensitivity cases for the SIF-dependence of the crack growth rate are also performed as part of the case matrix described in Section 7.

The crack growth rate values were input directly to the FEACrack software. The change in crack profile for each growth step and the time required for each growth step are calculated in a fully explicit manner from the previous step, based on an input step size for growth at the point of maximum SIF.

It should be recognized that the standard assumption of uniform and isotropic material resistance to PWSCC crack growth is assumed in the crack growth simulations. However, weld metal materials, including Alloy 82/182 piping butt welds, have a complex and anisotropic microstructure that can result in significant spatial and directional variability in the crack growth rate [21]. Furthermore, laboratory experience often shows a fingerlike crack front pattern, indicating greater through-wall extension in comparison to lateral extension than would be expected for the case of uniform and isotropic material resistance. This sort of behavior is commonly observed in the laboratory compact tension specimens used to measure PWSCC crack growth rate in Alloy 82/182 weld materials [21]. In 2004, EPRI published an MRP-sponsored laboratory study [41] that investigated the effect of weld metal microstructure on PWSCC initiation and growth in pressurized test capsules fabricated from Alloy 182 weld metal material. With regard to patterns of crack extension observed, this study concluded the following:

> "The cracks exhibited an unusual aspect ratio in that they never showed a large lateral surface extent, even when they extended through the wall thickness. This is a very different feature compared to PWSCC in Ni-base alloys such as Alloy 600. The aspect ratio is thought to relate to indications of crack arrest observed at low energy grain boundaries in Alloy 182."

The laboratory studies of capsule and compact tension specimens indicate that actual crack growth behavior in Alloy 82/182 weld metal materials is likely to be more favorable toward through-wall penetration and leakage occurring prior to rupture than is predicted under the standard assumption of uniform and isotropic material resistance. This is because actual effective growth rates in the lateral (i.e., circumferential) direction for a circumferential surface flaw on the weld ID may be lower in comparison to the growth rate in the depth direction (toward through-wall penetration and leakage) than is predicted by models assuming uniform and isotropic dependence of the crack growth rate on the SIF in combination with high assumed axial stresses around the ID surface.

4.1.4 Flaw Shape Transition

For every fracture mechanics analysis case considered in the sensitivity case matrix described in Section 7, the initial flaw is either a partially circumferential or fully circumferential (depending on the case) ID surface flaw. The flaw is allowed to grow at an appropriately refined growth step until the deepest part reaches about 93% of the wall thickness. At this point, the flaw size is

projected to where the deepest part reaches 100% wall thickness, and a new, through-wall (either true through-wall or complex crack) mesh is generated. In some cases, a partially circumferential ID surface flaw reaches around to become a fully circumferential ID surface flaw before it reaches through-wall; an intermediate variable depth circumferential surface flaw profile is generated in these cases. When the new through-wall mesh geometry is generated, the projected crack front from the surface flaw case is used as the through-wall flaw profile, and any regions where the remaining ligament is less than 10% of the wall thickness are converted to an open crack face (forming the through wall or complex crack). In this way, thin ligaments of material are assumed to break through immediately, without taking credit for additional time to grow through the region. An example of this mesh transition is included in Figure 4-9, which shows the final step of the surface crack growth and the first step of the complex crack growth.

4.2 Fracture Mechanics Calculation Software Background

The fracture mechanics model geometry is generated by FEACrack, a specialized fracture mechanics pre- and post-processing software code. The base model geometry, the model external loads, and the initial flaw geometry were all defined with the FEACrack software. Using this information, the software generates a finite element mesh that may be solved to calculate the stress state of the model. FEACrack is not a finite element analysis code; however, it is capable of automating the process used to generate a mesh and analyze that mesh on a variety of commercial analysis software codes. The analyses of the fracture mechanics models were performed using ANSYS Version 10.0, installed on the same computer as FEACrack.

Once the model is analyzed, the post-processing portion of FEACrack reads the ANSYS results and performs J-integral calculations at a number of points along the crack front. J-integral calculations are performed at each of five concentric rings set around the collapsed crack front nodes to determine an average J-integral value. The contour integral closest to the crack front is not used in the calculation; this does not impact the accuracy of the calculation. The variation of the average from each of the individual J-integral values determines the "contour dependence" of the average J-integral value, and is performed as an internal check on the numerical accuracy and mesh refinement of the FEA model. The J-integral contour dependencies are generally verified to be lower than 5% per the recommendation of the fracture mechanics software. The exception is at the one or two points near the surface of the flaw. Anderson notes in [38] that the J-integral value at the surface point of the flaw is frequently difficult to calculate with path independence. When this occurs, FEACrack will linearly extrapolate the J-integral value for the points where the path dependence is high, basing the extrapolation on previous values along the crack front.

FEACrack also has the capability of interleaving pre- and post-processing of a fracture mechanics model with the model analysis solution in ANSYS to perform crack growth analysis calculations. The crack growth analysis sequence is as follows: an initial mesh is generated, the FEA model is solved, the results are read in by FEACrack, and a new mesh is generated by FEACrack to be solved. The new mesh is generated based on the SIF results from the previous mesh and the desired crack growth step.

4.3 Extensions to Fracture Mechanics Software

A key task in performing the analyses described in this report was to extend the capabilities of FEACrack to consider flaws of arbitrary dimensions. For example, instead of specifying a surface crack with depth and length values, then fitting a semi-ellipse (or other flaw shape) through those end points, the analysis model needed to be able to define a flaw shape based on user inputs for coordinates of the entire crack front in the crack depth and crack length directions. Additionally, once the user-defined mesh geometry was input, growth of the flaw was to be calculated at all points along the crack front, rather than only at the depth and surface positions. Similar modifications were required for through-wall flaws. Based on the results for surface crack growth calculations, a new flaw shape was also developed to perform the through wall portion of the crack growth calculations. This flaw shape is 360° on the ID surface and partially circumferential on the OD surface, commonly referred to as a complex crack shape.

The following extensions were incorporated into FEACrack directly as a part of this project:

- Custom surface crack geometry mesh, part circumference, see example in Figure 4-10
- Custom surface crack geometry mesh, full circumference, see example in Figure 4-11
- Custom complex crack geometry mesh (360° on ID and part circumference on OD), see example in Figure 4-12
- Custom through-wall crack geometry mesh (part circumference ID and OD), see example in Figure 4-13
- Automated crack growth of all custom crack geometries, including crack growth at all points along the crack front
- Redistribution of crack front node spacing for automated crack growth to prevent mesh errors during crack growth, see Figure 4-14.

In addition to these meshing extensions, FEACrack was updated to include an optional contact surface plane that enforces crack face symmetry boundary conditions. Generally, the crack front will not grow into a compressive region where the crack face would be pushed through the symmetry boundary condition. As the local stress field grows more compressive, the local crack front K drops, and the crack stops growing. However, in cases where there is a low driving K along the entire crack front, the crack front may step into a region where the crack face is pushed through the symmetry plane of the model. This inward displacement, however, generates strain energy, leading to a positive crack tip SIF and crack growth. In these cases, the contact surface plane is necessary to prevent the crack face from pushing through the symmetry plane; the calculated strain energy then goes to zero and crack growth does not continue.

4.4 Phase I Crack Growth Results

4.4.1 Preliminary Phase I Results

In order to evaluate the impact of the extensions to FEACrack described above on the predicted crack shape, an initial (Phase I) analysis was performed using the geometry and load inputs from

previous Wolf Creek safety/relief nozzle flaw assessments [4]. This analysis case was performed for growth from a partially circumferential surface flaw to the final step where the deepest point of the flaw reaches through-wall. The Phase I analysis was intended as a test of the methodologies to see if it produced a different flaw shape at through-wall versus earlier assumptions for semi-elliptical crack growth. The Phase I analysis case was performed a total of three times over the initial weeks of the project, with results of each analysis reported in intermediate meetings. Each time the analysis was performed, the results were used to refine the understanding of the behavior of the model and to improve the methods used to perform the analysis.

The initial Phase I analysis revealed that the through-wall stress distribution, featuring a high ID surface stress, resulted in a part circumference surface crack growing rapidly to a full circumference surface crack before any significant advance through the wall at the deepest point. Addressing this result required the addition of the custom full circumference surface crack mesh extension to FEACrack. The initial analysis was also performed without nodal redistribution along the crack front, a feature that was added as a result of this initial trial. While performing the analysis, it was necessary to manually readjust the crack front nodes at every growth step in order to maintain an appropriate mesh. The limitations on automation restricted the crack growth refinement that could reasonably be used, including using only five steps growing through-wall once the flaw reached full circumference. Despite these limitations, the initial Phase I analysis results demonstrated that the resulting flaw shape was significantly different from one that was assumed to maintain a semi-elliptical shape, and that the remaining uncracked cross section was significantly greater than previously calculated. An illustration of the flaw growth for this analysis is shown in Figure 4-15. The time to reach through wall in the first analysis was calculated to be 5.1 years.

The Phase I analysis was performed a second time using the improvements to FEACrack to address the limitations from the previous iteration, including automatic node redistribution and the use of a full circumference ID surface flaw when appropriate. In addition, a number of other refinements were made to the calculation methodology. The analysis mesh was adjusted to have more crack front nodes at the surface point of the mesh, instead of evenly distributed. Much greater growth step refinement was also used to maintain flaw shape stability during the automatic growth of the crack. Additionally, analyses were performed to determine a "natural" flaw shape for the applied through-wall stress distribution, rather than starting from a semi-elliptical flaw shape. It was found that a semi-ellipse starting flaw tended to become rapidly deeper towards the surface side of the flaw; the natural flaw shape would tend to remain geometrically similar to its original shape during growth. The natural flaw shape was estimated by starting from a semi-elliptical flaw slightly smaller than the desired depth and length, then allowing the flaw to grow until the desired depth and length were reached. Finally, minor adjustments were made to the through-wall temperature distribution to improve the resulting stress distribution. An illustration of the flaw growth for this analysis is shown in Figure 4-16. The time to reach through wall in the second analysis was calculated to be 7.5 years.

At the completion of the second Phase I analysis, it was assumed that the increase in time was the result of the refined time step and other improvements to the meshing routines. However, in order to examine the impact of the through-wall stress distribution alone on the crack growth time, a final Phase I model analysis was performed with all other refinements and improvements included, but the applied temperature was identical to the first Phase I analysis. An illustration

of the flaw growth for this analysis is shown in Figure 4-17. The time to reach through wall in the third analysis was calculated to be 5.36 years.

The results of the iterations on the Phase I analysis methodologies demonstrated that the overall time to reach through-wall could be affected by the through-wall distribution. However, despite the time differences, the shape of the final through-wall flaw remained similar among all three analysis iterations, as demonstrated by Figure 4-18. Also shown in this figure is the final through-wall profile for the industry white paper [4] crack growth calculation for the same Phase I input parameters but under the assumption of a semi-elliptical flaw shape driven by the SIF calculation at the deepest and surface points on the semi-ellipse. This comparison demonstrates the large degree to which the semi-ellipse assumption overestimates the crack area at the point of through-wall penetration.

4.4.2 Phase I Results Using Final Mesh Parameters of Section 7 Sensitivity Matrix

A final analysis of the Phase I case was also completed using the same meshing parameters and analysis methods used to perform the final Section 7 sensitivity matrix analysis cases. This analysis evaluated flaw growth to through-wall, then continued the analysis of the complex flaw as it grows to critical flaw size. The initial flaw for this analysis is the same as the preliminary Phase I calculations, with a depth equal to 26% of the wall thickness, a 21:1 aspect ratio, and the "natural" flaw shape profile investigated in the preliminary Phase I work.

The progression of flaw profiles starting from the part-circumference surface flaw is shown in polar coordinates in Figure 4-19, and in Cartesian coordinates (superimposed on the cylinder cross section) in Figure 4-20. The initial through-wall flaw shape calculated by assuming the flaw remains semi-elliptical is also shown on these figures. These figures also indicate the growth step corresponding to each flaw profile. The time corresponding to the progression of flaw profiles for the Phase I calculations is shown in Figure 4-21 for the surface flaw growing to a through-wall flaw and in Figure 4-22 for the growth of the complex flaw around the cross section. The crack tip stress intensity along the crack front for the growing partial circumference flaw is shown in Figure 4-23. This figure shows generally smooth values along the crack profile.

Figure 4-24 through Figure 4-27 are plots of various flaw parameters as a function of time. A graph showing the change in depth of the surface flaw as a function of time, starting from the 26% deep partial circumference flaw, is shown in Figure 4-24. This figure also indicates the point where the flaw transitions from a partial to a full circumferential surface flaw. Figure 4-25 plots the aspect ratio of the partial circumference surface flaw as a function of time, until the flaw becomes fully circumferential. This figure indicates that the flaw generally maintains its long aspect ratio as it grows around the circumference. Figure 4-26 plots the percentage of the cylinder surface area covered by the flaw as a function of time, showing the surface crack (both partial and full circumference) and complex crack regimes of crack growth. The small discontinuities in the area at the transitions result from the assumed ligament breaking as the flaw reaches the edge of the section. Figure 4-27 shows the flaw shape function as a function of time; the shape function is defined as the actual flaw cross section divided by the cross sectional area of a semi-elliptical flaw with the same depth and length. This figure indicates that the flaw initially has a larger area than the equivalent semi-ellipse, but quickly develops a shape that has a smaller cross section than the equivalent semi-ellipse.

Figure 4-28 is a plot showing the stability margin on load as a function of time, starting from the initial partial circumference surface flaw and progressing to a complex flaw until a load factor of 1.0 is reached. As shown in this figure, the partial circumference flaw starts with a large margin on load that progresses steadily downward as the flaw grows through-wall. The load factor and leak rate as a function of time once the flaw reaches through-wall are shown in Figure 4-29; this plot is similar to plots in Section 7 for other sensitivity matrix cases. The figures shows that for the Phase I case, a time of about 70 days is required for the flaw to grow from 1 gpm leakage to a stability margin on load of 1.2.

4.5 Stress Intensity Factor Verification

The methodologies used in this report to generate, solve, and post-process a finite element analysis mesh for an arbitrary surface crack front profile were compared to an independent calculation performed by EMC^2, a contractor to the NRC, as a means of benchmarking the calculations. A set of four proposed crack front profiles were generated from specified combinations of mathematical functions. By defining them in terms of analytical functions, the profiles are completely defined for any arbitrary grid spacing and are not dependent on a particular mesh refinement. The four profiles selected are shown in Figure 4-30, both in planar coordinates and in the cylindrical coordinates used to generate the actual mesh. A common set of external loads (membrane plus bending stress) were applied to the crack models.

The calculation was performed using FEACrack to generate the mesh, ANSYS to solve the FEA mesh, and FEACrack to post-process the analysis results and calculate the crack tip SIF along the crack front. The independent calculation performed by EMC^2 used their own software to generate the mesh, and ABAQUS to solve the model and calculate the crack tip SIF along the crack front. The comparison for K solutions for all four crack fronts is shown in Figure 4-31. This figure demonstrates excellent agreement between the two independent analyses.

4.6 Crack Growth Convergence Checks

4.6.1 Temporal Convergence Check

As noted above, the amount of growth between successive crack growth steps is a specified parameter in the crack growth analysis, and the cumulative amount of time required to grow the specified distance is an output from the analysis. If the specified growth step is too large to capture the variations in loading through the wall of the model, an inaccurate final crack size will result. In order to check that sufficient growth refinement was being used, comparisons were performed for surface crack and complex crack growth progressions with about twice the normal growth step refinement. This convergence check is referred to as the temporal convergence check since a reduced growth step size also corresponds to refinement in the time step size.

Case 1c, defined in Section 7 as corresponding to an initial 10% through-wall 360° surface flaw, was used as the base case for this study. The normal surface crack growth procedure was applied in each case, with a growth step of 0.040 inches for the base case versus a growth step of 0.016 inches for the refined case. Additionally, the final growth step was made from a depth of 93% through-wall to 100% through-wall because of the difficulty in meshing very deep flaws. For the

complex crack portion of the convergence check, the cracks were grown from the same initial complex crack profile, with both the original and refined growth step size until a desired number of steps were achieved. For the refined growth step size case, the step size was halved and the number of growth steps doubled, resulting in the same final crack length on the weld OD. The complex flaw base case growth step is 0.072 inches, versus a refined case growth step of 0.036 inches.

The comparison results for the temporal convergence check are shown in Table 4-1 and Figure 4-32, which demonstrate an acceptably small level of temporal numerical convergence error. The final surface crack and complex crack profiles are nearly identical for the case of varying growth step size. Based on these results, it is concluded that a sufficient level of growth step refinement is assumed in the sensitivity matrix of crack growth calculations of Section 7.

4.6.2 Spatial Convergence Check

In addition to the preceding temporal convergence check, a spatial grid refinement convergence study was also performed using the same initial surface crack and complex crack cases. For the refined grid case, the number of elements in the radial and axial directions was increased by about 50%. The number of elements in the circumferential direction was maintained at the same normal level due to limitations in the meshing software.

The comparison results for the spatial convergence check are shown in Table 4-1 and Figure 4-33, which also demonstrate an acceptably small level of spatial numerical convergence error. The final surface crack and complex crack profiles are nearly identical for the case of varying grid refinement. Based on these results and the relatively large number of nodes assumed in the circumferential direction (typically 100 over 180°), it is concluded that a sufficient level of grid refinement is assumed in the sensitivity matrix of crack growth calculations of Section 7.

4.7 Validation Cases

As a consistency check of the ability of the crack growth methodology described above to predict actual plant experience, the large circumferential crack detected at the BWR Duane Arnold plant was applied as a validation case. A cross section through the 360° part-depth crack at Duane Arnold is shown in Figure 4-34 [22]. Crack initiation and growth were attributed to the presence of a fully circumferential crevice that led to development of an acidic environment because of the oxygen in the normal BWR water chemistry, combined with high residual and applied stresses as a result of the geometry and nearby welds, including the unusual repair weld made on the outside of the Alloy 600 safe end to correct a safe end fabrication error. The water chemistry conditions that contributed to cracking at Duane Arnold do not exist for the case of Alloy 82/182 piping butt welds in PWR plants.

In order to apply the Duane Arnold experience to the crack growth methodology described above, a welding residual stress analysis of the Duane Arnold configuration, including the weld repair, was performed [23]. The calculated through-wall variation in welding residual stress (including application of normal operating temperature but not pressure) at the general crack

location is shown in Figure 4-35. The polynomial fit shown in this figure was assumed in the validation case, as were reported operating pressure and design piping loads [23].

The crack profile calculated in the validation check is shown in Figure 4-36 versus the actual Duane Arnold crack profile. This profile is based on the assumption of an initial 30% through-wall uniform depth 360° surface flaw, in combination with the MRP-115 [21] crack growth rate dependence on stress intensity factor. (The assumption of an initial 360° surface flaw is reasonable given that the crevice between the thermal sleeve and safe end is expected to have acted as a crack starter.) The agreement shown in the predicted and actual crack profiles in Figure 4-36 is reasonable. However, because the simulated crack profile attained is sensitive to the particular assumed initial crack profile and no information is available on the actual crack profile at earlier times, this validation case must be interpreted as a consistency check of the crack growth methodology versus the Duane Arnold experience. In addition, it is recognized that the effective turn in flaw direction from the axial direction of the crevice to the general radial direction of the crack is a complication that cannot be directly addressed by the crack growth methodology.

Table 4-1
Results of Temporal and Spatial Convergence Study for Case 1 360° Surface and Complex Crack Growth Progressions

	Case	Sensitivity Description	Time (years) (Note 1)	% Difference in Time	Maximum Absolute Difference in Depth (in)	Maximum Abs. Difference in ID Circumferential Position (in)
360° Surface Crack	30 Steps - Original Mesh	Base Case	17.42			
	70 Steps - Original Mesh	Temporal	17.18	-1.40%	0.0158	0.0102
	30 Steps - Refined Mesh	Spatial	17.21	-1.24%	0.0021	0.0005
Complex Crack	65 Steps - Original Mesh	Base Case	0.725			
	130 Steps - Original Mesh	Temporal	0.701	-3.27%	0.0127	0.0371
	65 Steps - Refined Mesh	Spatial	0.721	-0.52%	0.0013	0.0021

Note 1: Time for the 360° surface crack case is time to through-wall and for the complex crack case is time until desired number of steps has been executed.

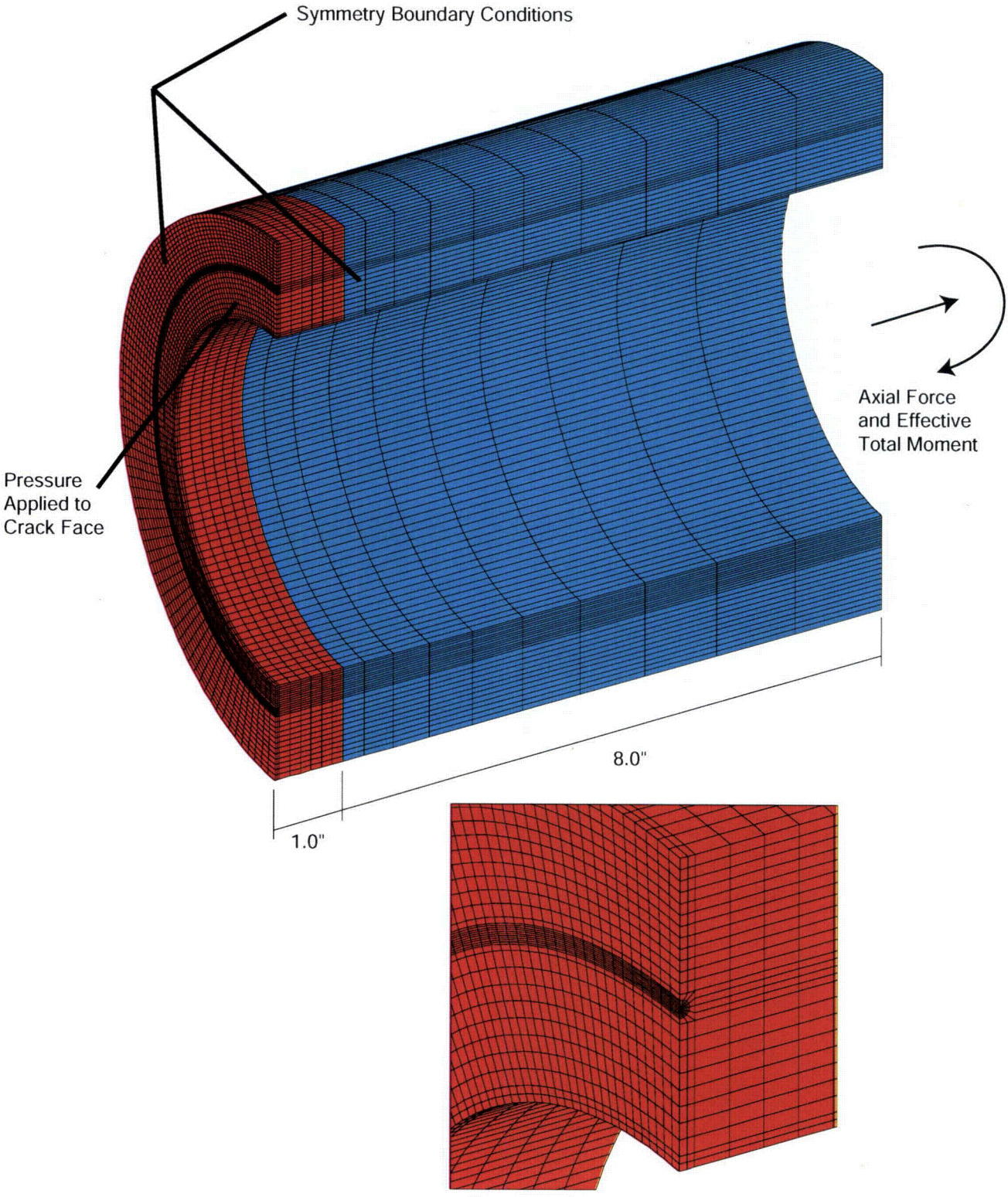

Figure 4-1
Fracture Mechanics Finite Element Analysis Model

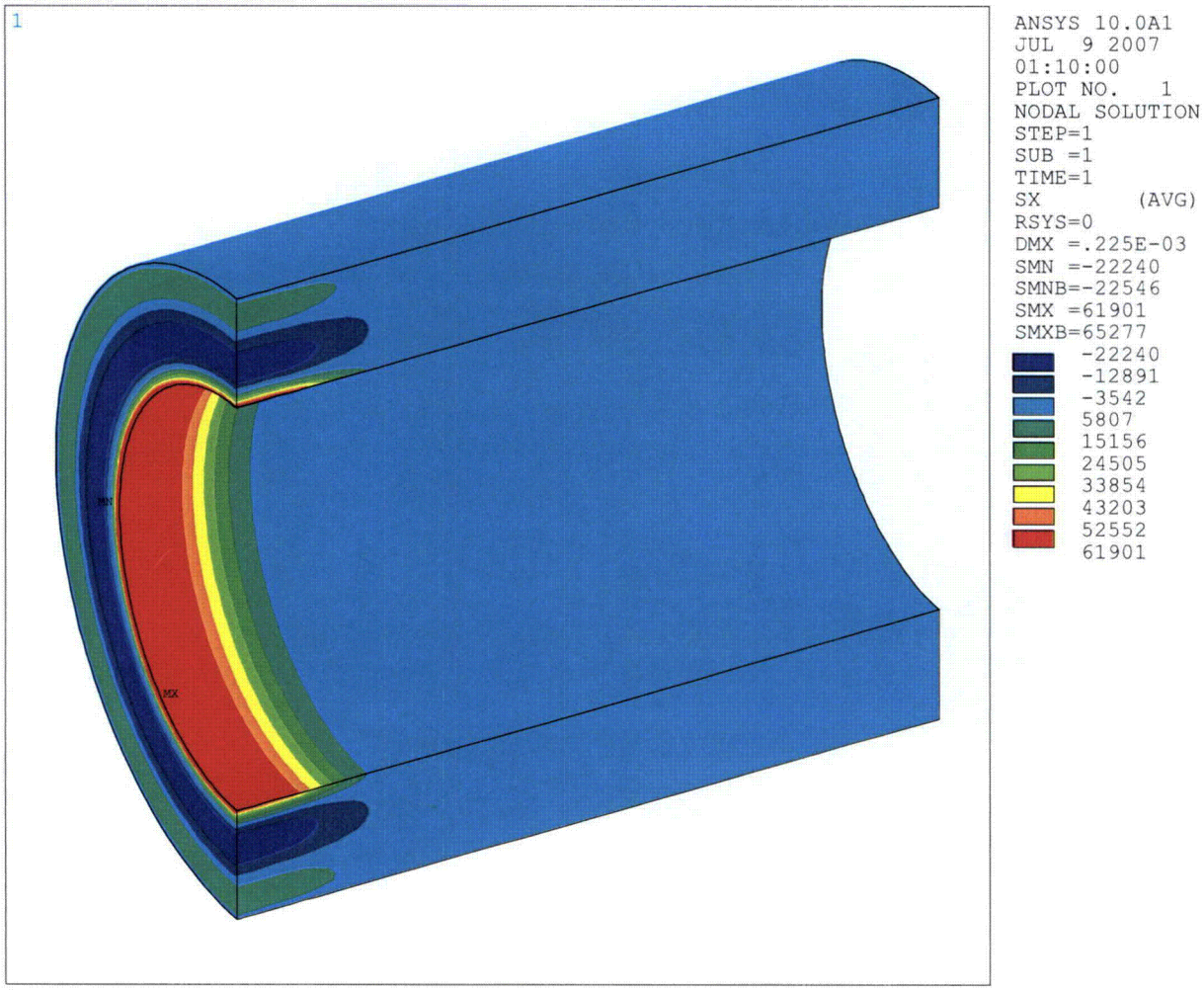

Figure 4-2
Axisymmetric Through Wall Stress Distribution Example

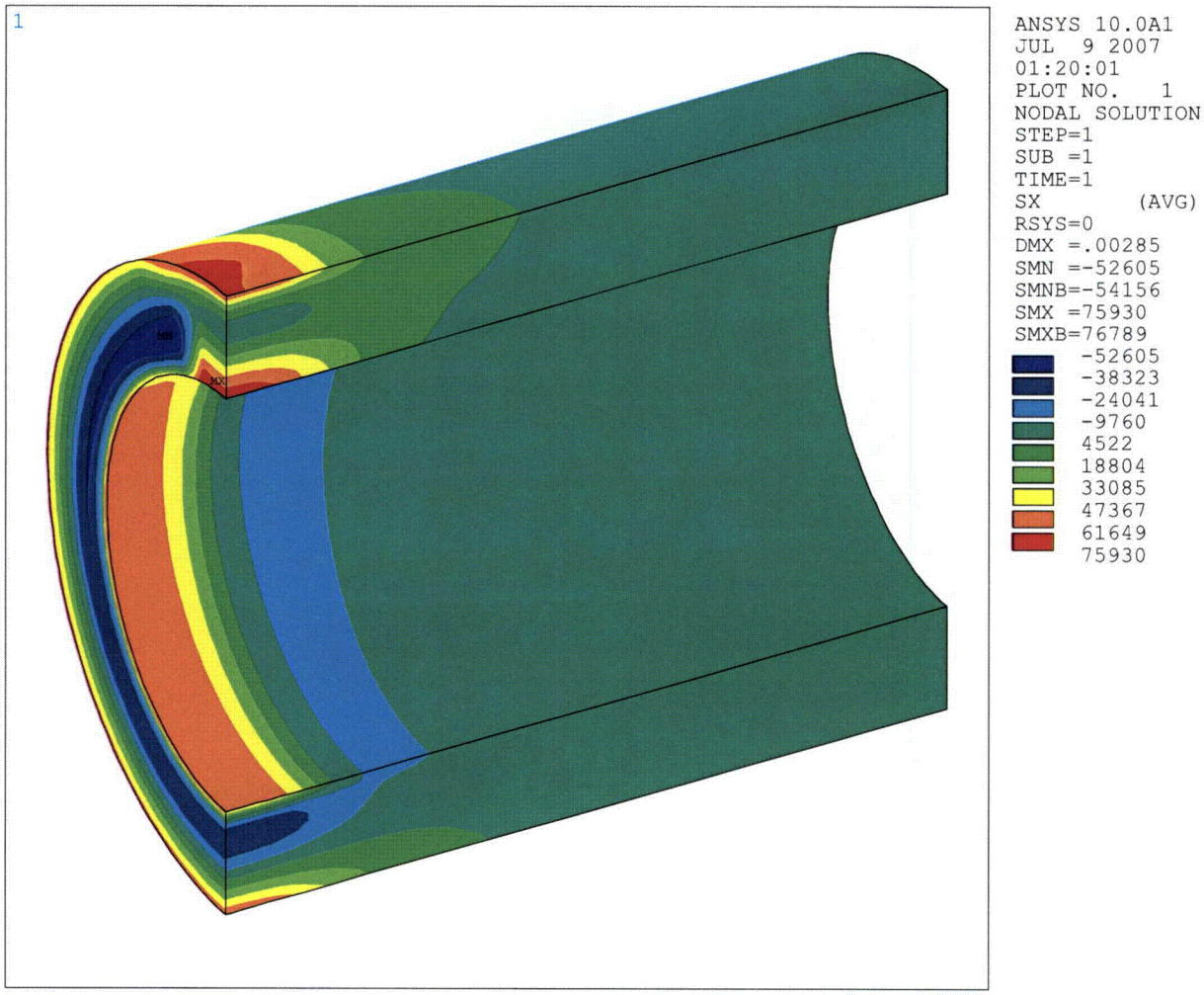

Figure 4-3
Circumferentially Varying Through Wall Stress Distribution Example

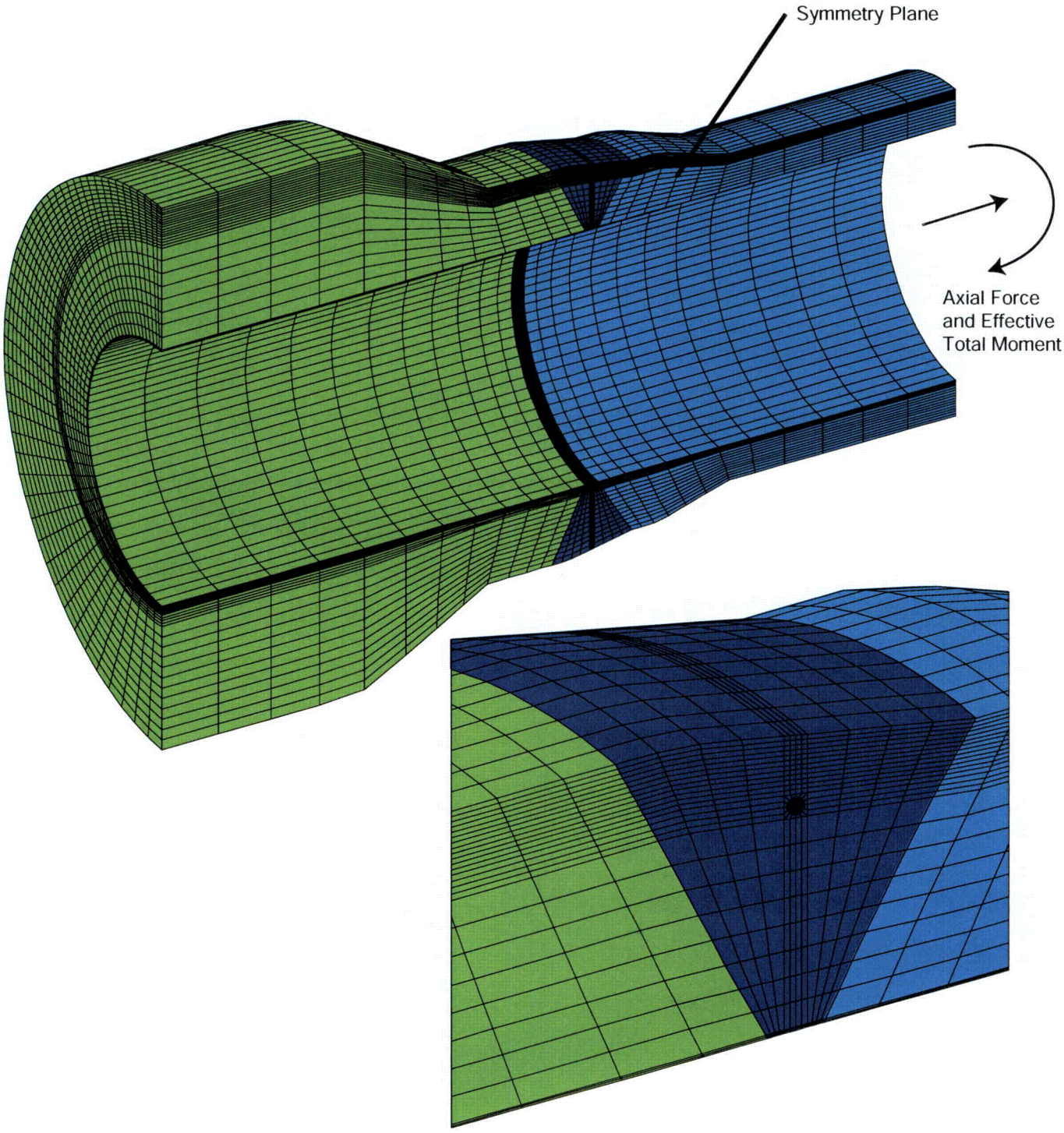

Figure 4-4
Safety/Relief Nozzle Fracture Mechanics Model (Nozzle Geometry)

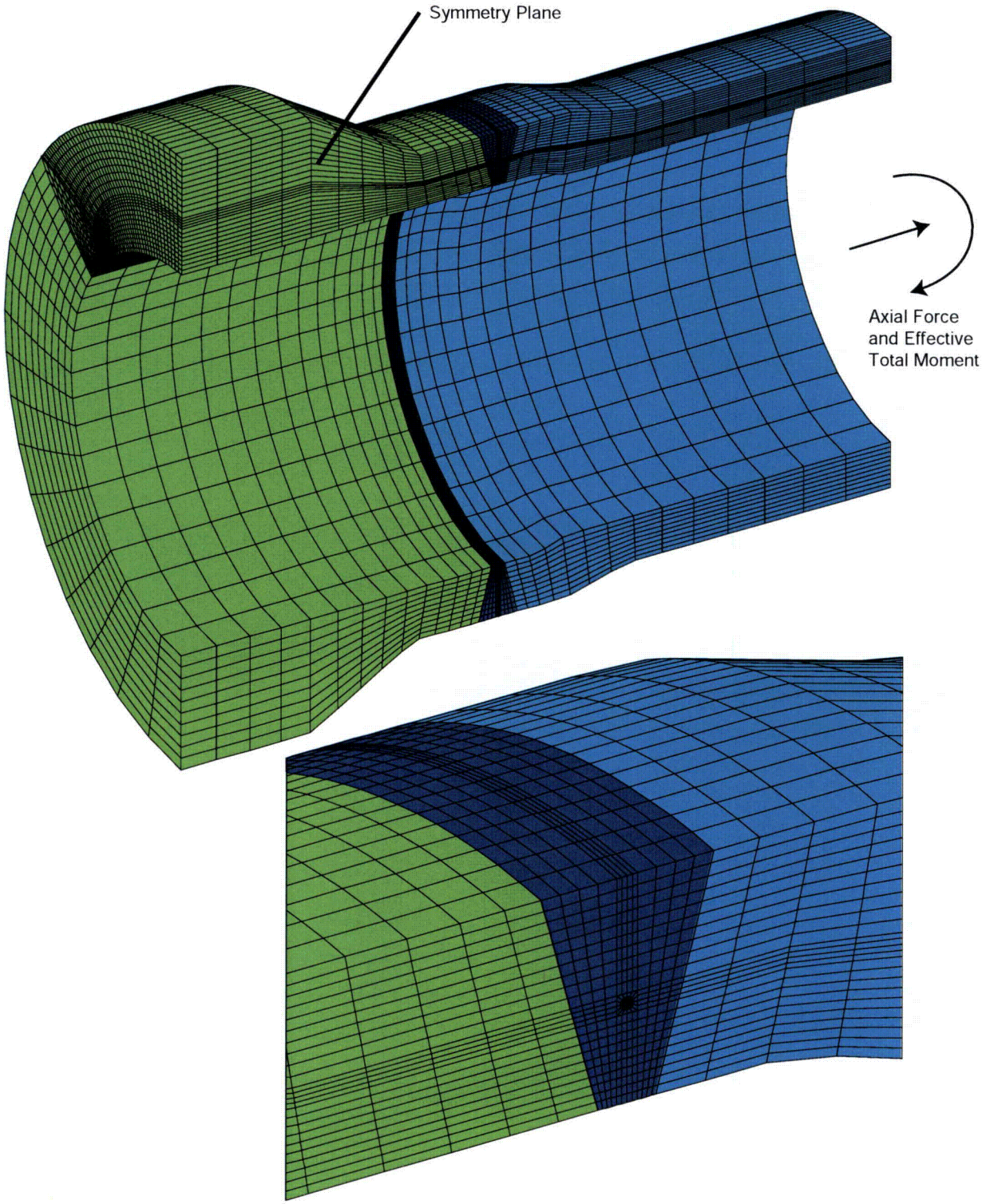

Figure 4-5
Surge Nozzle Fracture Mechanics Model (Nozzle Geometry)

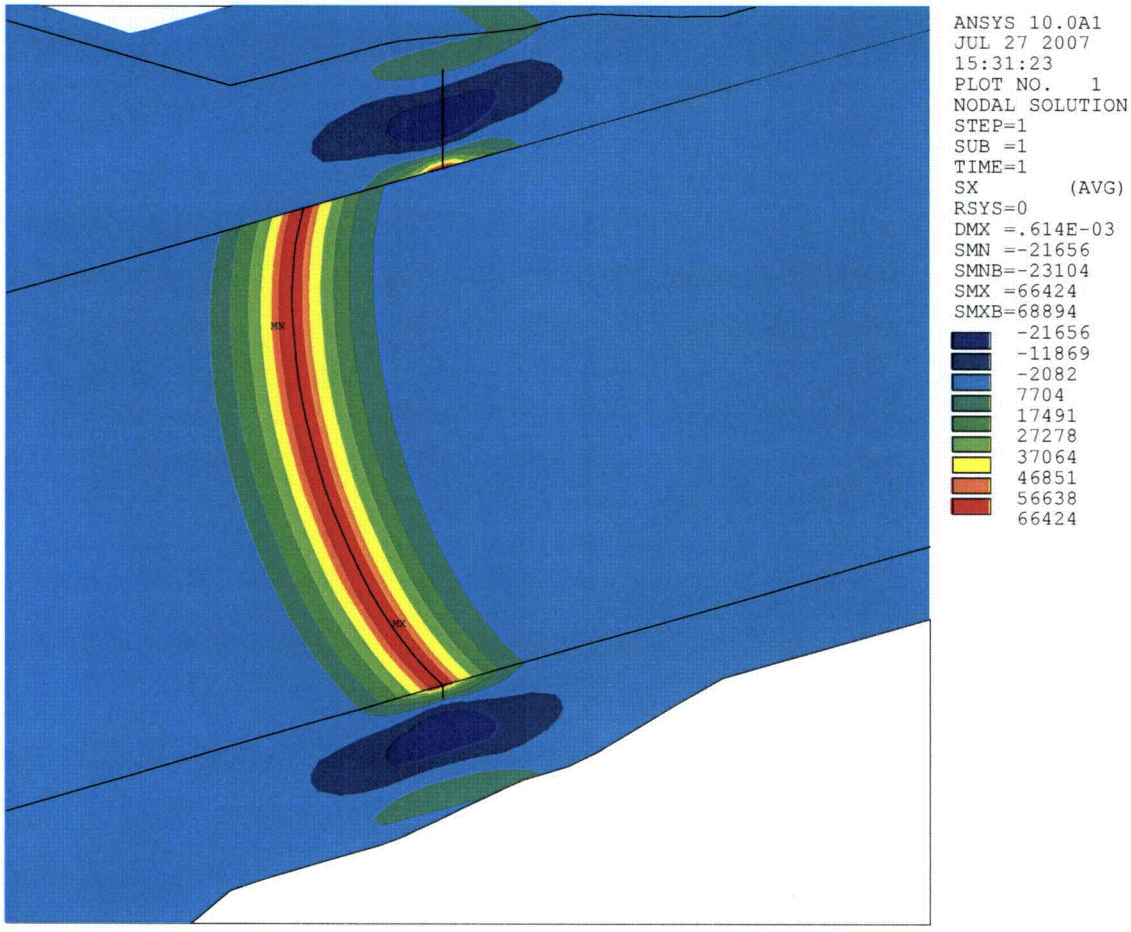

Figure 4-6
Safety Nozzle Imposed Axial Through Wall Stress Distribution

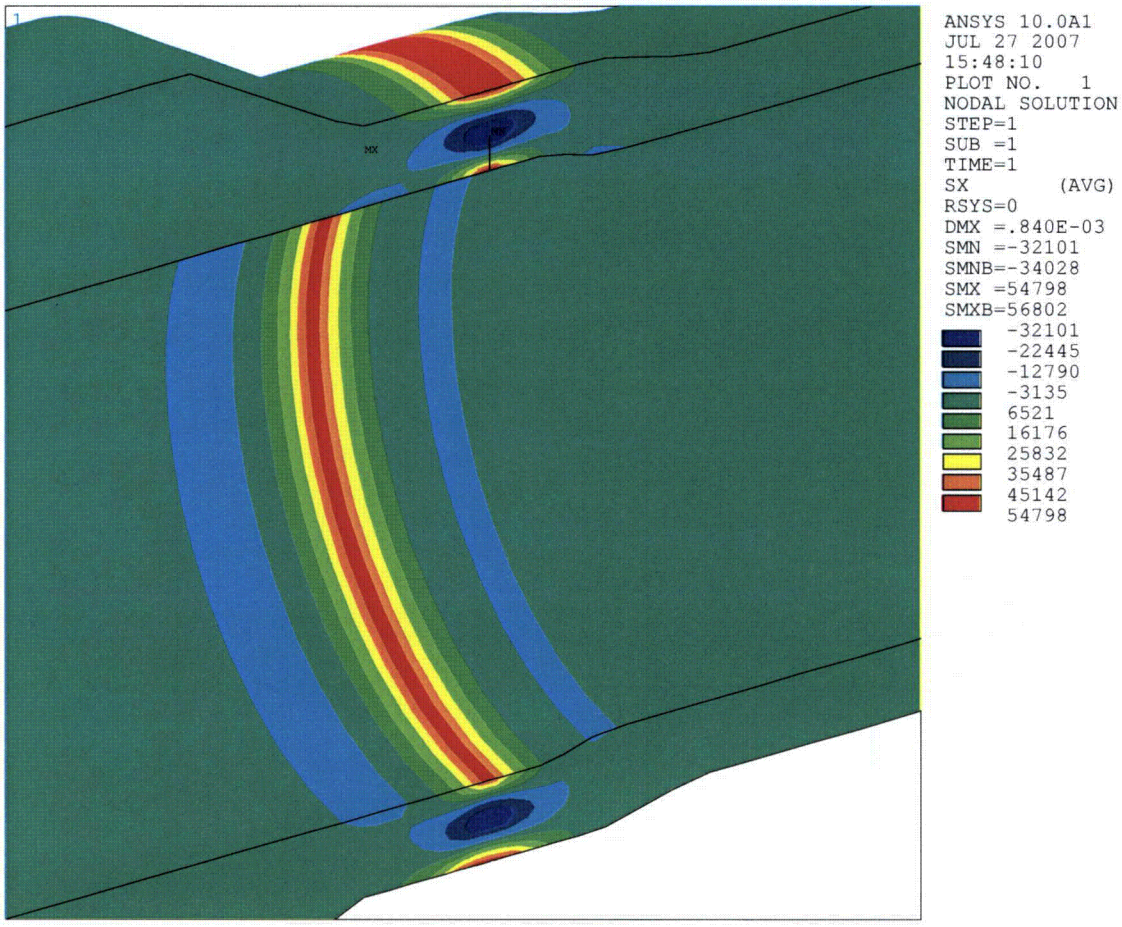

Figure 4-7
Surge Nozzle Imposed Axial Through Wall Stress Distribution

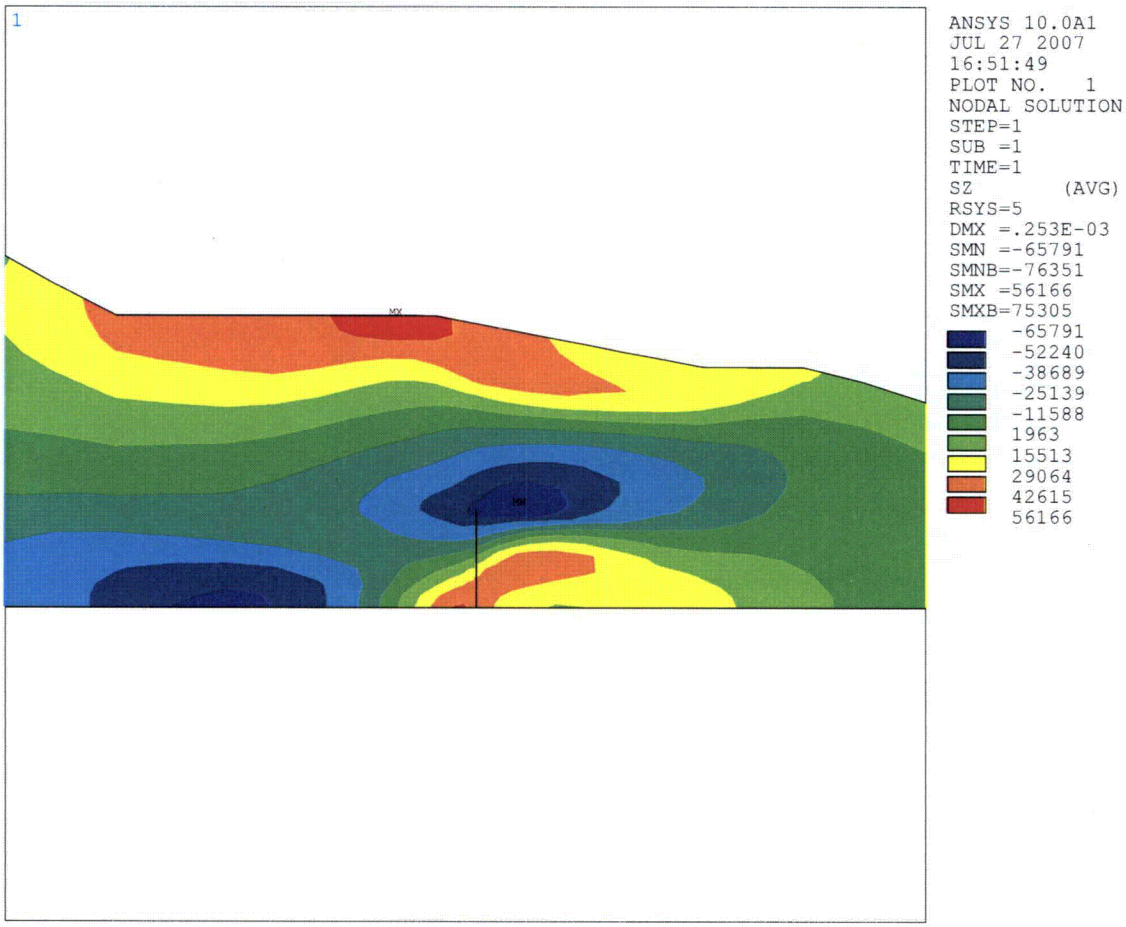

Figure 4-8
Safety/Relief Nozzle Interpolated Stress Distribution (Axial Stresses Shown)

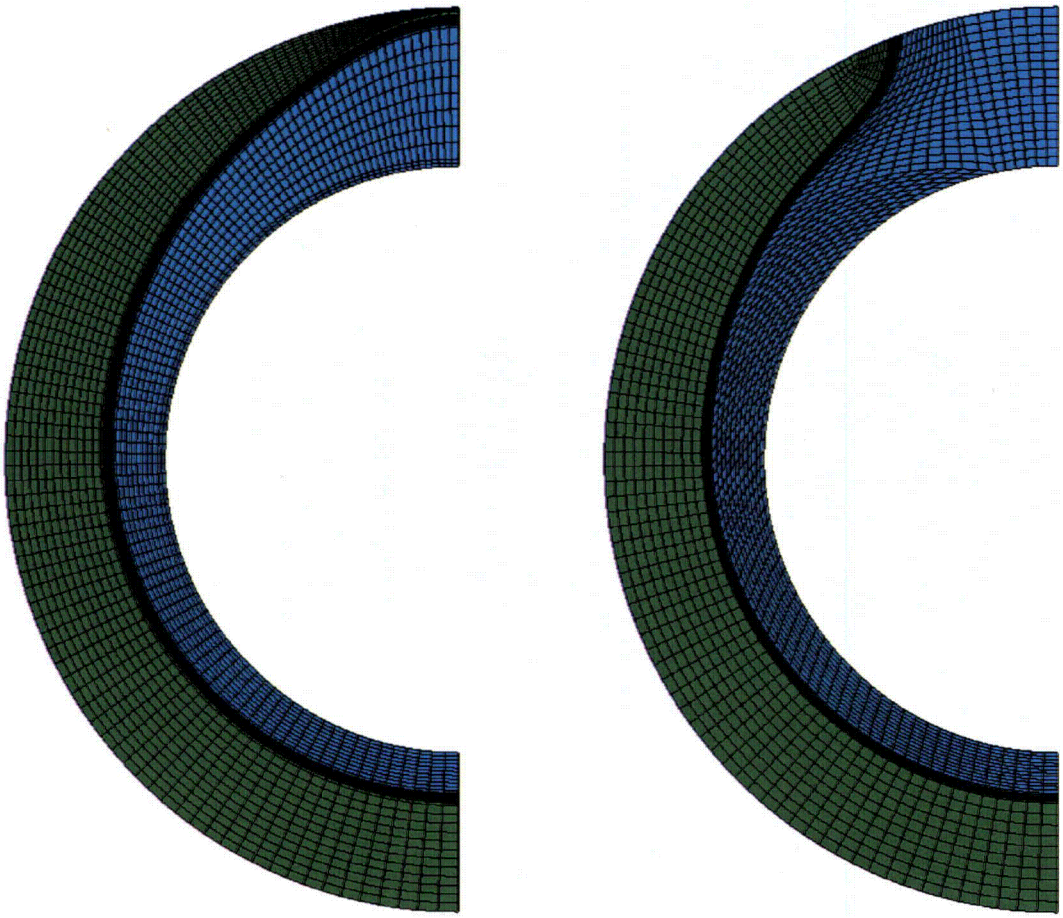

Figure 4-9
Example Mesh Transition from Surface Flaw to Complex Flaw

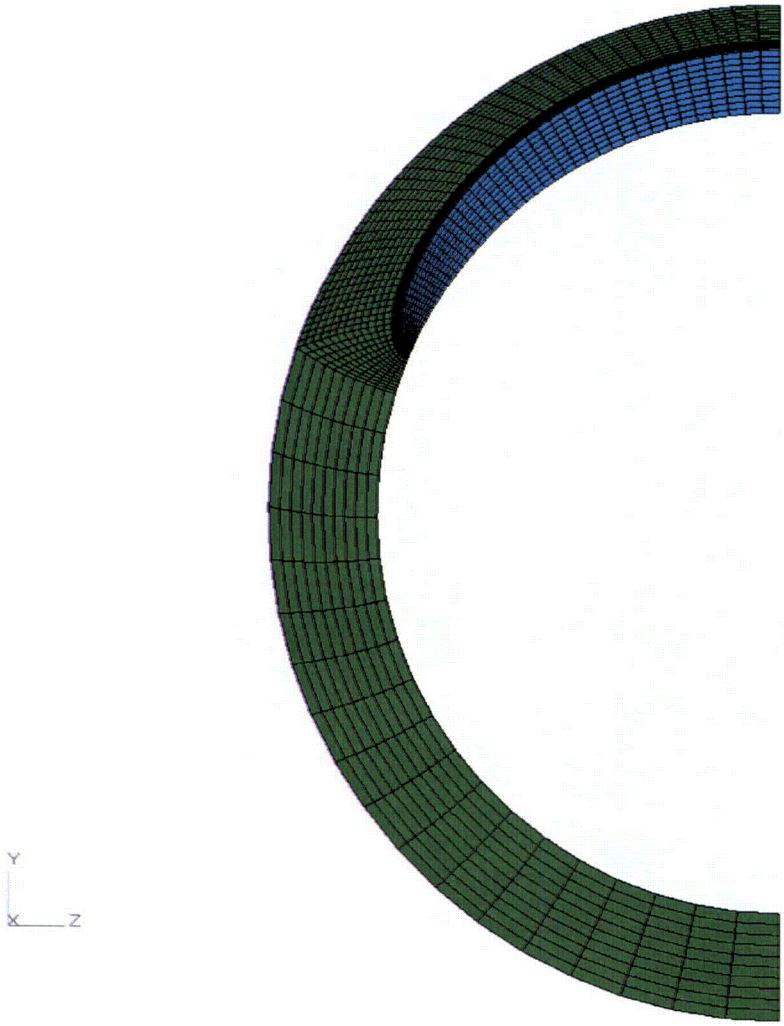

Figure 4-10
Part Circumference Custom Surface Crack Geometry Example

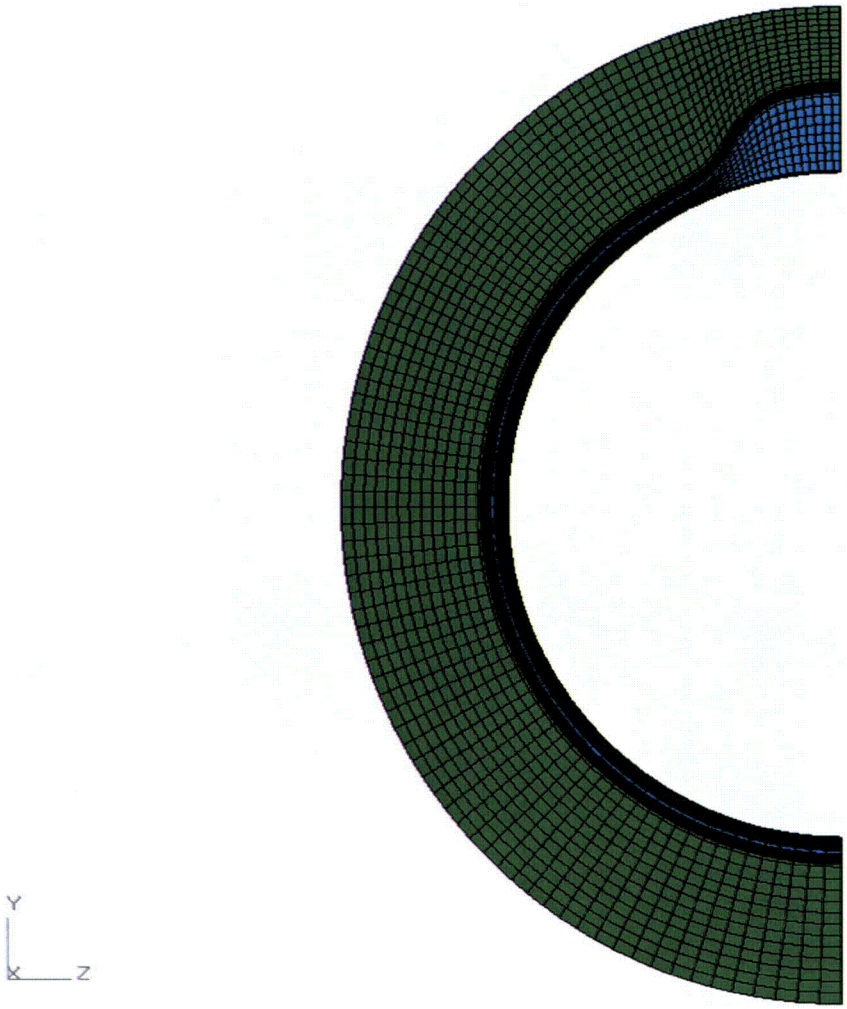

Figure 4-11
Full Circumference Custom Surface Crack Geometry Example

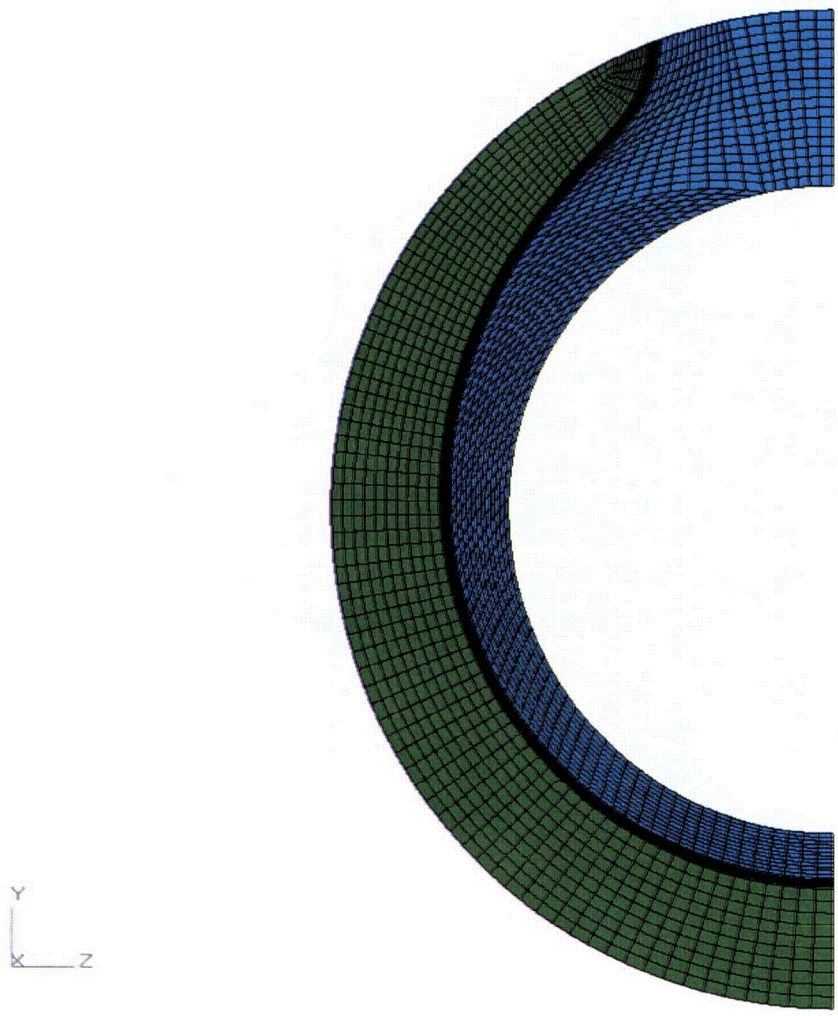

Figure 4-12
Complex Crack Geometry Example

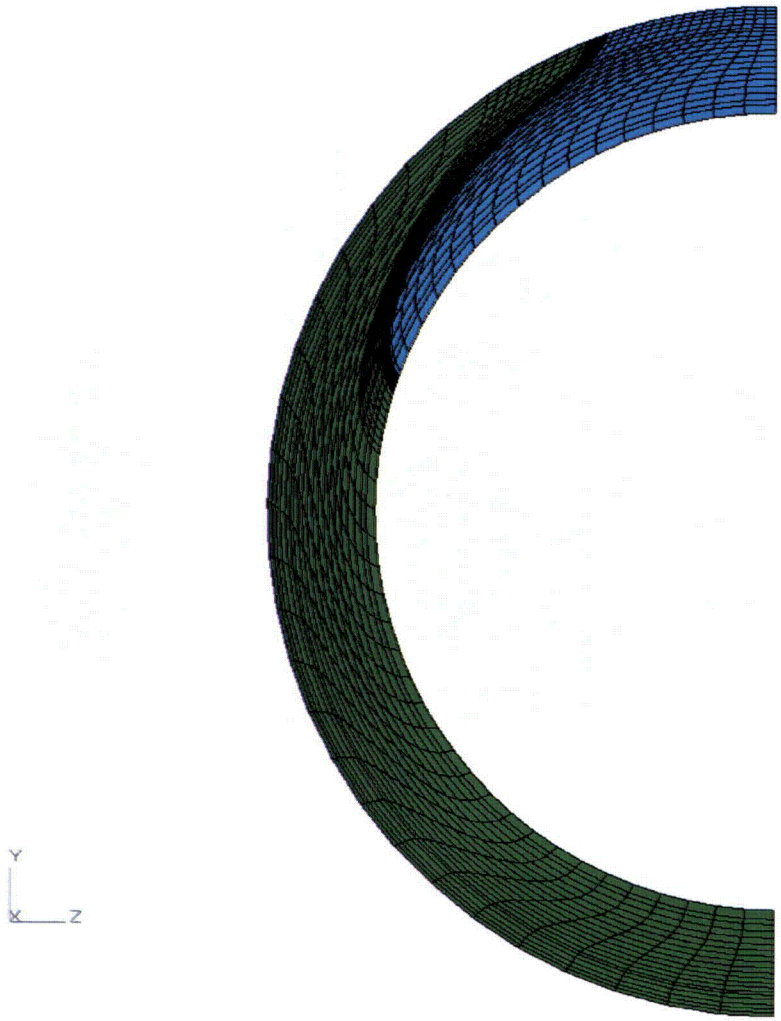

Figure 4-13
Custom Through-Wall Crack Geometry Example

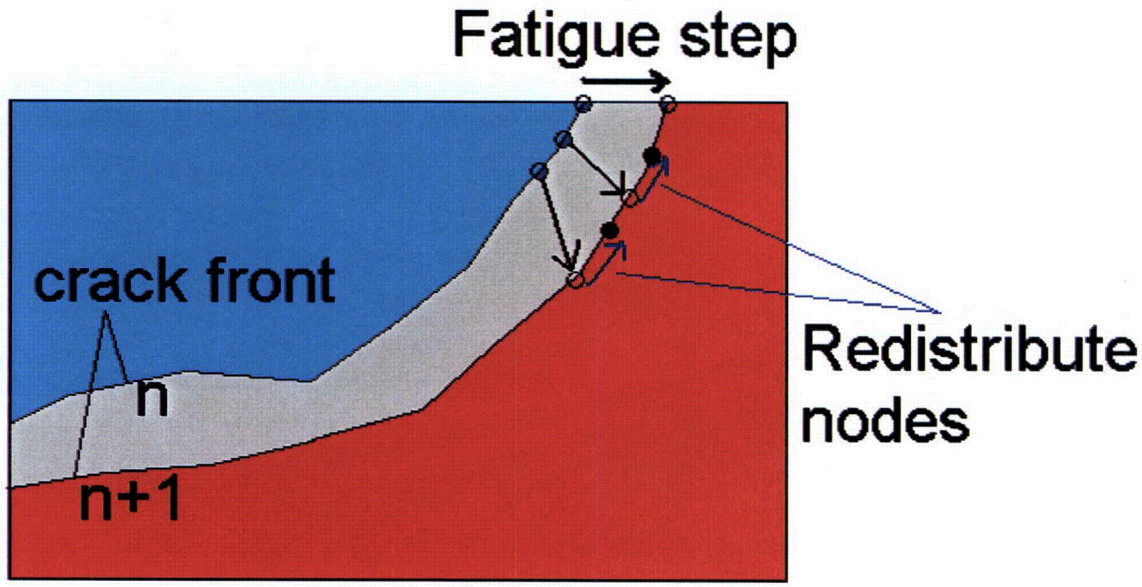

Figure 4-14
Illustration of Crack Front Redistribution During Crack Growth Calculations

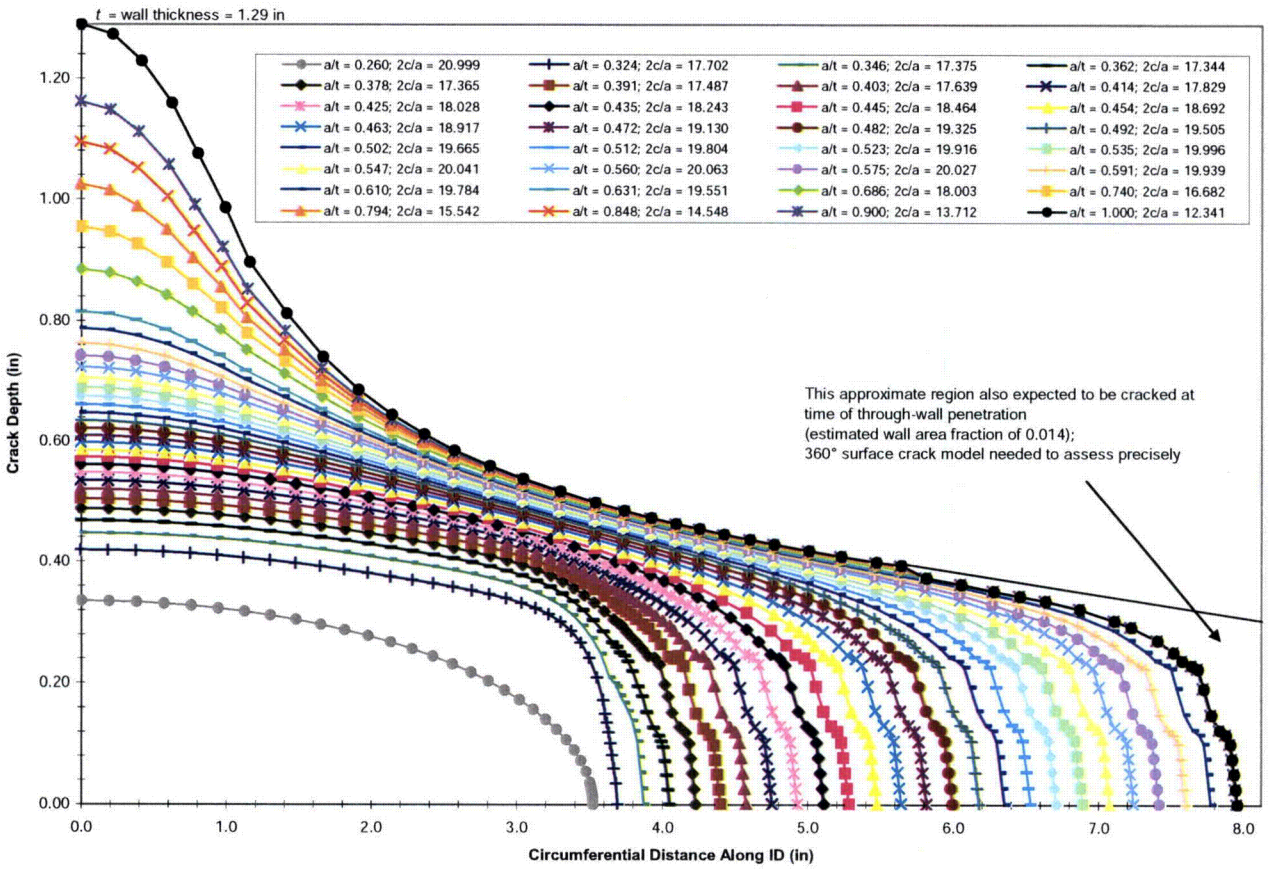

Figure 4-15
Phase I Initial Calculation Flaw Profile Growth (with Initial Semi-Elliptical Flaw Shape)

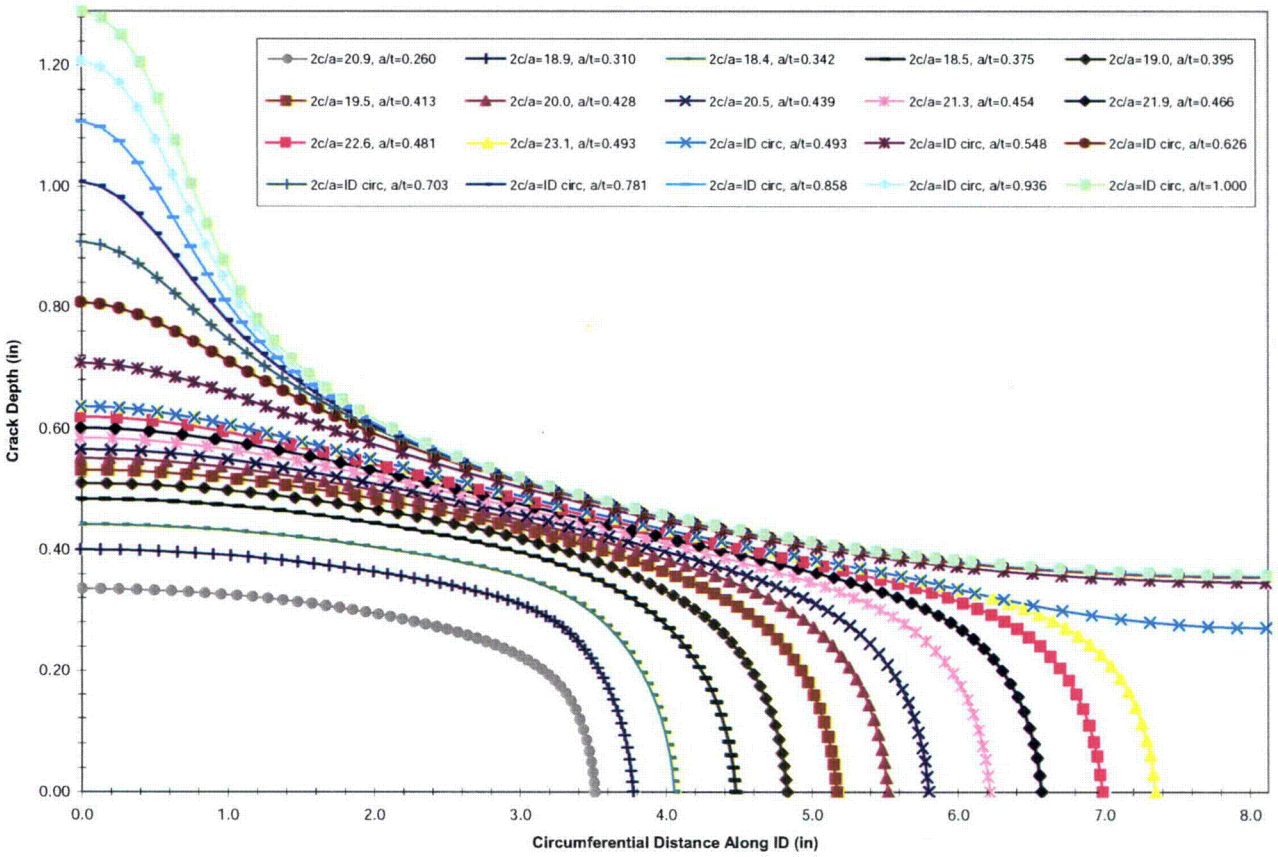

Figure 4-16
Phase I Second Calculation Flaw Profile Growth (with Initial "Natural" Flaw Shape)

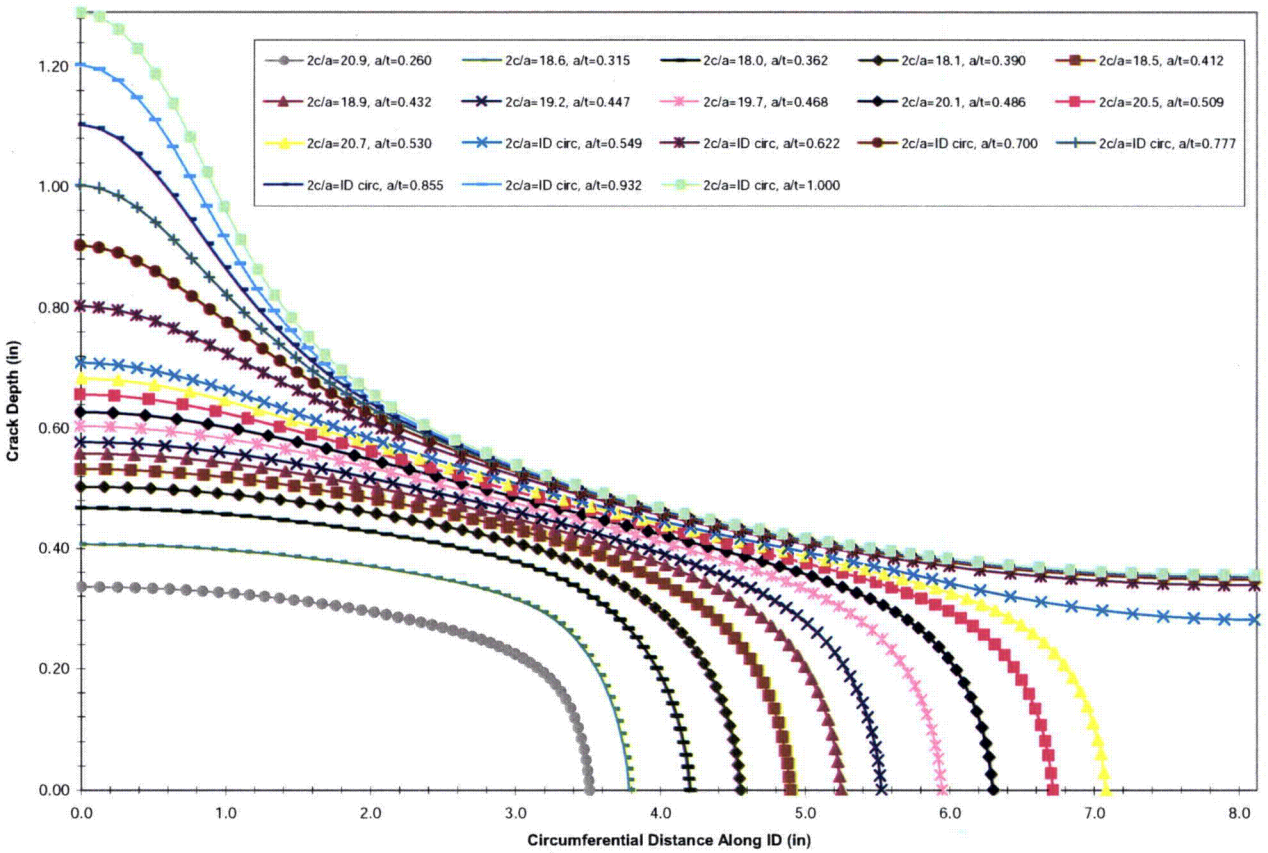

Figure 4-17
Phase I Third Calculation Flaw Profile Growth (with Initial "Natural" Flaw Shape)

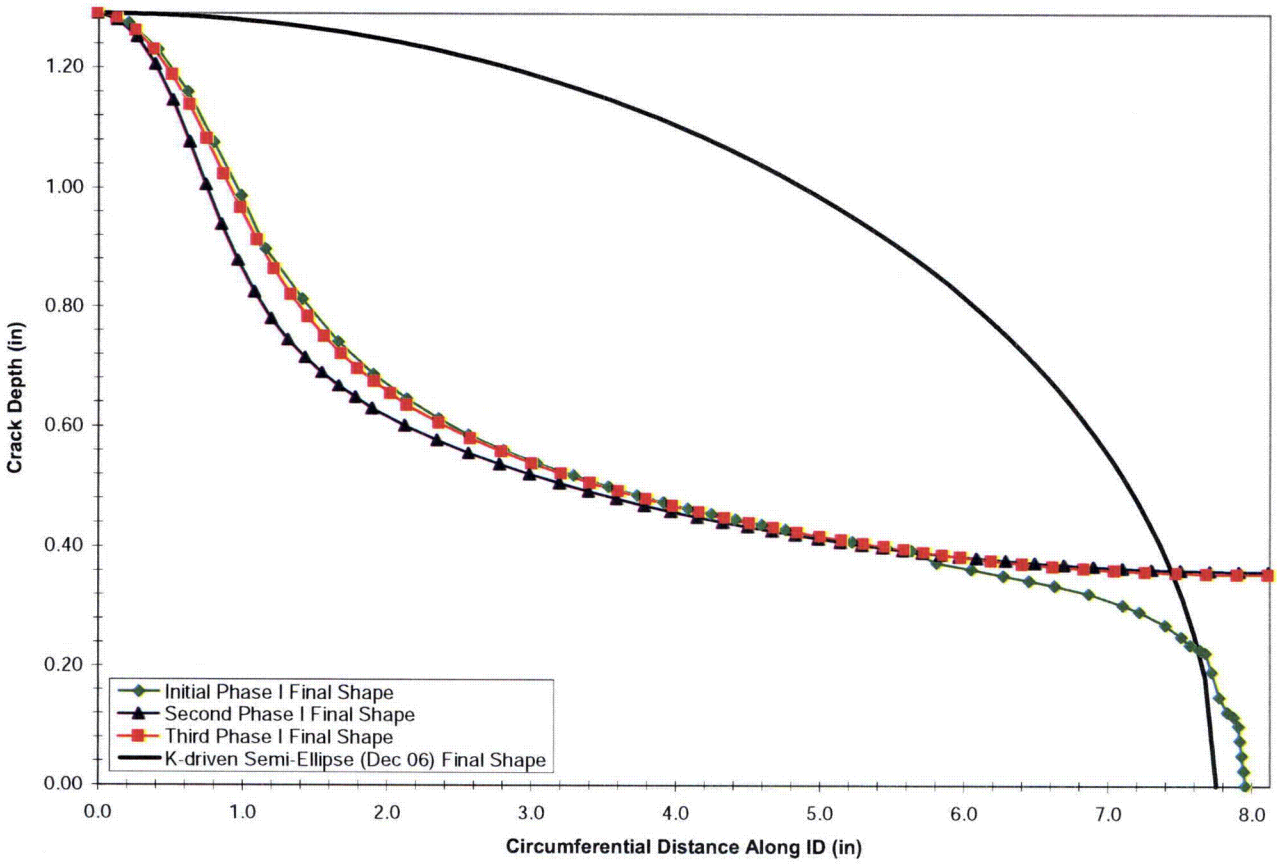

Figure 4-18
Comparison of Through-Wall Flaw Profiles for Phase I Calculation Analyses

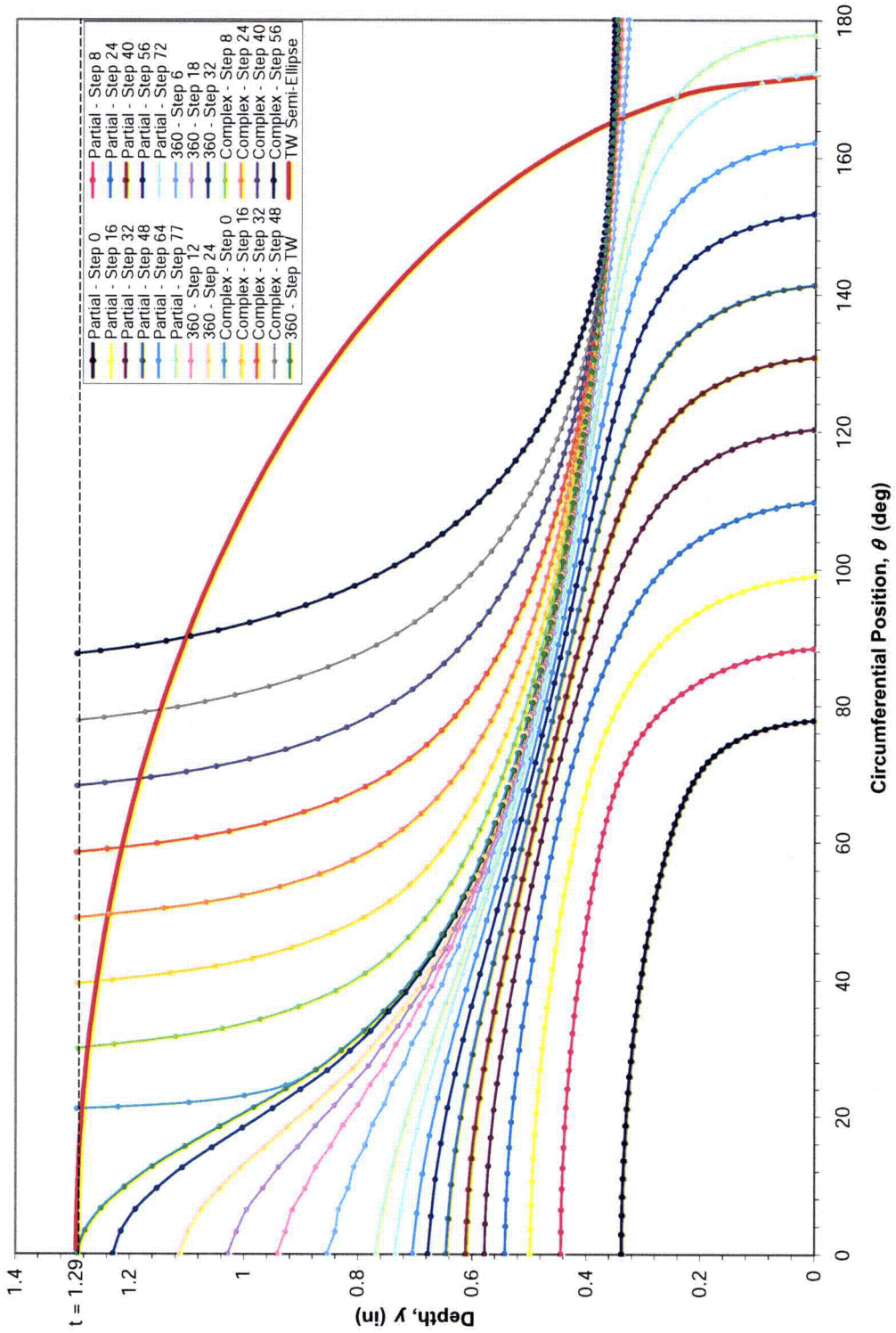

Figure 4-19
Phase I Crack Profile Evolution from Initial 21:1 Aspect Ratio 26% Through-Wall Flaw through Complex Flaws: Polar Coordinates

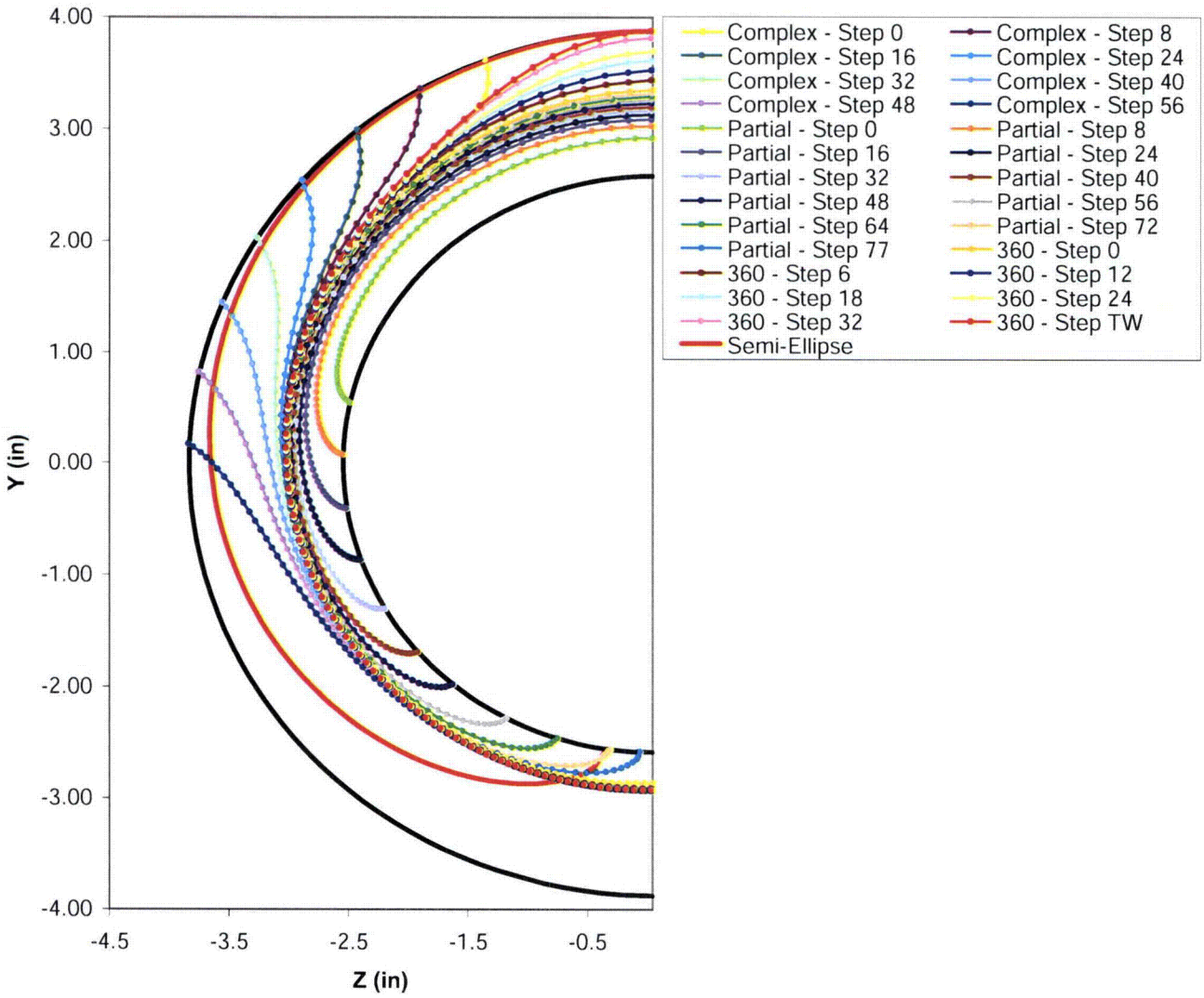

Figure 4-20
Phase I Crack Profile Evolution from Initial 21:1 Aspect Ratio 26% Through-Wall Flaw through Complex Flaws: Cartesian Coordinates

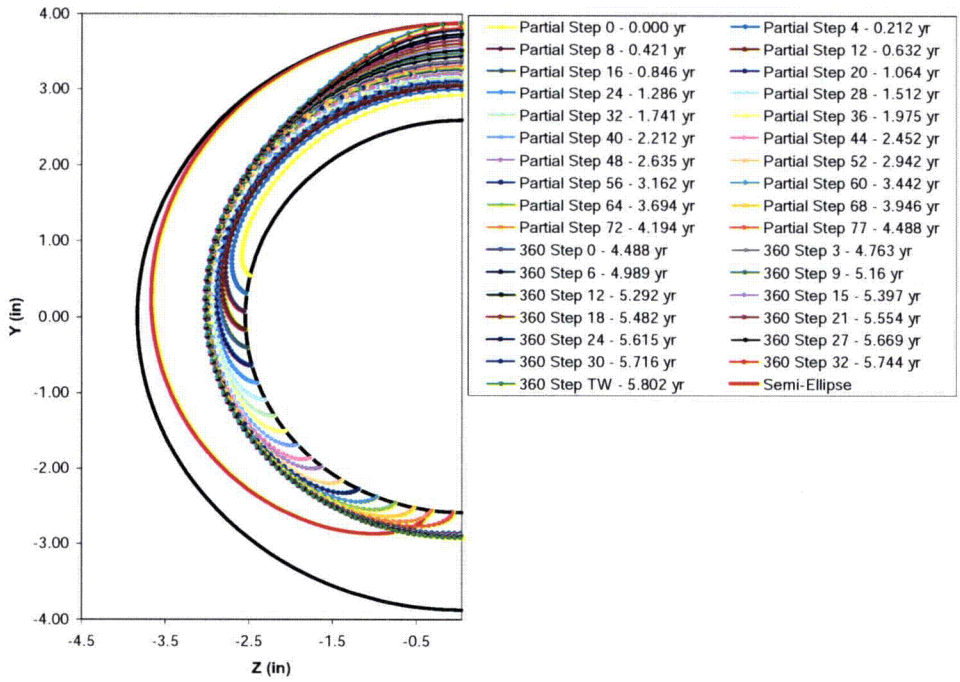

Figure 4-21
Phase I Surface Crack Profile Growth as a Function of Time since Initial 21:1 Aspect Ratio 26% Through-Wall Flaw

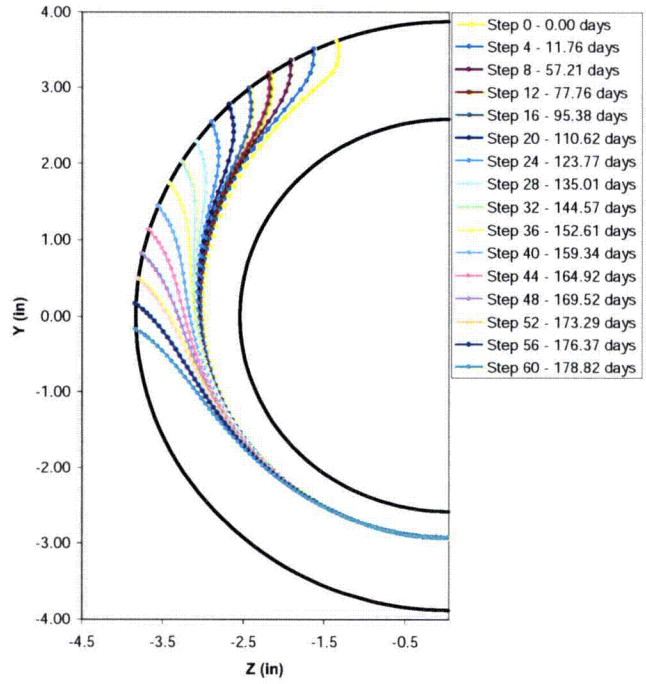

Figure 4-22
Phase I Complex Crack Profile Growth as a Function of Time since Through-Wall Penetration

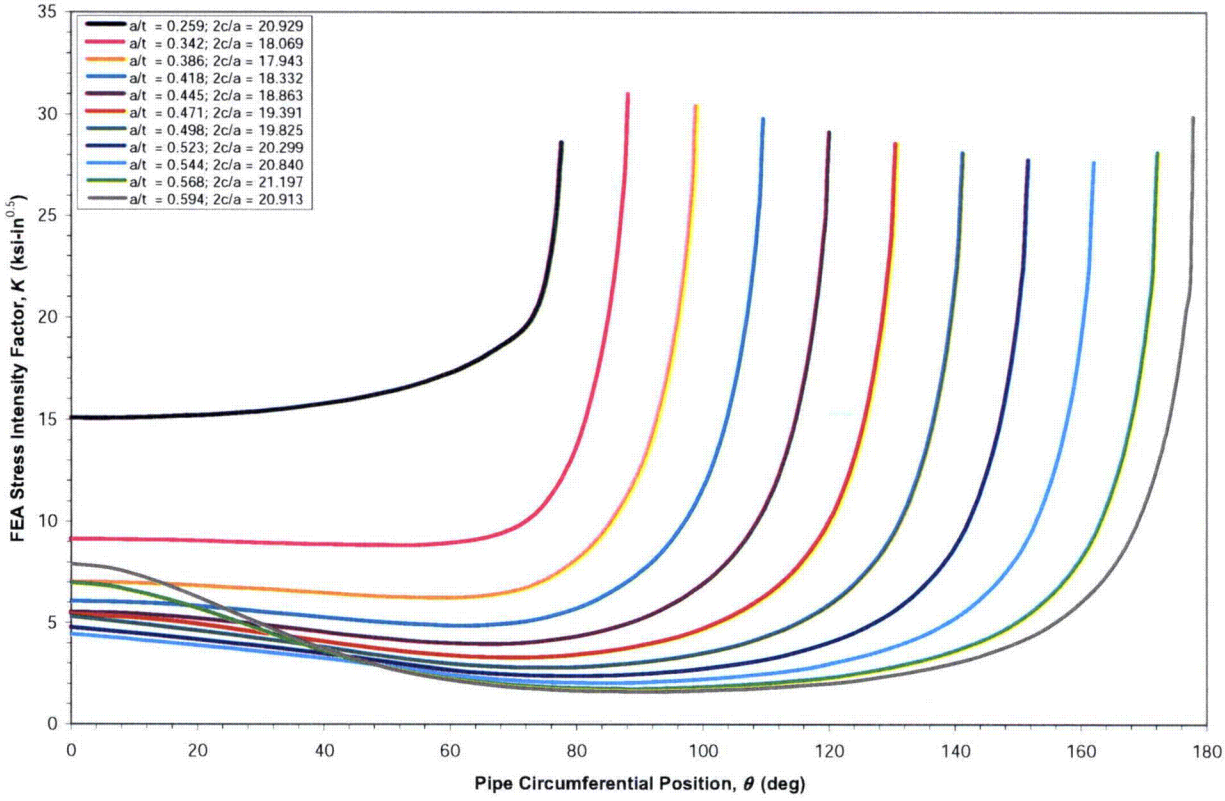

Figure 4-23
Phase I Crack-Tip Stress Intensity Factor Calculated along Crack Front for Partial-Arc Surface Growth

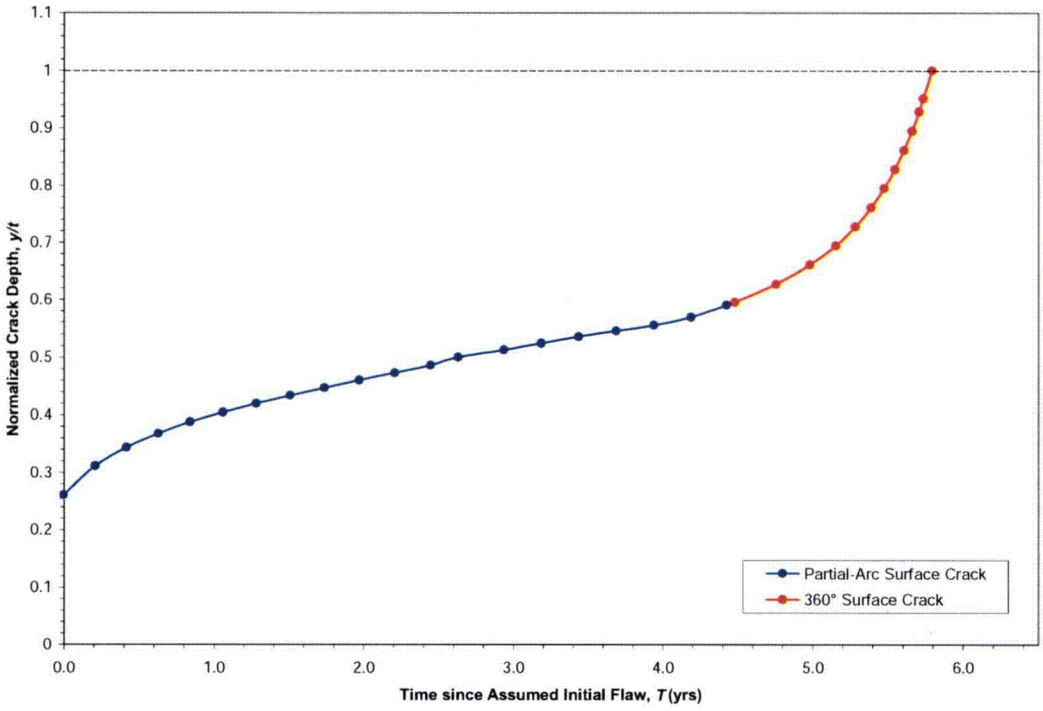

Figure 4-24
Phase I Surface Crack Depth as a Function of Time since Assumed Initial 26% Through-Wall Flaw

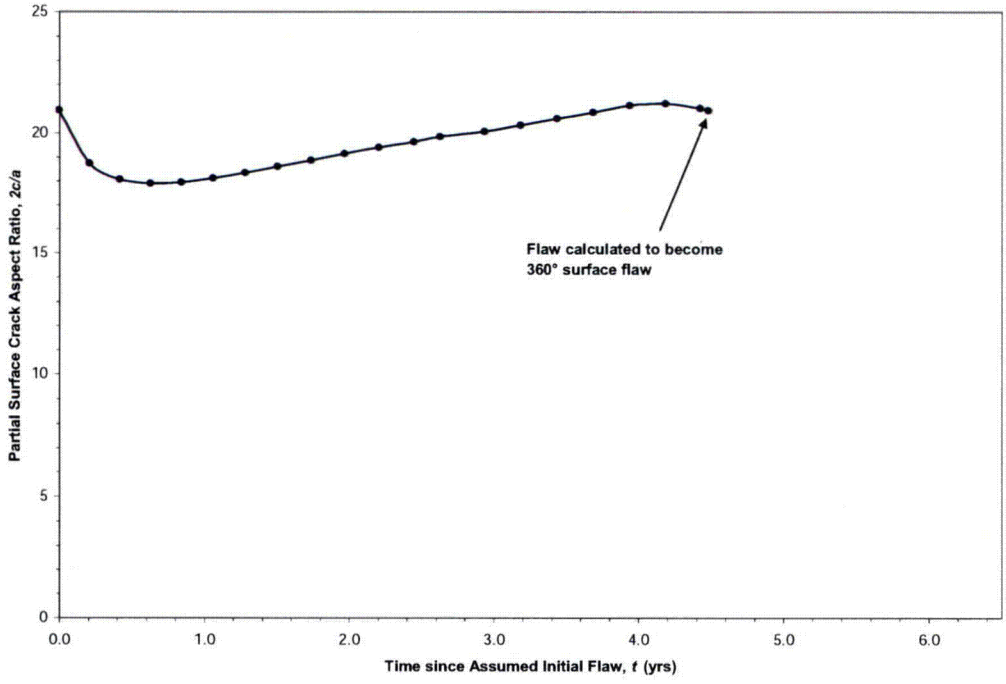

Figure 4-25
Phase I Surface Crack Aspect Ratio as a Function of Time since Assumed Initial 26% Through-Wall Flaw

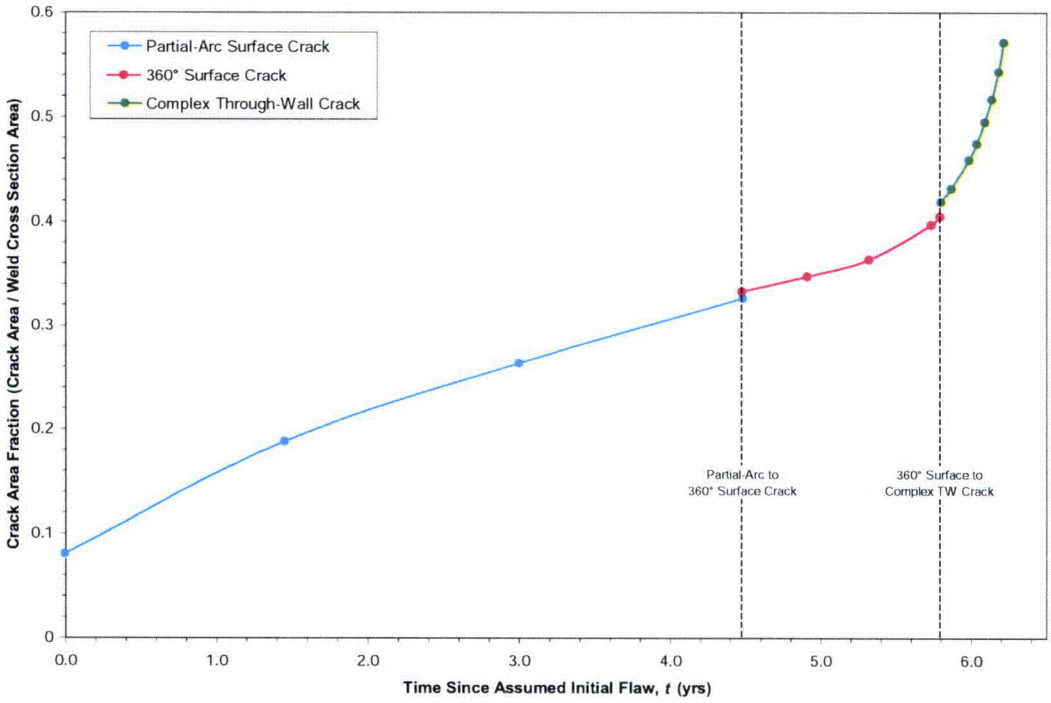

Figure 4-26
Phase I Surface and Complex Crack Area Fraction as a Function of Time since Assumed Initial 26% Through-Wall Flaw

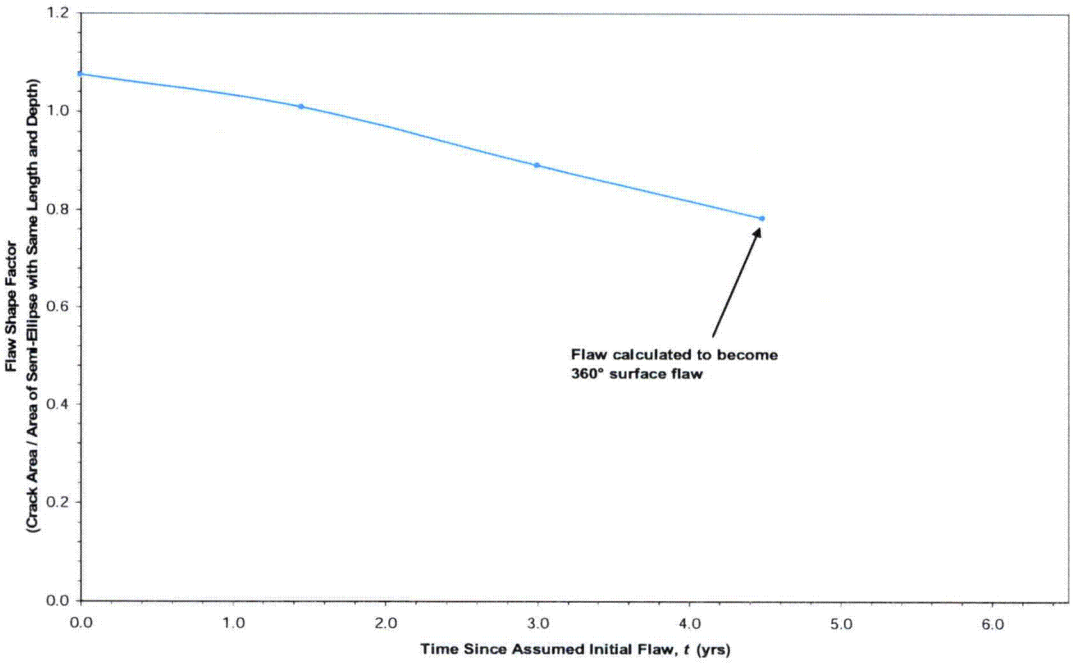

Figure 4-27
Phase I Surface Crack Shape Factor as a Function of Time since Assumed Initial 26% Through-Wall Flaw

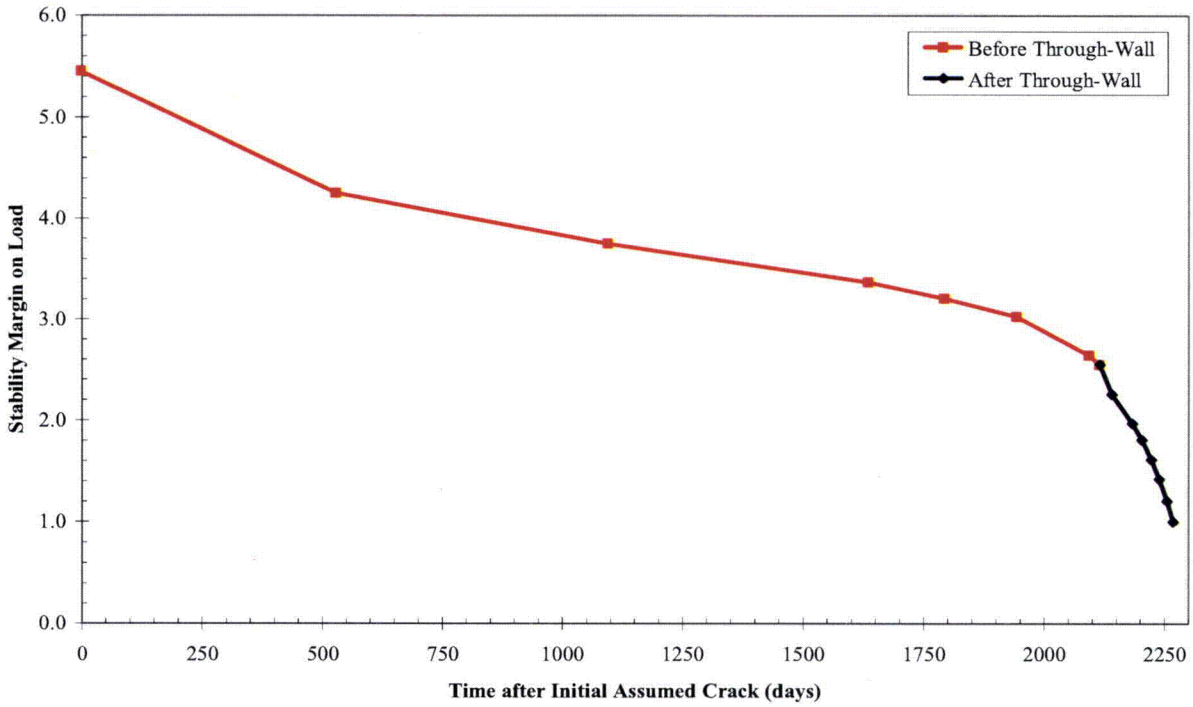

Figure 4-28
Phase I Load Margin Factor as a Function of Time since Initial 21:1 Aspect Ratio 26% Through-Wall Flaw

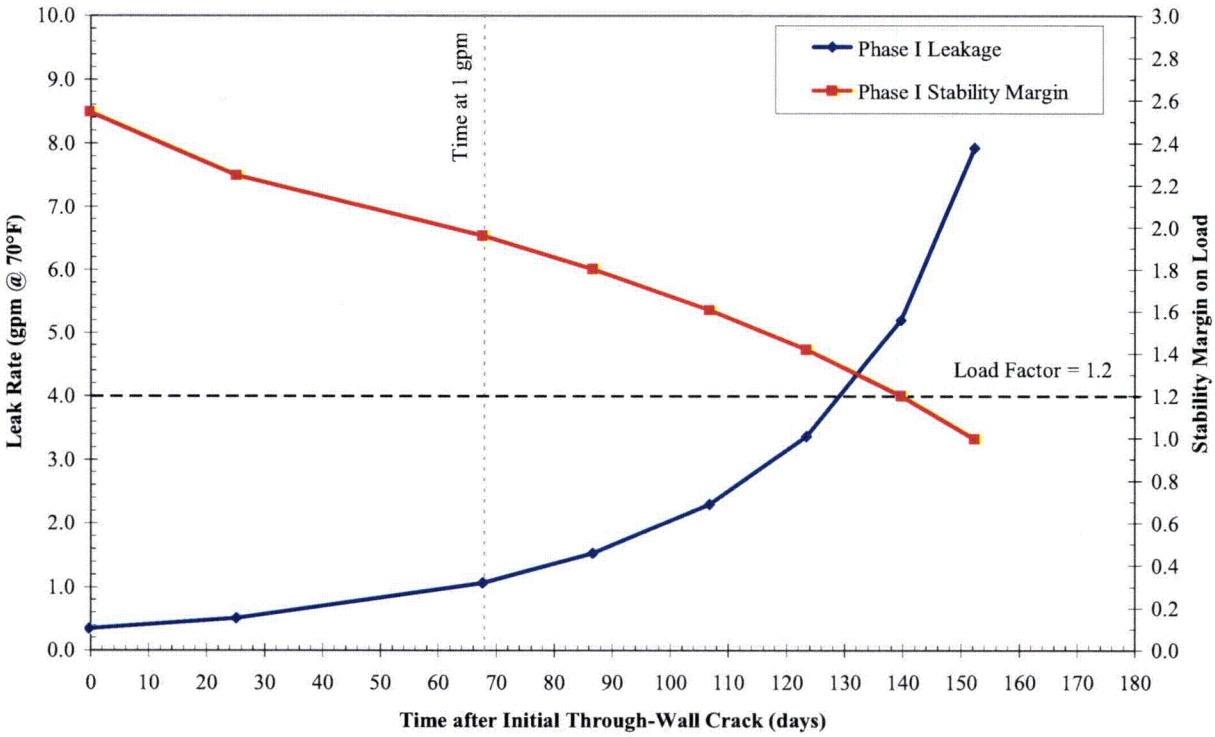

Figure 4-29
Leak Rate and Load Margin Factor as a Function of Time—Phase I Calculation

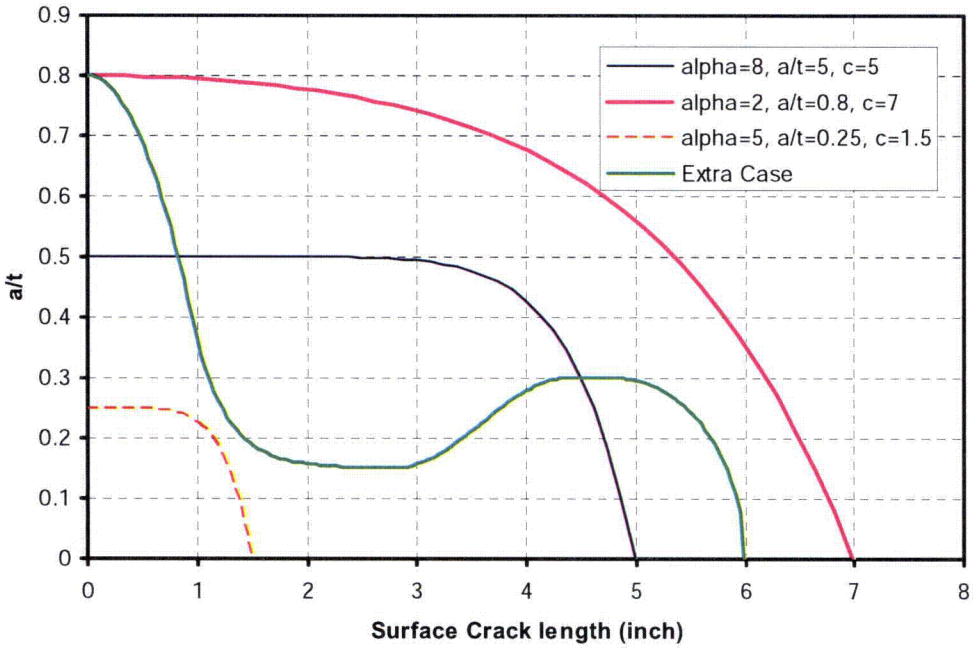

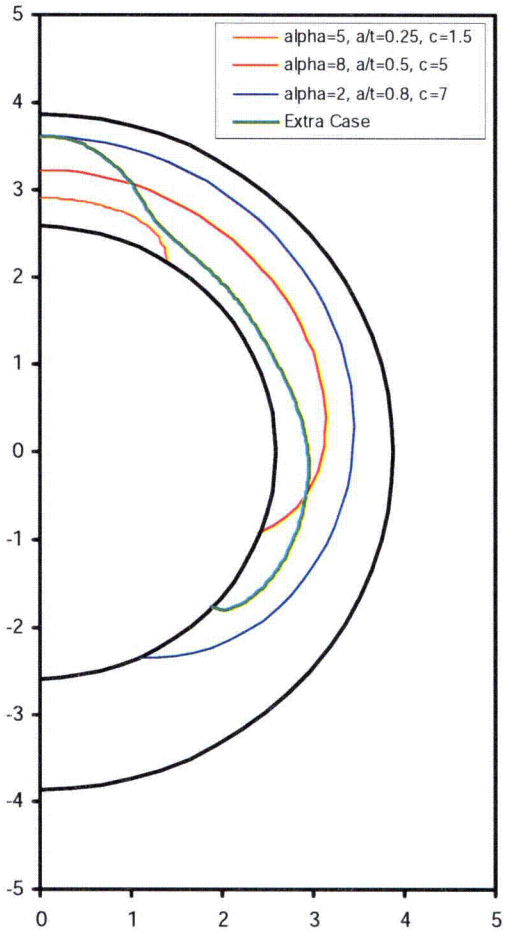

Figure 4-30
Flaw Profiles Used for Crack Tip SIF Calculation Verification

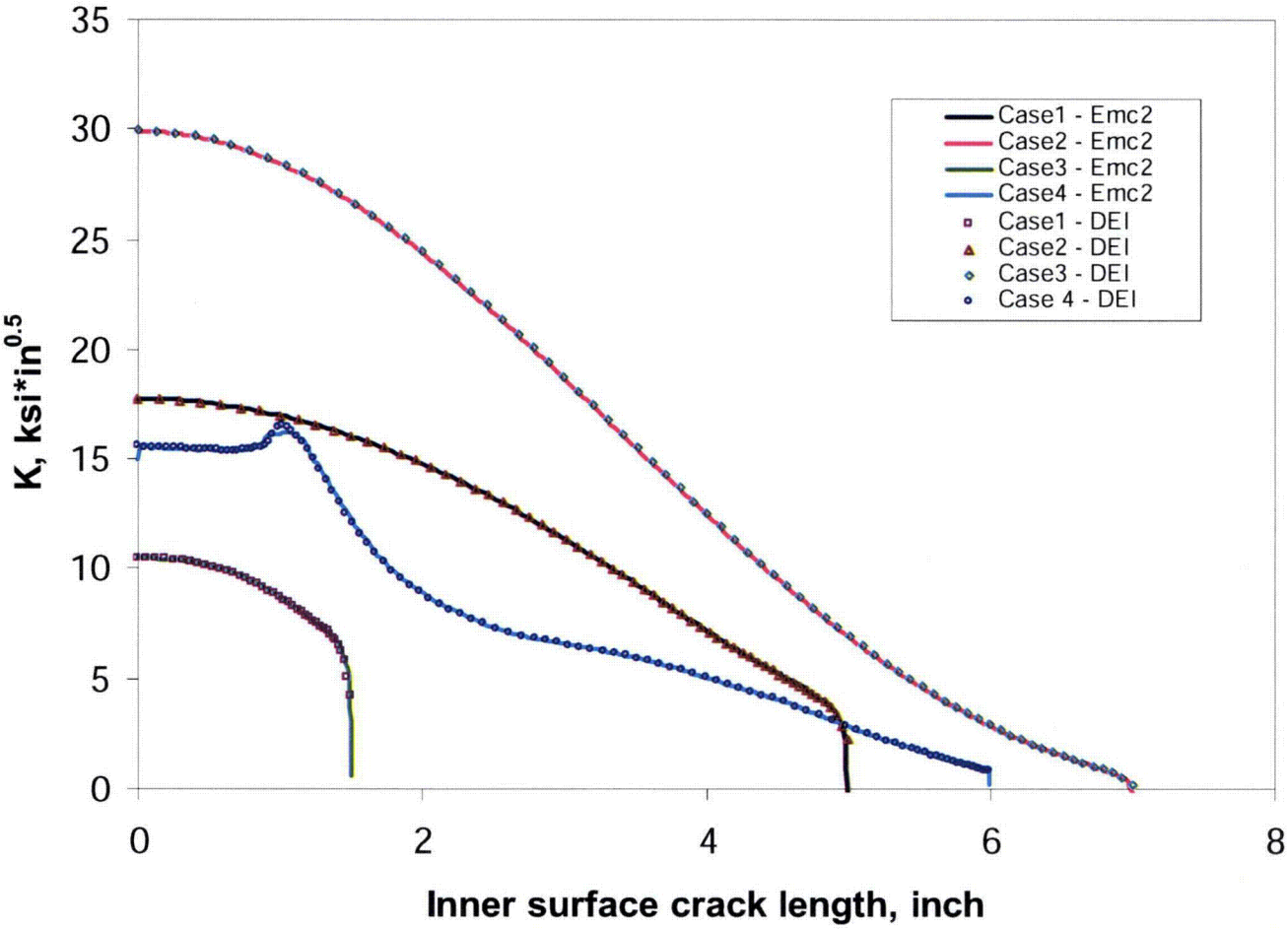

Figure 4-31
Crack Tip SIF Verification Results

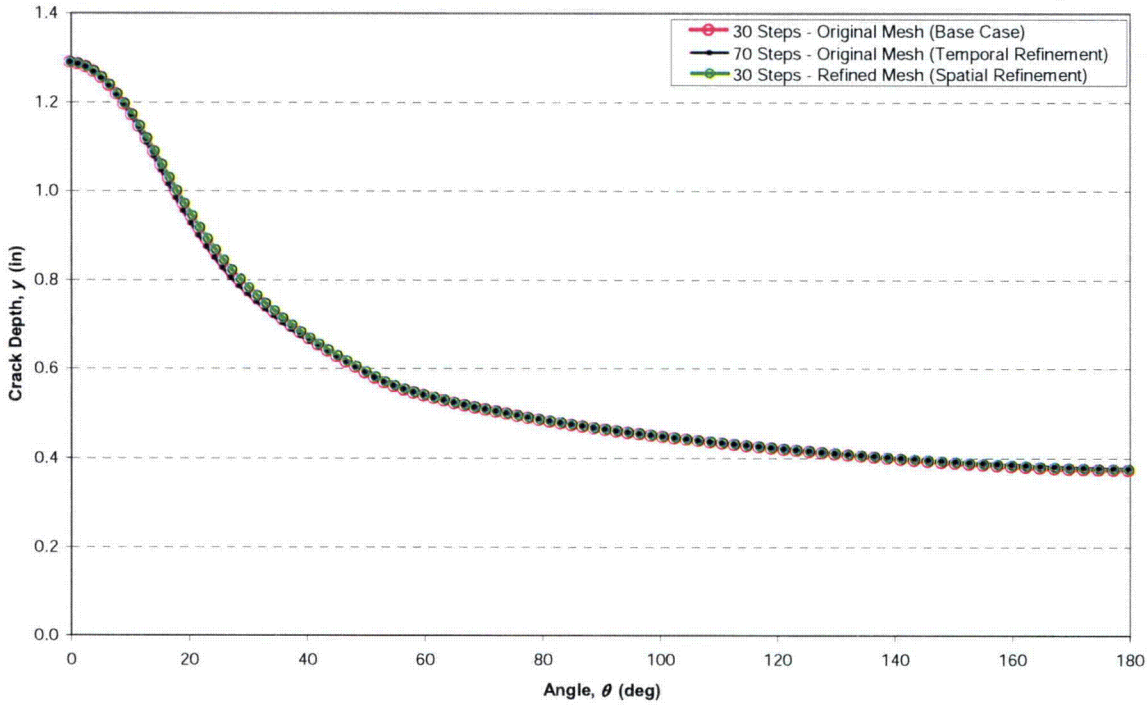

Figure 4-32
Temporal and Spatial Convergence Results for Case 1 360° Surface Crack Growth Progression

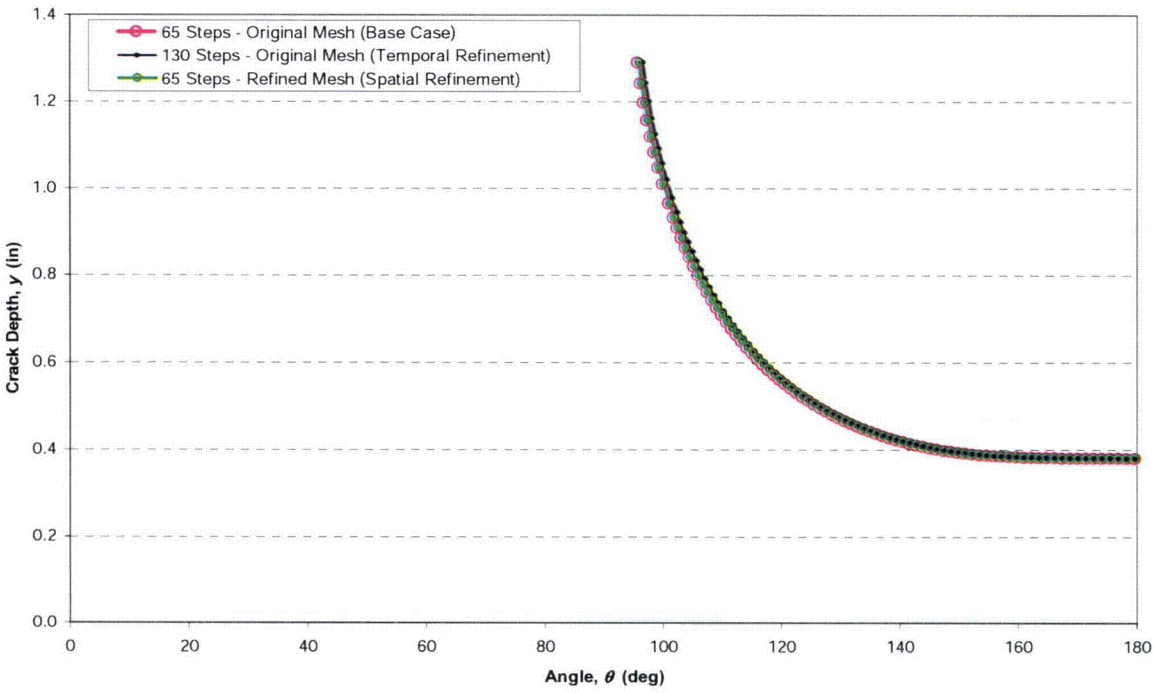

Figure 4-33
Temporal and Spatial Convergence Results for Case 1 Complex Crack Growth Progression

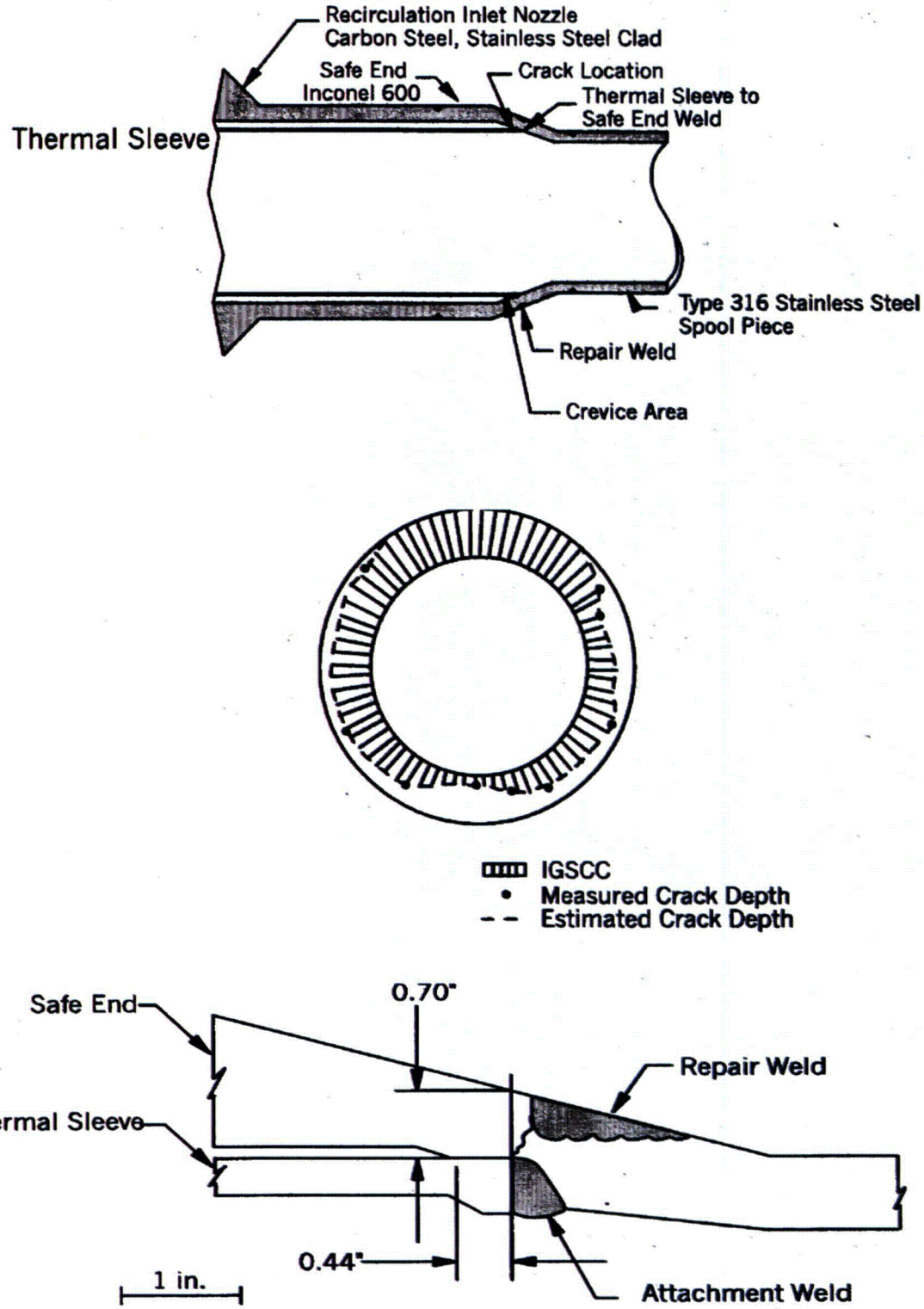

Figure 4-34
Cross Section Through 360° Part Depth Crack at Duane Arnold [22]

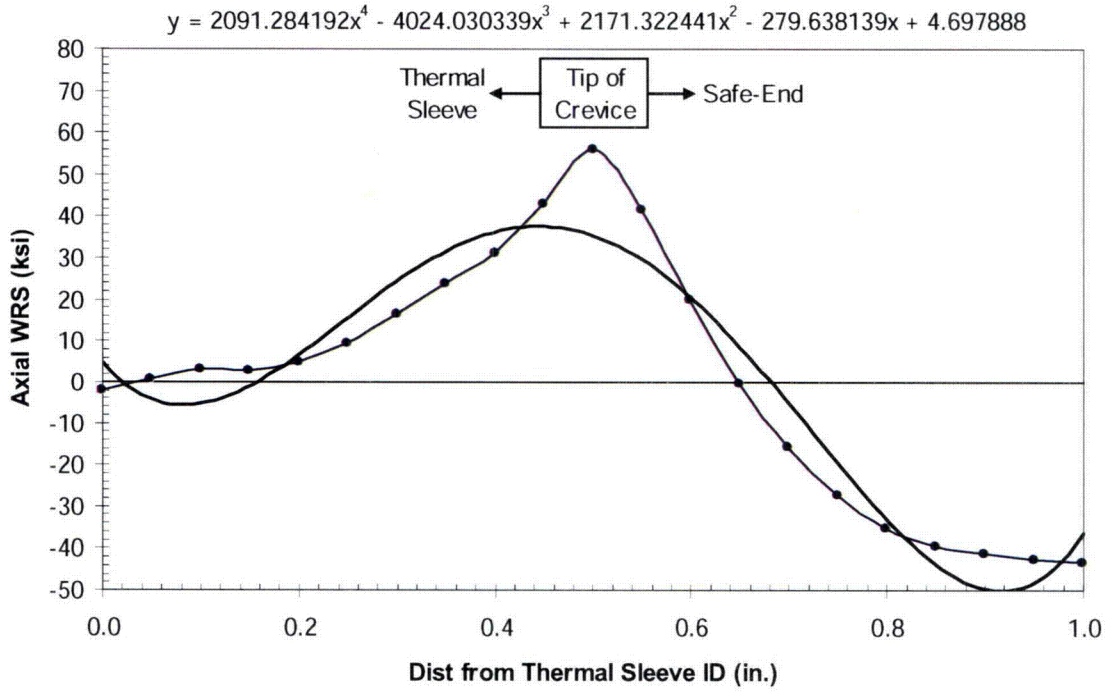

Figure 4-35
Polynomial Fit to Duane Arnold WRS Finite-Element Analysis Results

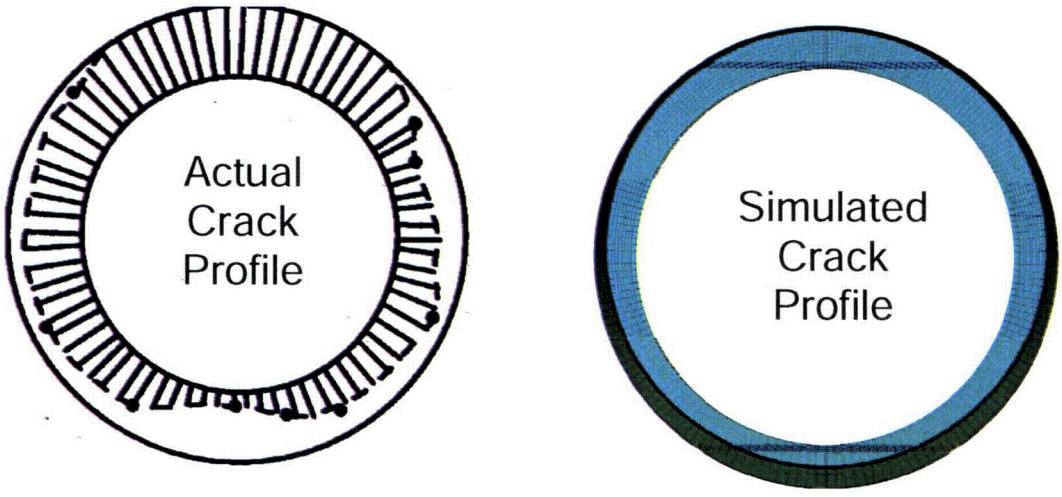

Figure 4-36
Comparison of Actual Duane Arnold Crack Profile with Simulated Crack Profile Assuming Initial 30% through-wall 360° Surface Flaw